PhD thesis in physics

On-chip manipulation and positioning of biomolecules with magnetic beads

written by
Michael Panhorst
born 3rd December 1974
in Bielefeld, Germany

Department of physics
Bielefeld University

July 2005

Declaration

I wrote this thesis by myself and used none but the indicated resources.

Bielefeld, 25th July 2005

(Michael Panhorst)

Reviewers:

Priv.-Doz. Dr. Andreas Hütten
Priv.-Doz. Dr. Robert Ros

Preface

The research in biotechnology boomed during the last decade, e.g. the gross investment per year for biotechnology in Germany increased from 24 million euro in 1994 to 150 million euro in 2004 [20]. This caused the evolvement of many new research fields in biotechnology during the last years.

One major research area in biotechnology is the selective detection of biomolecules. Such biosensors are available using many different detection methods. Most methods use markers which bind specifically to the target molecule and can be detected easily. The most common labels are fluorescent markers [107] which are widely commercially available. Other possible markers are nanoparticles [47], radioactive markers [112, 11], electrochemical markers [93] or magnetic markers [53], the latter of which are used in this thesis. Recent developments also use marker free detection methods, such as mass [130] and charge sensitive measurements [10] or measurements of the refractive index [99].

Another new trend is the full integration of all laboratory tasks into a lab-on-a-chip. Several research groups [43, 79, 129, 80] try to incorporate the laboratory preparation and detection methods into a portable hand-held device using microfluidic systems [3] and miniaturized detection methods. The use of magnetic markers and magnetoresistive sensors [114] has several advantages for a portable device. The magnetoresistive sensors directly provide an electric signal that can be evaluated with standard electronics, and they can be produced cheaply with standard microelectronic techniques. The pioneering work in this area was done by the Naval Research Laboratory [6], who introduced the BARC biosensor. While most groups use spinvalves for the detection [37, 53], some groups also use GMR/TMR sensors [114] or hall effect sensors [38].

Additionally to the sensor systems, magnetic markers allow the manipulation of the attached biomolecules with external magnetic fields. Although the manipulation with magnetic markers is a fairly new idea, several research groups are already working in this area. The magnetic fields can be generated through coils and poles around the sample [29, 50, 7] or by conducting lines

on the chip [51, 42, 136, 31, 87]. A few groups have already shown some interesting combinations of magnetic sensors and manipulation systems [52, 82].

This thesis especially focusses on the manipulation of magnetic markers with magnetic fields that are generated by conducting lines on a chip. Using currents through conducting lines to create the outer magnetic field allows an easy integration of the manipulation and detection methods into small hand-held devices. This thesis presents several working structures for the manipulation and positioning of magnetic markers. The maximum applied magnetic force is even high enough to use it for bond-force measurements, which are presented for the streptavidin-biotin and avidin-biotin bonds. But such a system is also exact enough to position single magnetic markers within an area of the size of the magnetic marker. Because this system is highly customizable, it is very interesting for many future applications.

Publications

M. Brzeska, M. Panhorst, P.B. Kamp, J. Schotter, G. Reiss, A. Pühler, A. Becker, and H. Brückl. Detection and manipulation of biomolecules by magnetic carriers. *Journal of Biotechnology*, 112:25–33, 2004.

H. Brückl, M. Panhorst, J. Schotter, P.B. Kamp, and A. Becker. Magnetic particles as markers and carriers of biomolecules. *IEE Proc.-Nanobiotechnol.*, 152(1):41–46, February 2005.

M. Panhorst, P.B. Kamp, G. Reiss, and H. Brückl. Sensitive bondforce measurements of ligand-receptor pairs with magnetic beads. *Biosensors and Bioelectronics*, 20(8):1685–1689, 2005.

G. Reiss, H. Brückl, A. Hütten, J. Schotter, M. Brzeska, M. Panhorst, D. Sudfeld, A. Becker, P.B. Kamp, A. Pühler, K. Wojczykowski, and P. Jutzi. Magnetoresistive sensors and magnetic nanoparticles for biotechnology. *submitted to Journal of Materials Research*, 2005.

Conferences

Poster at the Nanobionics 2 conference (293$^{\text{th}}$ Wilhelm and Else Heraeus Seminar) in Marburg (2002): "Manipulation of biomolecules with magnetic carriers and their detection"

Poster at the DPG Frühjahrstagung (AK Festkörperphysik) in Dresden (2003): "Manipulation of biomolecules with magnetic markers"

Poster at the SFB613-Workshop in Bielefeld (2003): "Manipulation and detection of biomolecules by magnetic carriers"

Poster at the eigth world congress on biosensors in Granada (2004): "On-chip manipulation of biomolecules using magnetic beads"

Talk at the DPG Frühjahrstagung in Berlin (2005): "Transport und Positionierung von Biomolekülen mit magnetischen Markern"

Contents

Chapter 1

Basics

The transportation, manipulation, positioning and detection of single biomolecules with magnetic particles requires knowledge of different scientific areas. Biochemical skills are needed for the functionalisation of the sample surface and the investigation of bonds between biomolecules. Physical knowledge is required for the preparation of the chips, the calculation of magnetic field configurations or the detection of magnetic markers with TMR sensors. This chapter provides the theoretical background for all areas that are used in this thesis. It starts with basics about the used biomolecules and their bonds, goes on about magnetic field configurations and finishes with some TMR theory.

1.1 Biomolecules

The interaction between biomolecules is a key aspect to examine and characterise biological systems. Common interactions are e.g. antibody-antigen interactions [27, 66, 110] or protein-protein interactions. A very versatile biosensor that can detect different kinds of biomolecules (DNA, Proteins, ...) and also examine different interactions between them would be most desirable, therefore. This is quite difficult, because the size of the biomolecules, the bond-type and with it the bond-force differ a lot, from a small antibody to a big protein-complex. For all marker based biosensors, this means that many versatile markers have to be available. The magnetic markers that are used in this thesis are available in many different sizes and configurations (see section 1.2).

A new technique to measure the bond-force between two biomolecules with magnetic markers is presented in chapter 4. To show the general applicability of this method, the well known streptavidin-biotin and the avidin-

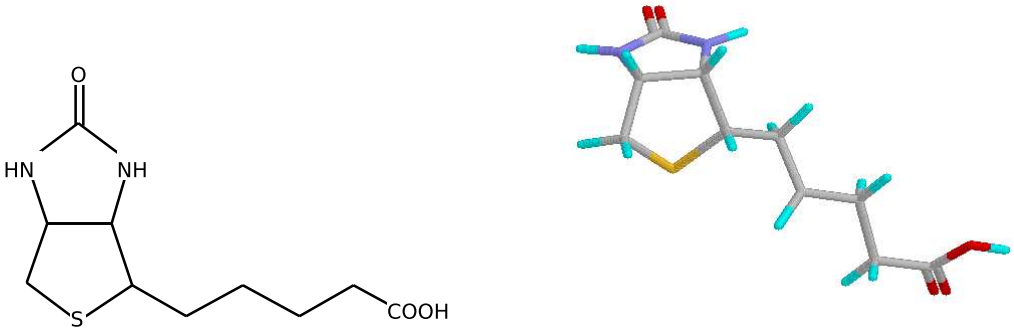

(a) Chemical structure of biotin, based on [26]

(b) Three-dimensional structure of biotin [33]

Figure 1.1: Biotin

biotin bonds were examined. In order to understand the processes during the bond-force measurements, the following sections describe the major properties of all three participating biomolecules and the bond properties.

1.1.1 Biotin

The discovery, isolation and synthesis of biotin started in 1927 with an experiment where rats developed an unusual dermatitis after they were fed only with the protein of hen egg white [14]. The dermatitis could be cured by a substance that was called vitamin H and that is present in many foodstuff. But it took many years, until György *et al.* [60] identified in 1940 that biotin and vitamin H are identical.

Biotin ($C_{10}H_{16}N_2O_3S$) is a coenzyme that plays a vital role in nearly all organisms (from bacteria to animals) [35]. Like many coenzyms, biotin cannot be synthesised by animals and must be obtained from plants. It is not indispensable for life, but humans and animals with a biotin deficiency can get dermatitis[1] or alopecia[2]. Biotin is a component of many enzymes in the human body and plays a vital role in the degradation of specific proteins (e.g. serum albumin) [13].

Figure 1.1 presents the chemical structure (a) and a three-dimensional image of biotin (b). Biotin consists of an imidazole ring with an attached

[1] skin rash or eczema
[2] loss of hair

valerat side chain. The carboxyl group at the end of the chain can bind covalently to the amino-groups of enzymes [127]. The molecular weight of biotin is only 144 Da [3] [9] and it is only about 7 Å long (see [32] for more information about the structure of biotin and its vitamers).

1.1.2 Avidin

The discovery of avidin is closely related to the discovery of biotin, because the egg white that was fed to the rats only contains biotin that is bound to avidin and the metabolism of rats is not able to separate those. Avidin accounts for maximal 0.05 % of the protein that is found in eggs and oviducts of many species of birds [57].

Avidin is very soluble in water and salt solutions between pH 5-7 and has its isoelectric point at pH 10 [57]. The basic tetrameric glycoprotein consists of 256 amino acids with an overall dimension of $72 \times 80 \times 44$ Å^3 [106] and has a molecular weight of 57 kDa [98]. A comprehensive overview about avidin was already published in 1963 by Green and Melamed [56]. Figure 1.2 shows the three-dimensional structure of avidin, which was acquired by x-ray diffraction methods.

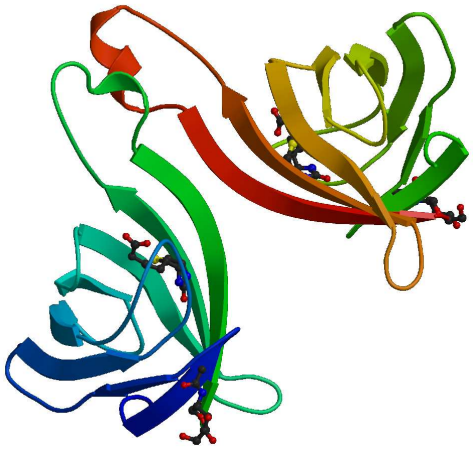

Figure 1.2: Three-dimensional structure of avidin, acquired with x-ray diffraction methods [106]

Although the high affinity to biotin was known from early on, the interest in avidin was low until the discovery of the coenzyme function of covalently bound biotin. The very high affinity between biotin and avidin together with the possibility to bind coenzymes covalently to the biotin made clear that avidin could be very useful to characterise new classes of enzymes [57]. Furthermore, the bond between biotin and avidin can resist dissociation in the presence of detergents, high and low pH values, protein denaturants and high temperatures. Today, many different macromolecules (e.g. proteins, polysaccharides or nucleic acids) can easily be linked to biotin without serious affect on their biochemical or physical properties. The generic nature of the biotinylation process and the high strength of the avidin-biotin bond makes this technology easily accessible and, therefore, interesting for

[3] Dalton - unit of the molecular weight: $1\,\text{Da} = 1,66054 \cdot 10^{-24}\,\text{g}$ [69]

scientific and industrial research [100].

Section 1.1.4 presents a more in-depth study of ligand-receptor bonds like the avidin-biotin bond.

1.1.3 Streptavidin

The discovery of streptavidin was totally unexpected and happened during a screening of *Streptomyces* for antibiotics. The antibacterial effects could be reversed by high concentrations of biotin in the medium. A closer look revealed that the high molecular weight component was a biotin binding protein that had remarkably similar physical and chemical characteristics as avidin [57], including a 33 % identity in the amino acid sequence [64].

Figure 1.3: Three-dimensional structure of streptavidin, acquired with x-ray diffraction methods [106]

In 1964, Chaiet and Wolf [21] published the first article about "The properties of Streptavidin, a Biotin-Binding Protein Produced by Streptomycetes". This was the first time a biotin-binding protein was isolated from a microbial source and not from egg white.

Streptavidin has its name from the bacterial source of the protein, *Streptomyces avidinii*, and from egg-white avidin. It is a tetrameric protein that consists of 254 amino acids. It has a size of $46 \times 93 \times 104\,\text{Å}^3$ [106] and a molecular weight of about 60 kDa [9]. Figure 1.3 presents the three-dimensional structure of streptavidin that was acquired with x-ray diffraction methods.

The exceptionally high binding affinity to biotin is in the same range as the binding affinity of avidin-biotin ($K_a \approx 10^{-15}\,M$) [64]. This is the highest known affinity without the formation of covalent bonds [57]. In order to understand these special properties and be able to use them for biotechnologic application, many groups investigated the streptavidin-biotin system.

The following section reviews the current state of the research on ligand-receptor bonds.

1.1.4 Ligand-Receptor bonds

The first step to understand interactions in cells and between cells is to understand interactions between the involved biomolecules. Besides DNA/RNA and antigen-antibody interactions, there are many proteins (receptors) and corresponding ligands that play a vital role inside and in-between cells. Because of their exceptionally high binding affinity, two of the most prominent ligand-receptor pairs are streptavidin-biotin and avidin-biotin. Both proteins have a tetrameric structure, so they can bind up to four ligands. Although many properties are valid for other ligand-receptor pairs, only these two ligand-receptor pairs were used in this thesis and, therefore, this section will focus on them.

During the last two decades, the rupture force between ligand and receptor was investigated with several different methods, such as Atomic Force Microscopy (AFM) [44, 97, 86, 122, 28, 134], Surface Force Apparatus (SFA) [63, 137], Dynamic Force Spectroscopy (DFS) [39, 91], Flow Chamber measurements [102] and relaxation experiments with magnetic nanoparticles [77]. Complementary to the measurements, computer-simulations were done by several groups [59, 70, 40, 65]. Figure 1.4 shows a single streptavidin-biotin pair and exemplarily the applied force in bond-force measurements.

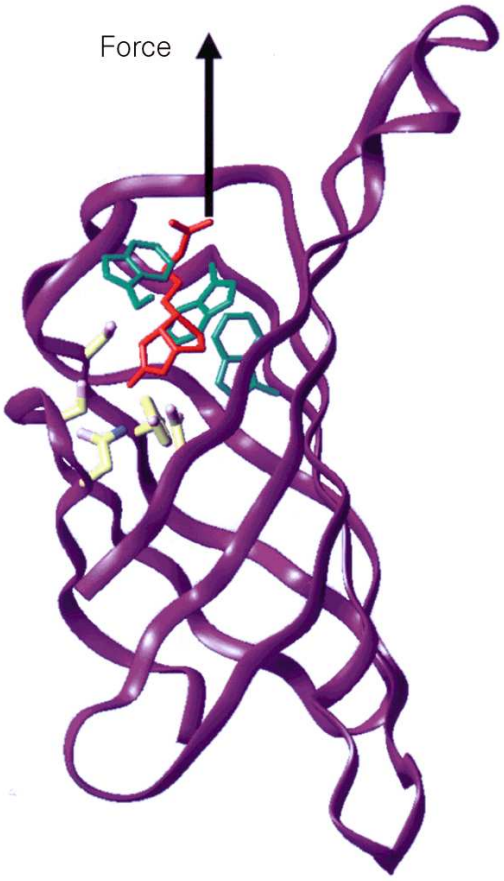

Figure 1.4: Sketch for streptavidin-biotin bond-force measurements, from [119]. A force is applied to biotin (red) to pull it out of the streptavidin.

Numerous measurements of the rupture force between ligand-receptor pairs were made with the AFM. In AFM experiments, the tip is coated by one part of the ligand-receptor pair and the other is fixed to a surface (e.g. an agarose bead [44]). After the tip contacts the surface and the ligand-receptor pair is bound, the tip

is retracted using the force spectroscopy mode. Under appropriate experimental conditions [123, 122], hundreds of single bond breaking events can be measured within a short time. But AFM measurements are somewhat limited, as shown in 1999 by MERKEL *et al.* [91]. They showed that the bond-force depends strongly on the rate of force increase F' [4]. Although this dependency was found with AFM measurements as well [134], only the DFS has the possibility to measure with loading-rates from 0.05 pN/sec to 60 nN/sec. Dynamic Force Spectroscopy, developed by EVANS *et al.* [39] in 1991, utilises biomembrane probes and is a potent method for the analysis of rupture events. DFS consists of two micropipettes that push two vesicles against each other. A vesicles contains low amounts of either receptors or ligands. The separation of the vesicles is analysed under a microscope, and video is recorded to calculate the rupture force.

In contrast to the AFM measurements, where the measured bond-forces where around 100 to 300 pN, it was possible to measure bond-forces of only 5 pN with the DFS [91]. Experiments with other techniques, also got results in between those values, which support the loading-rate dependency. In addition, this thesis presents experiments that confirm the dependency in the range of extremely low loading-rates (see chapter 4).

In a different approach multi-wavelength x-ray diffraction methods were used to obtain the specific structure of ligand-receptor pairs with ångstrøm precision [132, 64, 88, 46, 24]. Results of such x-ray diffraction methods can be seen in figures 1.2, 1.3 and 1.4.

In 1987 WEBER *et al.* [132] were the first group who fabricated streptavidin crystals and characterised the streptavidin-biotin complex with this method. Two years later HENDRICKSON *et al.* [64] made a comprehensive assay using a multi-wavelength anomalous diffraction method at an x-ray energy of 11921 eV. They found that the biotin is buried deeply inside the β-barrel of the streptavidin protomer. Only the carboxylate oxygens and the ureido-ring nitrogen protrude to the outside. Multitudinous hydrogen-bonds and van der Waals interactions are involved in the biotin binding. There are three hydrogen bonds to the carbonyl group buried within the barrel and also hydrogen bonds to the ureido nitrogens and carboxyl oxygens. Four tryptophan amino acids are in contact with each biotin molecule. Most of the interactions result from the residues of a given subunit, although one tryptophan is supplied by a subunit related to the R diad axis, which is vital for the tetramer integrity. This is an explanation for the reduced affinity with less than four ligands that was also found elsewhere [76, 113]. WEBER *et al.* [131] confirmed the results for streptavidin and apostreptavidin in 1992 and LIVNAH *et al.* [88] got similar results for the avidin-biotin complex

[4] The rate of force increase F', is called "loading-rate" in most papers, e.g. [91]

in 1993. In 1998, Chu *et al.* [24] presented a very convincing experiment, where they removed the polypeptide loop that undergoes an open to closed conformational change when biotin is bound. They showed that the deletion caused a large decrease of the affinity for the full ligand-receptor bond.

Although Jones and Kurzban [72] presented good evidence that the streptavidin-biotin binding is not cooperative[5] in the sense of the MWC-model[6], many other publications clearly indicate that the bond strength makes a step for the full bond. This can be seen as a positive cooperativity, as proposed by Williams *et al.* [133] and Sano *et al.* [113]. Besides the already mentioned x-ray diffraction experiments, these results were also supported by fourier-transform infrared spectroscopy and fluorescence spectroscopy [49].

All theoretical descriptions of ligand-receptor bonds and their breaking is based on the Transition-State-Theory (TST) and Kramers' model [15]. The TST was developed by Polanyi and Wigner in 1928 [103] and expanded by Eyring in 1935 [41]. Generally the classical TST describes any two physical states that are separated by a bottleneck in phase space. Two assumptions have to be made to apply the TST. First, the strong-coupling assumption, i.e. that all effects from a divergence of the thermal equilibrium are neglected, and second, the point of no return, i.e. that separated states do not reconnect. Even when these assumptions are applicable, TST can only give an upper bound to the true rate for any dividing surface [61]. Kramers' model describes a chemical reaction as a classical particle that moves in a one dimensional asymmetric double-well potential (confer to figure 1.5). A thorough description of Kramers' model can be found in [61].

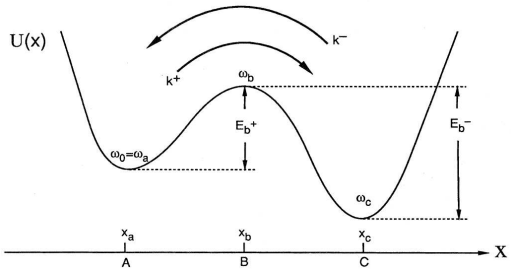

Figure 1.5: Asymmetric two-well potential U(x), used in Kramers' model. Escape occurs via the forward rate k^+ and the backward rate k^-. The corresponding activation energies are E_b^+ and E_b^-. Taken from [61]

The new experimental results about ligand-receptor bonds stimulated several theoretical works that extend the TST and Kramers' model. In 1996 Grubmüller *et al.* [59] presented computer-simulations of the streptavidin-biotin bond that matched their AFM measurements. The simulations supported their experimental results, that the measured bond-force increased with an increasing loading rate, and that the bond-force is around 280 pN

[5] Simple definition for *cooperativity*: An interaction of the constituent subunits of a protein causing a conformational change in one subunit to be transmitted to all others [67].

[6] A model by Monod, Wyman and Changeux for negative and positive cooperativity [95].

for a loading-rate of over 100 nN/sec. But they simulated an extremely stiff cantilever (the spring constant was nearly 20 times higher than in the experiments), the time-scale of force increase was nanoseconds rather than milliseconds (as in experiments) and only a streptavidin monomer has been simulated. In 1997 Izrailev *et al.* simulated the avidin-biotin bond and found very high rupture forces of up to 450 pN. They also presented a theoretical study that demonstrates that the nanosecond simulations can not reproduce thermally activated bond rupture that requires milliseconds. Also in 1997 Evans and Ritchie [40] published a thorough extension of Kramers' model to simulate force-activated bond rupture, and tested their model using smart Monte Carlo simulations. Additionally, they proposed a law for the exponential loading-rate dependency of the avidin-biotin rupture between 1 and 10^{20} pN/sec and 100 to 400 pN.

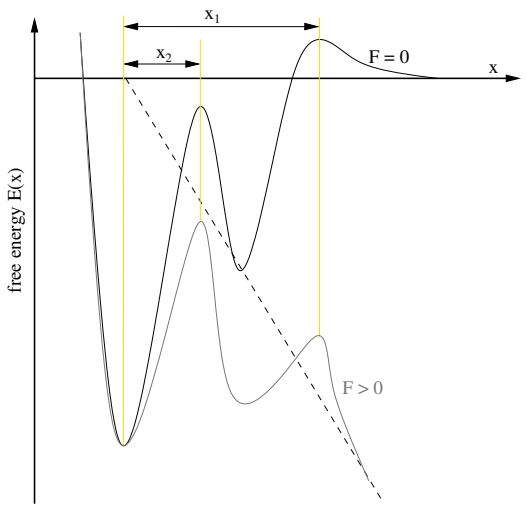

Figure 1.6: Conceptual energy landscape of a ligand-receptor bond. The dashed line represents an applied force that lowers the potential barriers and, therefore, the total width of the potential narrows ($x_2 < x_1$). Remade after [91]

As shown 2000 by Strunz *et al.* [121] the simplest possible model for ligand-receptor pairs has at least one intermediate state. Figure 1.6 illustrates such a model. Without any outer force the width of the potential (x_1) is wide. An applied force (represented by the dashed line) lowers the outer barrier and therefore the inner barrier with a narrower potential width (x_2) is relevant for the bond rupture properties. For the narrowing of the potential width a linear lever rule is valid: The smaller the potential width, the higher the rupture force. These models can only be applied if there is a single preferred path for the reaction [15], which was shown experimentally by Freitag *et al.* [45]. Such a model was introduced in 1978 by Bell [8] and used e.g. by Merkel *et al.* to explain the loading-rate dependency of the ligand-receptor bond in 1999. Experimental data from bond-force measurements can be fitted to a linear function [121]:

$$F = \frac{k_\mathrm{B}T}{x_\beta} \ln \frac{x_\beta \cdot r}{k_\mathrm{B}T \cdot k_\mathrm{off}} \tag{1.1}$$

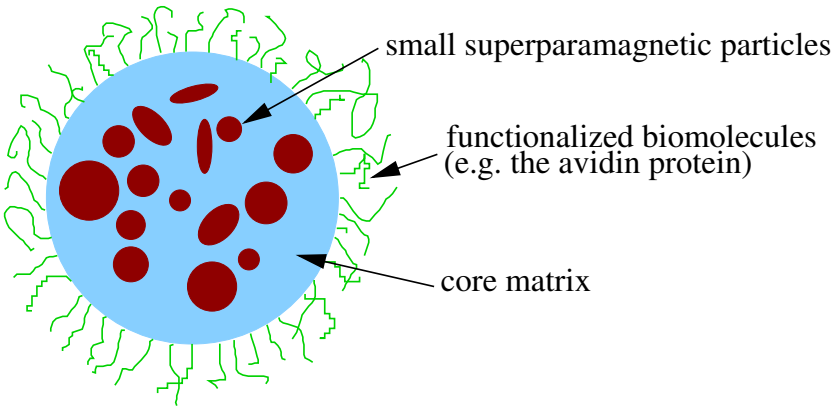

Figure 1.7: Sketch of a typical magnetic marker

where $k_{\mathrm{B}}T = 4.114\,\mathrm{pN\,nm}$ is a Boltzmann factor at 298 K, r is the loading-rate, x_β is the potential width (see above) and k_{off} is the natural off rate.

1.2 Functionalised magnetic markers

Today magnetic markers are widely used in biotechnological applications. They were originally developed by DYNAL BIOTECH to segregate specific biomolecules from a given solution [114]. The magnetic markers (also known as particles or beads) are specifically functionalised to bind to the target analyte and mixed with a solution. After the biomolecules are bound to the markers, the markers are removed from the solution by using a magnet. Because this method proved very successful, many companies offer a wide range of different magnetic markers. The commercially available markers differ in size from several nanometer to a few microns and in composition from pure Co to magnetite particles enclosed in different matrix materials.

For choosing the most suitable particles from this wide variety, the requirements of the experiments have to be clear. The experiments presented in this thesis demand several attributes for the beads. First of all, the particles should have a high magnetic moment to be able to apply high forces to the beads. But because we want to manipulate single beads, they are not allowed to cluster. Therefore, the beads must be superparamagnetic and can't be ferromagnetic. Second, the particles are not allowed to be smaller than half the wavelength of light ($\lesssim 300\,\mathrm{nm}$), because they are tracked with an optical microscope. Third, the particles must not bind unspecifically to the sample surface (mostly SiO_2). This is especially important for all bond-force

Company	Chemagen	Seradyn	Micromod
Product No.	M-PVA SAV1	30152104011150	39-18-153
Matrix material	polyvinyl alcohol	polystyrene	silicate
Magnetic material	Fe_3O_4	Fe_3O_4	Fe_3O_4
Diameter in μm	1	0.779	1.5
Particle density	n.s.	1.5 g/ml	4 g/ccm
Share of magn. mat.	50-60 %	40 %	n.s.
Magnetic moment m	1.82 fAm^2	0.88 fAm^2	0.4 fAm^2

Table 1.1: Properties of the magnetic particles used in this thesis [22, 115, 92]. The magnetic moment m at 100 Oe is measured with AGM, see section 2.6. (n.s.: not specified)

measurements. If there would be unspecific bonds to the surface, it would always be unclear if the rupture force corresponds to the bond in question, or just to an unspecified bond. Therefore, we tested 12 different magnetic markers on several surfaces in order to find out, if they adhere to the sample surface or not (confer section 4.4).

There are still many different commercially available beads that comply with these requirements. Figure 1.7 presents a sketch of a commonly used magnetic marker. The markers consist of superparamagnetic material enclosed by a matrix material and are functionalised on the outside with biomolecules.

According to the requirements stated above, three kinds of particles from three different companies are chosen. One might think that some matrix materials adhere to the surfaces and others don't. Our tests do not support this assumption, and so all three kinds of particles have a different matrix material. The beads used in this thesis have polystyrene, polyvinyl alcohol or silicate matrices. The magnetic material of all used markers is magnetite (Fe_3O_4). The biomolecules on the outside can be chosen as needed. For the bond-force measurements presented in chapter 4, we used beads functionalised with avidin or streptavidin.

Table 1.1 presents the main properties of all three types of magnetic particles that were used for the bond-force measurements. The mean diameter ranges from 0.8 μm to 1.5 μm, which can be verified by Scanning Electron Microscopy (SEM) imaging. Figure 1.8 shows SEM images of all three particle types that were used for the bond-force measurements. The markers of one kind do not always have the same size (see e.g. figure 1.8b), and all three types have different surfaces. While the Micromod particles seem to have a very slick surface with other substances intermixed inbetween the beads,

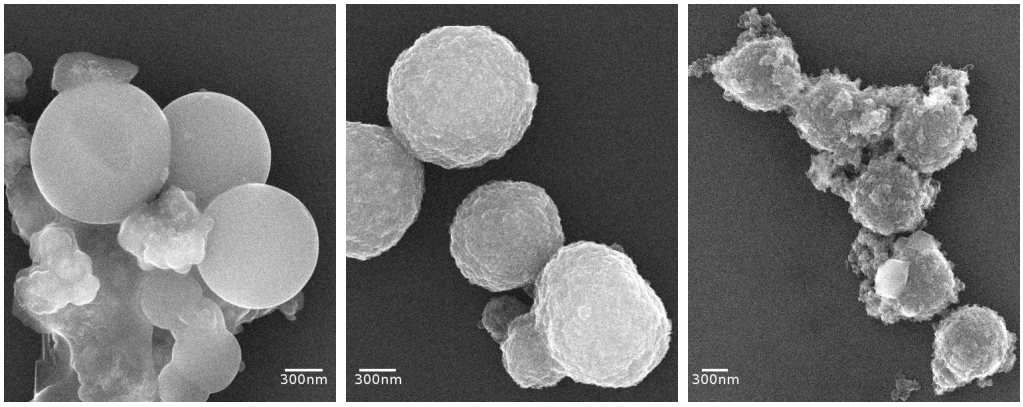

(a) Micromod particles. (b) Chemagen particles. (c) Seradyn particles.

Figure 1.8: SEM images of three different kinds of magnetic particles

the CHEMAGEN particles have a more fleecy surface and there is nothing else in the solution. One possible reason is that the different matrix materials of the particles have a different contrast in the SEM. Other possible reasons are a different amount of biomolecules attached to the markers or a different method to attach the biomolecules.

Although the micron sized magnetite particles work well for the presented experiments, there is still room for improvements. Using nanoparticles instead of micron sized particles would greatly improve the binding capacity. Smaller markers would also reduce interfering effects in the behaviour of the biomolecules. But the magnetic moment should still be as high as possible. Single domain particles made of Co, FeCo or FePt with a diameter of only a few nanometers would meet these requirements, and such particles were already manufactured, e.g. by Hütten *et al.* [68]. But there are still several problems with such small markers. For example, Co particles are probably not biocompatible and need, therefore, some coating for the use in biological systems. Furthermore the functionalisation of small metallic particles is not trivial, especially because the surface properties change the particle properties, too. So for these nanoparticles, there is still a lot of research to be done.

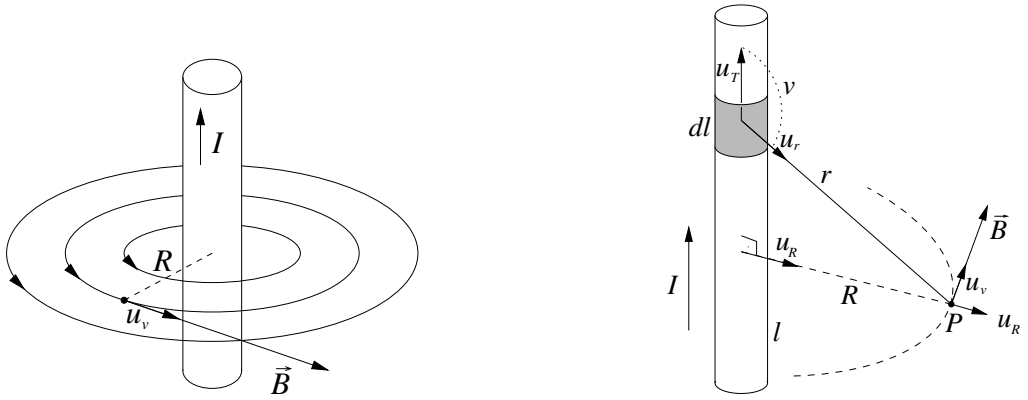

(a) Magnetic field lines around a rectilinear current

(b) Magnetic field at point P produced by a rectilinear current

Figure 1.9: Magnetic fields of a rectilinear current, remade after [1]

1.3 Magnetic fields generated by conducting lines

This section is an introduction to the theory of the magnetic field around a current carrying conducting line and the forces acting on a magnetic marker inside the produced magnetic gradient field. Additionally, some basic ideas about the manipulation and positioning of a magnetic markers with conducting lines will be discussed.

A straight current generates a magnetic field that is inverse proportional to the radius R. The field lines are concentric circles orthogonal to the straight current, see figure 1.9(a). To calculate the magnetic field of a straight current we start from the Ampère-Laplace law:

$$\vec{B} = \frac{\mu_0 I}{4\pi} \oint \frac{\vec{u_T} \times \vec{u_r}}{r^2} dl \tag{1.2}$$

with the unit vectors $\vec{u_T}$ and $\vec{u_r}$, $\mu_0 = 4\pi \cdot 10^{-7} \frac{mkg}{C^2}$ and assuming a constant current density. As shown in figure 1.9(b), the vector $\vec{u_T} \times \vec{u_r}$ is for every point P and every element dl perpendicular to the plane which is determined by P and the current I. Hence $\vec{u_T} \times \vec{u_r}$ equals $\vec{u_\nu}$. The magnetic field at point P, originating from dl, is tangent to the circle of radius R that passes through P. It is centered on the current and it is in a plane perpendicular to the current. So, when we integrate equation 1.2 all contributions in the

integral have the same direction $\vec{u_\nu}$, and the resultant magnetic field $\vec{B}$ is also tangent to the circle. Thus, it is only necessary to find the magnitude of $\vec{B}$. The magnitude of $\vec{u_T} \times \vec{u_r}$ is $\sin\nu$, because both vectors are unit vectors. Therefore, we get for the magnitude of a rectilinear current:

$$B = \frac{\mu_0 I}{4\pi} \int_{-\infty}^{\infty} \frac{\sin\nu}{r^2} dl \tag{1.3}$$

It can be seen in figure 1.9(b) that $r = R\cos\nu$ and $l = -R\cot\nu$ thus $dl = R\frac{1}{\sin^2\nu}\, d\nu = R\csc^2\nu\, d\nu$. Hence we get

$$B = \frac{\mu_0 I}{4\pi} \int_0^{\pi} \frac{\sin\nu}{R^2\csc^2\nu}(R\csc^2\nu\, d\nu) = \frac{\mu_0 I}{4\pi R} \int_0^{\pi} \sin\nu\, d\nu \tag{1.4}$$

With $l = -\infty$ corresponding to $\nu = 0$ and $l = +\infty$ corresponding to $\nu = \pi$ we get the law of Biot-Savart:

$$B = \frac{\mu_0 I}{4\pi R}(\cos\nu)_0^{\pi} = \frac{\mu_0 I}{2\pi R} \tag{1.5}$$

or in vector form

$$\vec{B} = \frac{\mu_0 I}{2\pi R}\vec{u_\nu} \tag{1.6}$$

After we can calculate the magnetic field B at every point around a long and thin conducting line, we also want to set a superparamagnetic marker inside this magnetic field and calculate the acting forces.

Figure 1.10 shows a simplistic setup for a magnetic particle on a surface near a conducting line. When we neglect different heights of the center of the magnetic particle and the center of the conducting line, this is only a two-dimensional problem. While the current flows in-plane through the conducting line, the magnetic field is always perpendicular to the plane and so it is easy to calculate the magnetic field for every point in the plane. When the current is turned on in this simple setup, a magnetic field is generated that affects the magnetic particle. In the case of ferromagnetic markers with large anisotropy, the markers would start to rotate in order to align themselves to the magnetic field, as the dipole wants to go into the state of minimal energy [29]. The magnetic torque forced on the marker is $\vec{\tau} = \vec{m} \times \vec{B}$.

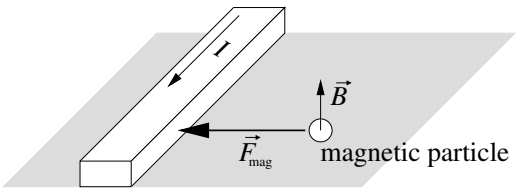

Figure 1.10: Sketch of a simple setup to manipulate a magnetic marker with a conducting line on a surface.

But in this thesis, only superparamagnetic markers were used. The ferromagnetic crystallites inside the core of the markers are so small (≈1-10 nm) that they show superparamagnetic behaviour. In such small crystallites, the thermal energy is sufficient to change the direction of the magnetisation, so the overall magnetic moment averages to zero. Therefore, the crystallite exhibits a behaviour similar to paramagnetism, where the magnetic moment M follows the langevin equation:

$$M(x) = N \cdot \coth(x) - \frac{1}{x} \tag{1.7}$$

with $x = \frac{\mu_0 H}{k_B T}$. In an outer magnetic field, the magnetic moment in the crystallite instantaneously aligns to the outer magnetic field, and, therefore, generates an own outer magnetic field. The net magnetic field of the superparamagnetic markers increases with a higher outer field until all magnetic moments are aligned, and the magnetic moment is saturated. So, in a magnetic gradient field, as generated by the conducting line, the markers additionally feel a translational force $\vec{F}_{\text{mag}}$ in the direction of the magnetic gradient.

The change of the magnetic moment of the markers is very small for the applied outer fields. Therefore, it is only a small error when we assume the marker as a constant magnetic dipole for the bond-force measurements (see chapter 4). The force exerted on the marker can then be written as [71]:

$$\vec{F}_{\text{mag}} = \nabla(\vec{m} \cdot \vec{B}) \tag{1.8}$$

With the assumption that the magnetic dipole moment instantly aligns to the outer magnetic field and the particle adheres to the surface in the same position, the vector product reduces to a scalar product. The magnetic force can then be written as:

$$\vec{F}_{\text{mag}} = |\vec{m}|\nabla|\vec{B}| = m \cdot \frac{dB}{dR} \tag{1.9}$$

Together with equation 1.5 we get:

$$\vec{F}_{\text{mag}} = \frac{m \cdot \mu_0 I}{2\pi R^2} \tag{1.10}$$

To hold a particle in a specified position, a trap must be build with the magnetic fields. But according to Earnshaws theorem, it is not possible to build a trap with any combinations of outer magnetic fields. Samuel Earnshaw already proved in 1842 [36] that if inverse-square-law forces, such

as the magnetic force $\vec{F}_{\mathrm{mag}}$, govern a group of charged particles, they can never be in stable equilibrium. The reason for this is that inverse-square-law forces follow the Laplace partial differential equation, and the solution of this equation does not have any local maxima or minima. There are only saddle-type equilibrium points, instead. Although not applicable for the experiments in this thesis, in principle one can circumvent Earnshaw's theorem by using time-varying fields, active-feedback systems, diamagnetic systems (extremely low forces) or superconductors.

Naturally one would like to guide a particle between the conducting lines that create the magnetic field. But this is only possible for particles that follow the magnetic gradient to local minima. This was e.g. done by DEKKER *et al.* [30] to guide neutral atoms on a chip. But the magnetic particles used in this thesis follow the magnetic gradient to the local maxima, and the local maxima are always at the edges and in the corners of the conducting lines.

So, in the experiments in this thesis, we trapped particles at the crossing of two conducting lines or in a corner (see chapters 3 and 5).

1.4 Computer-simulations of the magnetic fields

To visualise the magnetic fields around arbitrary conducting lines, a computer simulation program was written. Because the magnetic field $\vec{B}$ is always perpendicular to the sample plane (confer figure 1.10) the program only needs to calculate the magnitude of the magnetic field, which reduces the problem to two-dimensions (please see the CD for the source code of the simulation program).

The following variables have to be defined for the computer-simulations to calculate the magnetic fields. First of all, a matrix of $n \times m$ grid points is set and the size of one grid point is defined. Then, the conducting lines are set into the matrix by defining the start- and endpoint of the conducting line. Additionally, the width of the conducting line and the current through it is set. Finally, the number of iterations per gridwidth for the conducting lines is set. So the conducting line is cut into many pieces, and for every piece the mag-

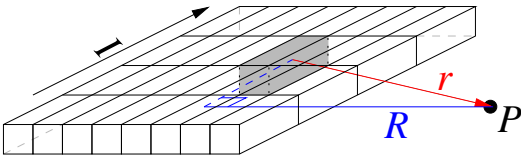

Figure 1.11: Sectioning of the conducting line for the simulation program showing the magnetic field at point P generated from one section (confer figure 1.9b)

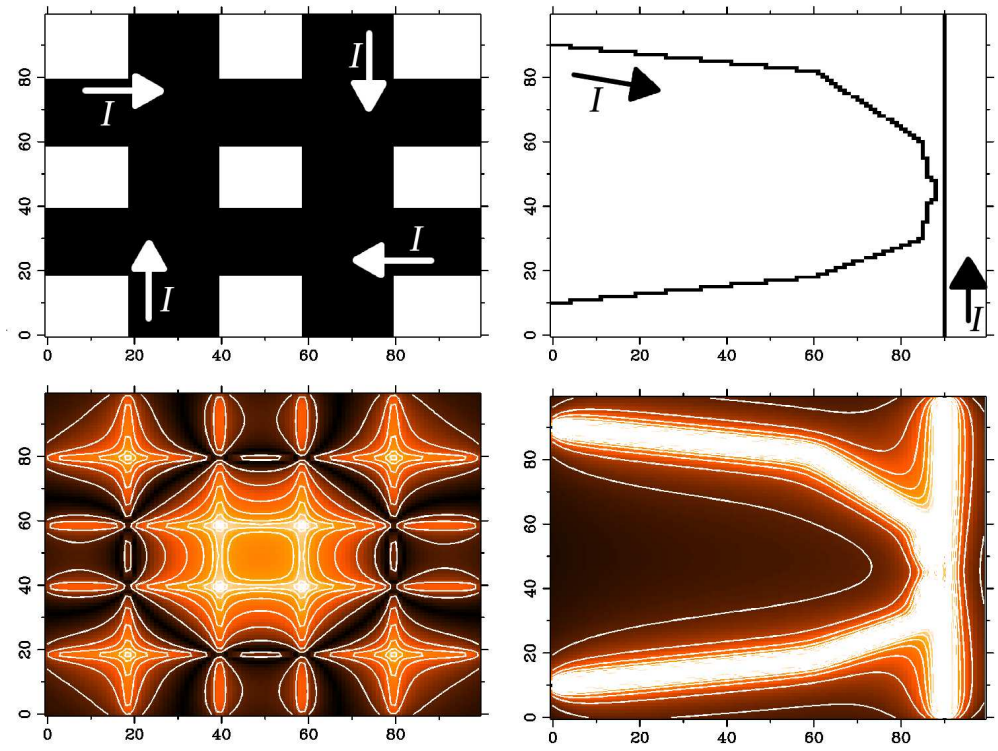

(a) Four crossing lines that are not connected to each other

(b) A curved line in vicinity to a straight line

Figure 1.12: Results from the the simulation program. The top images show the defined conducting lines with the direction of the currents, and the bottom images show the normalized magnetic field.

netic field is calculated at every gridpoint P with the law of Biot-Savart (see figure 1.11). The accuracy of the output can be tested by incrementing the iterations per gridwidth until the output doesn't change significantly and by comparing with analytic solutions of model problems.

The output of the program is a matrix, containing the magnitude of the magnetic field for every grid point. The resulting matrix can then easily be normalised and displayed as a coloured images. Figure 1.12 shows two examples of the computer-simulations. The top image shows the defined conducting lines and the bottom image the normalised magnetic field. The magnetic field changes in the bottom images from low (black) to high (white). The images also show lines of equal magnetic fields to enhance the visibility.

It is easy to spot the gradient that is perpendicular to the equipotential lines. As can be seen in figure 1.12(a), the corners of crossing conducting lines have the highest magnetic field and are local maxima. The inner corners have higher fields due to higher fractions of all four lines, although the outer corners are still local maxima. In figure 1.12(b) it can be seen that the magnetic gradient points to the smallest distance between the two conducting lines.

Although the program was a good starting point to develop the different designs that were used for the conducting lines in this thesis, it is neither fast nor sophisticated enough to calculate a complete setup in a reasonable time. Furthermore, it would be advantageous to be able to simulate the influence of the viscosity together with the magnetic force in order to gain insight in the real flowing behaviour of a bead. A professional finite-element simulation program would be more suitable for such a task.

1.5 Magnetic Tunnel Junctions

Since the discovery of the Tunnel Magneto Resistance (TMR) in 1975 [73] and especially in the last two decades, the interest in Magnetic Tunnel Junctions (MTJ) grew quickly. Besides the work to create a Magnetic Random Access Memory (MRAM), MTJs were already used for magnetic biosensor applications [114]. This section will introduce the basic theory needed for a description of MTJs.

1.5.1 Tunneling effect

The electron tunneling effect is a purely quantum-mechanical effect and first theoretical studies were published in the early 1930s [117]. Although the TMR effect was discovered early in 1975 [73], it took two more decades, and the discovery of the Giant Magneto Resistance (GMR) [5, 12], until the interest in the TMR effect grew quickly.

Figure 1.13(a) shows the wave function $\Psi(x)$ of two electrodes separated by an insulating barrier. Although classically forbidden, a part of the wave function continues beyond the barrier. Because the wave function has to be continuous, it decays exponentially within the insulator. If the barrier is too thick, the wave function vanishes beyond the barrier.

In a MTJ the electrons tunnel only through thin insulating barriers (only a few nanometers thick) and, therefore, a reasonable tunneling current can be measured. Those metal/insulator/metal systems are mostly analysed by measuring the current/voltage (I/V) characteristic. Figure 1.13(b) shows a

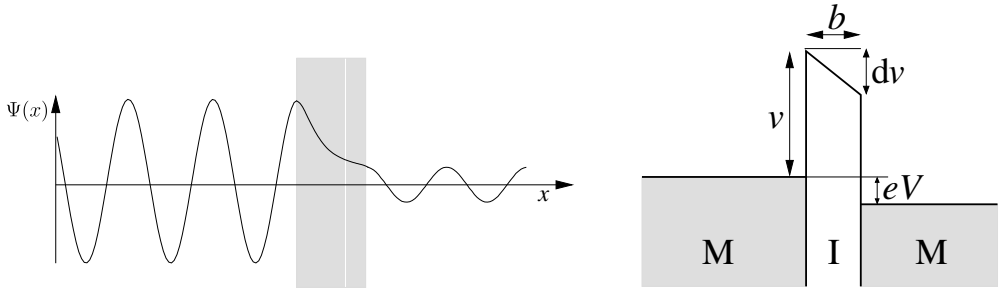

(a) Wave function $\Psi(x)$ for electron tunneling through an insulating barrier. While the barrier would classically be forbidden, quantum-mechanically the wave function decays exponentially and, for thin barriers $\Psi(x)$, is attenuated beyond the barrier.

(b) Sketch of a M/I/M model with an applied bias Voltage eV. The barrier height ν, the thickness b and the asymmetry dν can be obtained from a Brinkmann fit.

Figure 1.13: Tunneling in metal/insulator/metal (M/I/M) structures, from [84]

sketch of such a system. The Fermi-levels E_F of the two metals are shifted because of the applied bias Voltage eV. The tunneling through an insulator mainly depends on the the density of states (DOS) in the left and right electrode. The current from the left to the right electrode can be written as:

$$I_{l\to r}(E) = \int_{-\infty}^{\infty} \rho_l(E)\cdot\rho_r(E+eV)\cdot|T(E)|^2\cdot f(E)\cdot(1-f(E+eV))dE \quad (1.11)$$

where ρ_l is the DOS in the left electrode at energy E and ρ_r is the DOS at the same energy plus the applied bias voltage. $|T(E)|^2$ is the probability of transmission through the barrier and $f(E)$ the Fermi-Dirac function. Because electrons also tunnel in the other direction, you have to subtract the current from right to left to get the total current $I_{total} = I_{l\to r} - I_{r\to l}$.

While the easiest way to get the properties of the barrier is the Simmons-fit [116], which assumes a rectangularly shaped barrier, in this thesis the more elaborate Brinkman-fit is used. Brinkman *et al.* [17] used the WKB-approximation to numerically calculate the transmission probability $|T|^2$ for a trapezoidally shaped barrier. The first terms of the WKB-approximation give for the conductance: $G = A\cdot V^2 + B\cdot V + C$. So when the conductance is measured, the barrier parameters can be obtained by fitting the parameters A,B and C:

$$\nu = \frac{e^2 C}{32A}\ln^2\left(\frac{h^3}{\sqrt{2}\pi e^3 m_{\text{eff}}}\sqrt{AC}\right) \quad (1.12)$$

$$b = -\frac{\hbar}{2\sqrt{2m_{\text{eff}}\nu}} \ln\left(\frac{h^3}{\sqrt{2}\pi e^3 m_{\text{eff}}}\sqrt{AC}\right) \tag{1.13}$$

$$d\nu = -\frac{12\hbar\nu^{\frac{3}{2}}B}{\sqrt{2m_{\text{eff}}}ebC} \tag{1.14}$$

with the effective electron mass m_{eff} set to 0.4 [16]. Although Brinkmans approach neglects any dependence of the transport characteristics on the DOS of the electrodes, equation 1.13 provides good results for the barrier thickness. In the experiments, the I/V curve of a MTJ is measured, numerically differentiated and fitted with a standard code [104].

1.5.2 Tunnel Magneto Resistance

In 1975, Julliere [73] was the first one who measured TMR in MTJs. He already gave a simple explanation for the TMR effect and defined a and a' as the fractions of tunneling electrons in the two ferromagnetic materials that are parallel to the magnetisation. With the spin polarisations of the two ferromagnets defined as $P = 2a-1$ and $P' = 2a'-1$, the relative conductance variation is defined as:

$$\text{TMR} = \frac{2PP'}{1-PP'} \tag{1.15}$$

Jullieres explanation is just a very simple model for the TMR and does not include temperature or voltage dependencies. For two different ferromagnetic electrodes in a MTJ, the model also gives a wrong positive sign for the polarisation of the 3d-ferromagnets. There are more open questions, e.g. the connection between the spin-polarisation of the different electron bands to the measured TMR ratio, and until today, there is no comprehensive theory about it. The interested reader is encouraged to read the article from Stearns [120] and the PhD thesis of LeClair [84], where some more elaborate approaches are summarised.

1.5.3 Exchange Bias

The exchange bias was discovered in 1956 by Meiklejohn and Bean [89, 90] as a new type of magnetic anisotropy. They found an unidirectional pinning of a ferromagnetic layer by an adjacent antiferromagnetic layer. When the ferromagnet in contact with the antiferromagnet is cooled from above the Neél temperature in an outer magnetic field, there is a shift from zero along the field axis in opposite direction of the applied field. This unidirectional shift is called exchange bias and it means that there is a preferred magnetisation direction for the ferromagnetic layer.

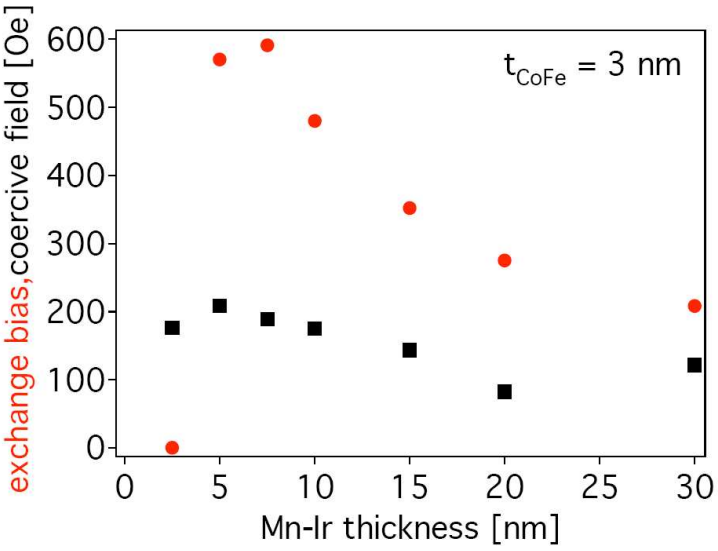

Figure 1.14: Exchange bias and coercive field of a CoFe layer in dependence on the MnIr thickness. From [124]

The exchange bias depends strongly on the thicknesses of the ferromagnetic and the antiferromagnetic layer. Figure 1.14 shows the dependence on the antiferromagnetic layer thickness for MnIr in contact with a CoFe layer as the ferromagnet. There clearly is a maximum exchange bias at a MnIr thickness of 7.5 nm, which is typical for MnIr (see e.g. [2]). Such an exchange bias can also be impressed into an antiferromagnet-ferromagnet system by sputtering the thin layers within a magnetic mask, as it is done in this thesis (see chapter 6).

Chapter 2

Preparation and analytical tools

This chapter describes all techniques that are needed for the preparation of the samples and the methods to analyse the samples. The principle of every technique is described shortly and the used apparatus in more detail. For a comprehensive overview, the reader is pointed to the corresponding references. The exact preparation steps for the different samples will be elaborately explained in the corresponding chapters 3 – 6.

2.1 Sputtering thin films

Sputtering was used in this thesis for the thin films of MTJs, conducting lines, contact pads and protection layers. The first publication about sputtering is from Grove in 1852 [58], but it took a long time until the micro-electronics demanded the sputtering technique for the production of good metal films. While a general description of the sputtering process can be found in [101] and [75], this section will focus on the used apparatus and their settings for the different films.

All thin films of the MTJs (see chapter 6) were sputtered in the fully automated commercial sputter system CLAB 600, made by Leybold Dresden (see figure 2.1(a)). This system is equipped with six 4" magnetron sputter sources and one 2" magnetron sputter source. Two of the 4" sources are special DC-magnetron sources for ferromagnetic materials and one 4" source is a RF sputter source for MnIr. The other sources are regular DC-magnetron sputter sources. The base pressure in the sputter chamber is at least $3.5 \cdot 10^{-7}$ mbar. During sputtering, argon is let into the chamber and the process pressure is kept constant at $1.3 \cdot 10^{-3}$ mbar by adjusting the shut-

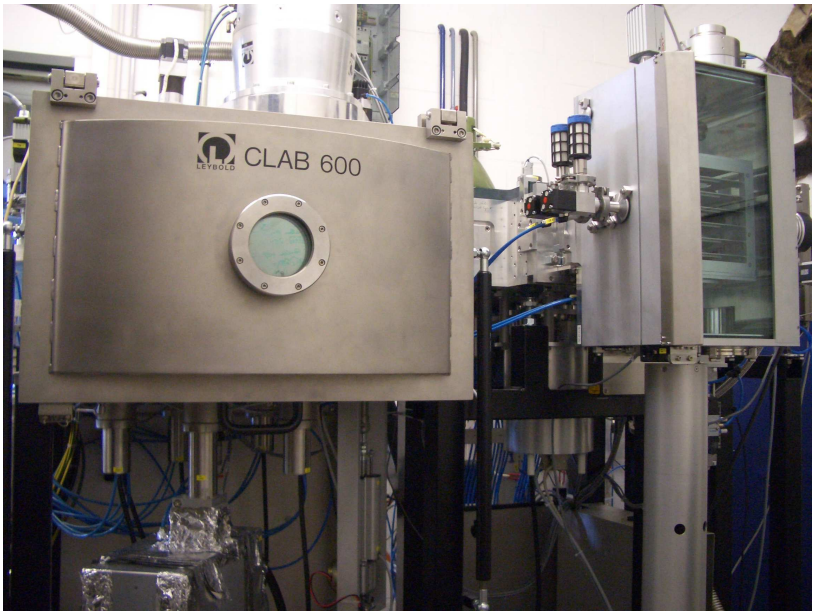

(a) Commercial sputter system CLAB 600, made by LEYBOLD

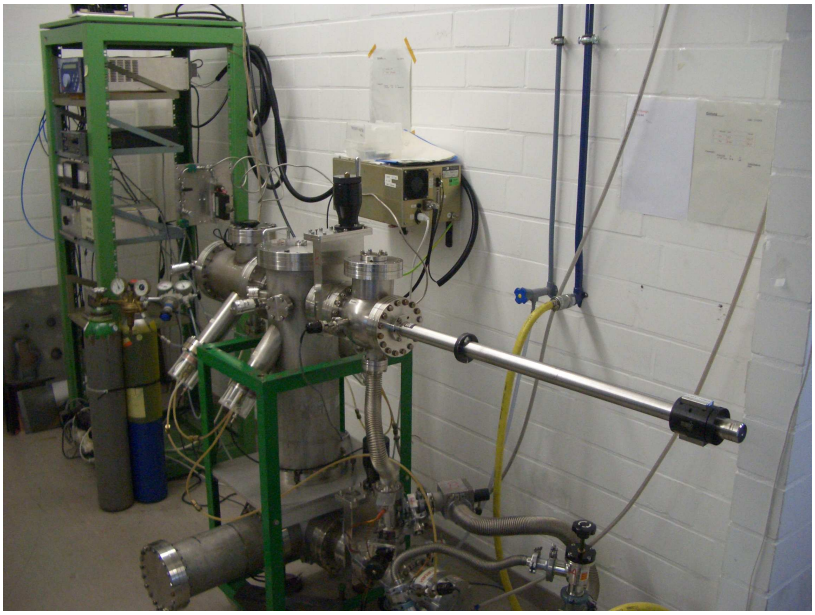

(b) Home made sputter system, used for SiO_2, Tantalum and Gold

Figure 2.1: Sputtering systems used in this thesis

ter in front of the main turbo pump. The sputter power is 115 W for all targets except Gold (the 2" source) with 29 W. Changing the target materials, installing magnetic masks or wobble mask inside the sputter system is easily possible within a few hours. The layer thicknesses of the materials were frequently calibrated through x-ray diffraction methods or atomic force microscopy (AFM) [62].

The insulating barrier of the MTJ is processed inside the CLAB 600 without vacuum breach. The barrier consists of 1.4 nm Aluminium, that is oxidised for 100 sec in an ECR[1] oxygen plasma source, made by Roth & Rau. At the best parameters [124] of $3 \cdot 10^{-3}$ mbar oxygen pressure, a microwave power of 275 W and a DC bias voltage at the sample of −10 V relative to the chamber, the aluminium transforms into an amorphous 1.8 nm thick Al_2O_3 barrier.

In the MTJs which are prepared during this thesis, the ferromagnetic layers are pinned to an antiferromagnetic layer (MnIr) by exchange bias. Normally, the exchange bias is activated by heating the sample over the Neèl temperature and cooling down the sample in a homogeneous magnetic field. But with this technique, it is not possible to pin the top and bottom ferromagnetic layers in different directions. Therefore, the exchange bias is activated by sputtering the layers below and above the barrier in two different magnetic masks.

Figure 2.1(b) shows the home built sputtering system that is used for conducting lines, contact pads (Ta, Au) and protection layers (SiO_2). With a base pressure of at least $2 \cdot 10^{-6}$ mbar, Tantalum and Gold is deposited at $2.1 \cdot 10^{-3}$ mbar argon pressure with a power of 25 W. The protective SiO_2 layers are RF-sputtered from a silica glass target in a gas mixture of $2.1 \cdot 10^{-3}$ mbar argon and $1.1 \cdot 10^{-4}$ mbar oxygen at a power of 50 W.

2.2 Ion beam milling

Ion beam milling is very similar to sputtering, but the sample is now the target. So the top layers of the sample will be etched down by Ar^+-ions that are accelerated towards the sample. Ion beam milling is used for several different process steps during the creation of the MTJs (confer chapter 6) or to embed the conducting lines into the Si-wafer (chapters 3 – 5).

The ion beam milling is also done in a apparatus built in Bielefeld. It has a base pressure of at least $2 \cdot 10^{-6}$ mbar and an argon pressure during the etching of $8 \cdot 10^{-4}$ mbar. The ion source is operated at a discharge voltage

[1] ECR is the abbreviation for: electron cyclotron resonance

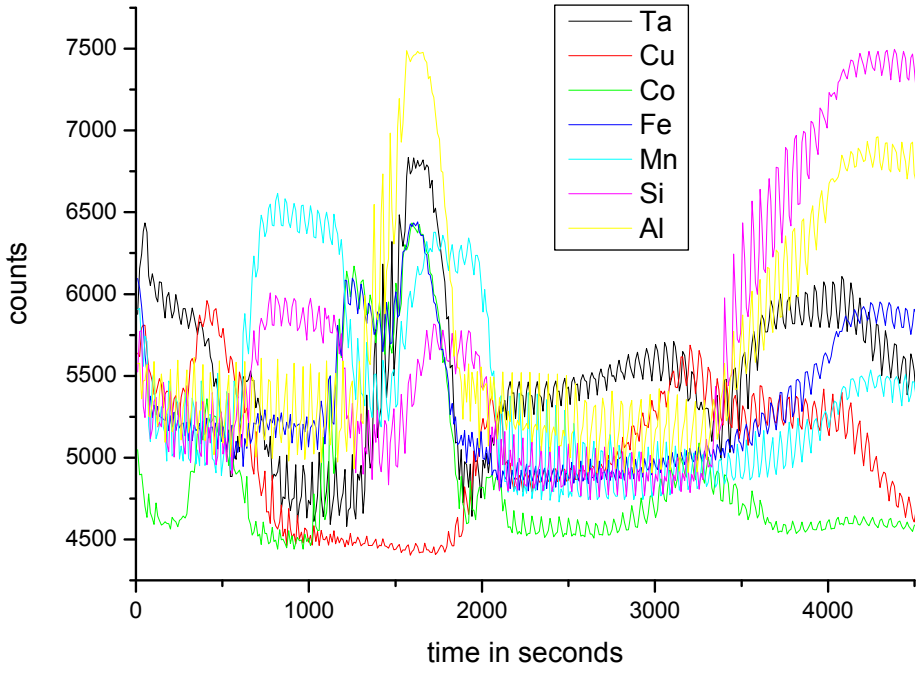

Figure 2.2: Full recorded spectrum of the layer stack TMR-DP15 from the quadrupole mass spectrometer. Because the channels for different masses are not fully separated, some artefacts occur (e.g. the rise of Al at the end of the spectrum is only related to the Si peak).

of 50 V, a beam voltage of 400 V, an accelerator voltage of 30 V and with a beam current of 6 mA. The sample current is measured and kept at about 400 μA to keep the etching rate constant. To ensure homogeneous etching and to avoid short-circuited TMR elements, the sample holder is tilted by 30° and rotates slowly. A comprehensive description of the apparatus can be found in [101].

The etching is monitored with a quadrupole mass spectrometer, which allows to stop the process exactly in the desired layer of the stack. Figure 2.2 shows a recorded layer stack as it is used in chapter 6 of this thesis. The Al_2O_3 can easily be seen at around 1600 sec. After etching the complete layer stack, the process time for the TMR-elements and the bottom electrodes can easily be calculated.

2.3 Optical lithography

Optical lithography is used extensively in this thesis. All conducting lines, contact pads and TMR test structures are made with optical lithography. In principle, the lithography always consists of the following steps: a) spin-coating the resist on top of the sample, b) annealing the resist, c) exposing desired parts to light of a specific wavelength and d) developing the resist. These steps transfer a given structure to the resist on top of the sample. Depending on the resist type, the resist is preserved in the exposed area (negative resist) or in the non-exposed area (positive resist). The resist protects some parts of the sample surface, and on the other part thin films can be deposited or can be etched with Ar^+-ions. Afterwards the resist is removed by suitable solvents.

The positive photoresist AR-P 5350 from ALLRESIST GmbH is used for all optical lithography. It is spin-coated at 4000 rpm (or 6000 rpm for mask lithography) for 30 secs and annealed for 30 min at 92 °C. Then, the resist is exposed with a laser lithography or a UV-mask lithography system. Afterwards, it is developed for 45 sec with the ALLRESIST developer AR 300-35 (mixed 2:1 with H_2O). Because of the special undercut profile of this resist, the real structures are about 1 μm wider than specified in the design file. After all necessary steps, the resist is removed with the ALLRESIST remover AR 300-70 in an ultrasonic bath for 15 mins.

The used laser lithography system is a DWL 66 from HEIDELBERG INSTRUMENTS GmbH with a laser from MELLES GRIOT and a 4 mm write head. The laser has an output of 90 mW at 442 nm. A built in camera easily allows the alignment to already existing structures. The minimum possible size of the structures with the used photoresist is 1 μm. This laser lithography system is also used to fabricate UV-masks that can be used with the UV-mask lithography process. For such masks, the design is inverted and structured on a glass substrate. To block the UV-light, a thick tantalum layer is sputtered in the created holes. After lift-off, the mask is complete and can be used for very quick parallel optical lithography.

For one-step lithography with structure sizes larger than 5 μm, a UV-mask lithography system from THERMO ORIEL is used. The homogeneous UV light source with 300 W exposes the sample through the mask that lies on top of the sample. The exposure time is between 3 and 5 secs, depending on the age of the UV-lamp. Figure 2.3 shows the design of the used TMR standard mask with

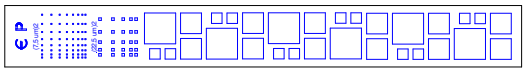

Figure 2.3: Design of the TMR standard mask.

squares that define areas of 90000 μm^2, 40000 μm^2, 10000 μm^2, 506.25 μm^2 and 56,25 μm^2.

2.4 E-beam lithography

The principle of e-beam lithography is the same as the optical lithography. Instead of photons, high energetic electrons are used which have a much shorter wavelength and, therefore, allow to write much smaller structures. The negative resist AR-N 7500/18 from ALLRESIST is used in this thesis. After a spin-coating at 6000 rpm and annealing at 85 °C for 2 mins, the sample is exposed at 20 kV in a LEO SERIES 1530 Scanning Electron Microscope (SEM) with a RAITH ELPHY PLUS lithography system. The minimal possible structure size is about 50 nm and depends on the resist. For all e-beam lithography steps the developer AR 300-47 (4 min) from ALLRESIST and the remover 1-Methyl-2-pyrrolidinone (1 h in an ultrasonic bath at 80°C) from ALDRICH is used.

The SEM is also used to analyse samples [126]. The energy, the aperture and the detector type (In-lens or SE2) can be adjusted to suit the investigated sample. The nominal resolution is 1 nm at 20 kV. Figure 1.8 on page 19 shows SEM images of the magnetic beads.

2.5 Auger electron spectroscopy

For detailed examination of TMR layer stacks and a special surface test (see section 4.1) a Scanning Auger Microscope (SAM) SYSTEM 660 from PHYSICAL ELECTRONICS was used. This system has an integrated SEM for the positioning on a sample and uses an integrated ion beam milling system to acquire depth profiles of samples. Using only Auger electrons with an energy between 30 eV and 2000 eV for the mass determination the SAM has a very high depth resolution. A comprehensive description of this system and the method can be found in [111].

2.6 Alternating Gradient Magnetometer

For the manipulation of magnetic particles, it is very important to know their magnetic moment. This was measured with the Alternating Gradient Magnetometer (AGM) MICROMAG 2900 from the PRINCETON MEASUREMENT CORPORATION. The maximum magnetic field, generated by an electromag-

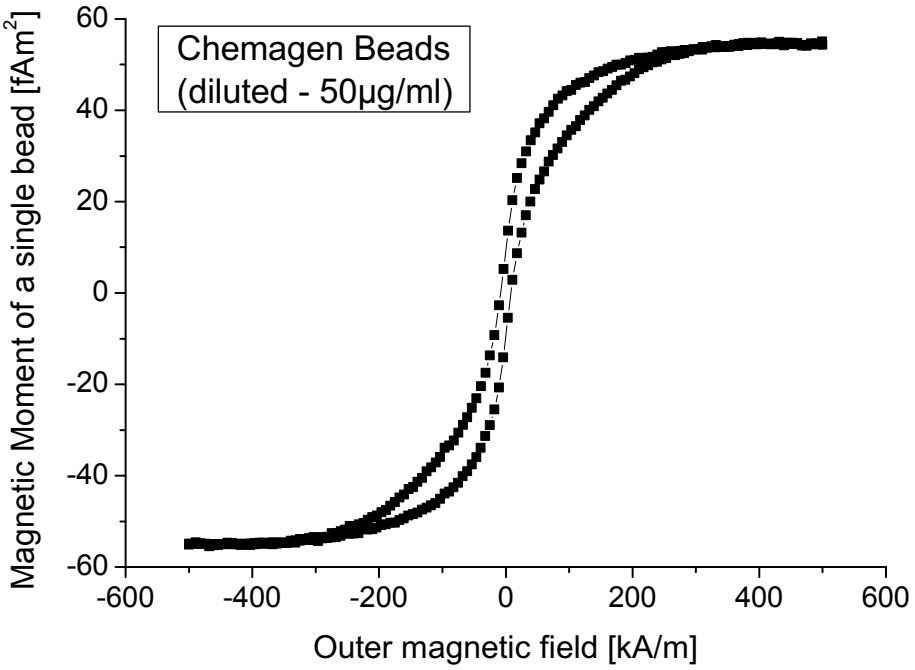

Figure 2.4: Example for an AGM measurement of magnetic markers.

net, is 14 kOe at an air gap of 12 mm. The sensitivity goes down to 10 pAm^2 with an accuracy of 2 %.

Although the AGM is very sensitive, single magnetic markers cannot be measured directly. Instead, several millions of markers are measured in the AGM and the average magnetic moment for a single bead can be calculated then. Additionally, the number of the measured magnetic markers cannot be counted exactly, but only estimated by the given dilution. Figure 2.4 shows exemplarily the calculated magnetic moment per bead for CHEMAGEN beads with a concentration of 50 μg/ml. For the bond-force measurements, the magnetic moment at a small outer field ($\approx$100 Oe) is interesting and not the moment for saturated magnetic beads.

Beside the fact that only the mean magnetic moment of the beads is known, more issues were found during the measurements. Although the beads are superparamagnetic, some of them show a remanent magnetisation. The reasons can be the clustering of the beads, not fully oxidised Magnetite (Fe_3O_4) particles inside the beads or a few very big beads. To

avoid clustering, the magnetic markers are pipette spotted onto a heated Si-wafer (≈100 ℃). Because the effect remained, the clustering cannot be the only reason for the ferromagnetic behaviour. Additionally, the magnetic moment shows a dependency on the concentration of the beads that cannot be neglected (6 different concentrations are tested for every bead type). All of this has to be taken into account, to calculate the magnetic moment at a small outer magnetic field.

2.7 Optical microscope with a CCD-Camera system

This section describes the main setup that was built for particle positioning and manipulation measurements. As shown in figure 2.5, the setup consists of an optical microscope with an attached CCD-camera and an IC-socket that holds the sample. A computer is used to record the applied currents/voltages and the video images of the sample (see figure 2.5(b) for a close-up of the setup).

The microscope is an Axiotech Vario from Zeiss with 3 Epiplan objectives, with a magnification of 20×, 50× and 100× and a 10× eyepiece. The sample holder is a self-made IC-socket, which is set on top of a micro precision positioning table from Parker. All contacts of the IC-socket are connected via a special box to the measuring instruments, power supplies and an analog-digital converter card (CIO-DAS08-PGA) in the computer. Using a c-mount adapter, the CCD-camera M4+ CL from JAI on top of the microscope is directly connected to a special video grabber card in the computer.

For a complete survey of the sample during the experiments, a computer program is developed that grabs images from the CCD-Camera, simultaneously measures voltages from the A-D card and saves the data together on the hard-disk. Because the magnetic field directly depends on the current through a conducting line, the voltage over a specified resistor is measured and directly converted into the current. For an easier review process and for better presentation of the collected data, another program was developed that takes the specified part of the images, adds the actual current/voltage inside the image and puts the single images together to a video. See the enclosed CD for the source code of both programs and examples of the videos.

(a) Overview

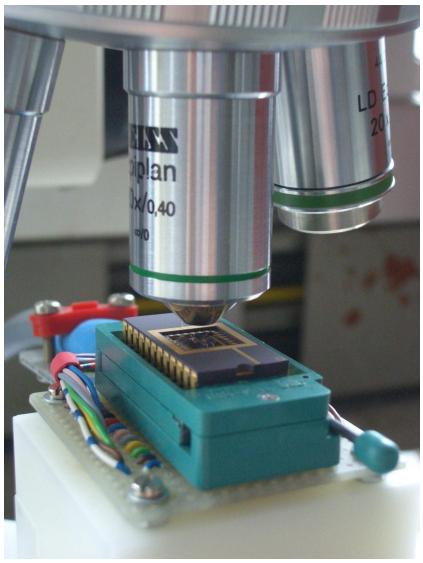

(b) Close-up

Figure 2.5: Setup used for the main measurements. Including an optical microscope with a CCD-camera, an IC-socket for the samples and a computer with proprietary developed software.

Chapter 3

On-chip manipulation of magnetic markers with conducting lines

The starting point for this thesis was the idea to use magnetic markers for the manipulation of biomolecules directly on-chip. The magnetic fields that are needed for the manipulation can be created by currents through conducting lines on a Si-wafer. Together with magnetoresistive sensors, everything that is needed for a magnetic biosensor can be integrated into a small chip using standard methods of micro-electronics. Besides several advantages, such as low cost and portability, this setup opens up many possibilities for new measurements in the micro and nano cosmos.

This chapter provides all information about the basic setup of all samples and discusses several problems that have to be considered. Besides the first simple approach, several examples for manipulations on a chip will be presented and discussed.

3.1 Basic sample preparation

All samples in this thesis, which are used for manipulation or positioning of magnetic markers, have the same basic preparation procedure. Figure 3.1 presents the five main steps in the procedure. The first step is the optical lithography (a) that consist of spin-coating the sample with a resist, exposing it with a laser lithographer, and developing the resist to get the written design (check section 2.3 for a comprehensive description of optical lithography). Then, the whole sample is etched with Ar^+-ions, so 200 nm deep holes are created where the resist was removed (b) (see section 2.2 for a description of

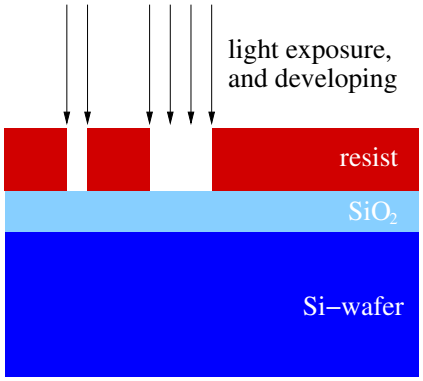

(a) Optical lithography

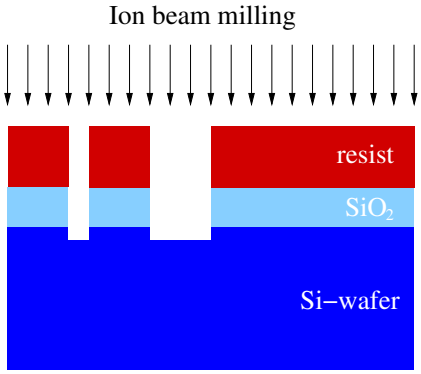

(b) Etching holes in the wafer

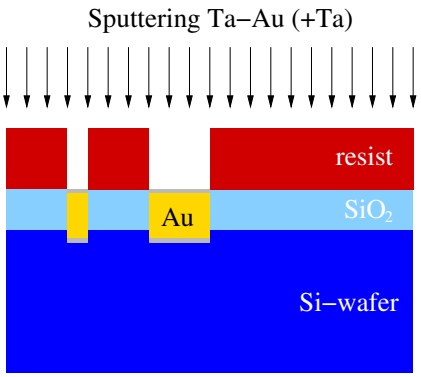

(c) Filling up the holes

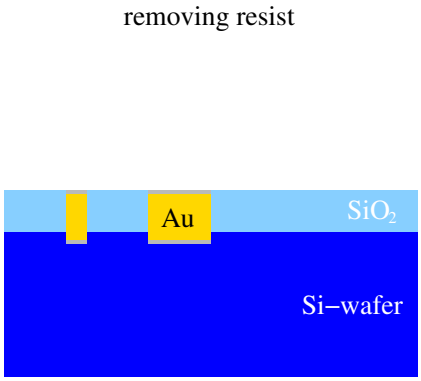

(d) Removing the resist

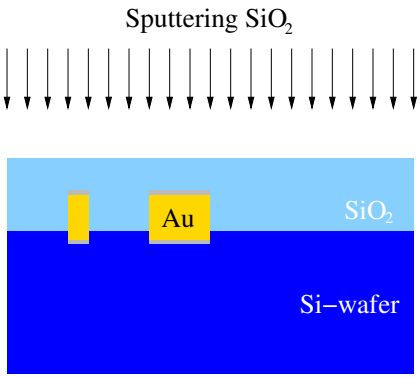

(e) Optional sputtering of a protection layer

Figure 3.1: Side view of a sample for all preparation steps

the etching process). These holes are exactly filled up with Au (c), using 5 nm thick Ta below and on top as an adhesive agent (thin grey layers). Finally, the resist is removed (d), and optionally, a protection layer of 100 nm SiO_2 is sputtered onto the sample (e).

Initially, the conducting lines were not embedded into the Si-wafer, but first experiments showed that the protruding lines are real obstacles for the magnetic particles. This is no real surprise, as the height of the conducting lines is nearly one third of the diameter of a bead. Because the conductivity of gold is much higher than the conductivity of silicon, it is no problem to embed the gold lines into the Si-wafer (confer figure 3.1c).

The SiO_2 protection layer is not added for all experiments, as it is only imperative for the bond-force measurements. But this layer helped in several experiments and was used in many cases.

The thickness of the conducting line and the width at the narrowest point determines the resistance and the maximum possible current. In most samples the resistance of a conducting line is between 20 and 300 Ω and the maximal possible current is about 30 to 150 mA.

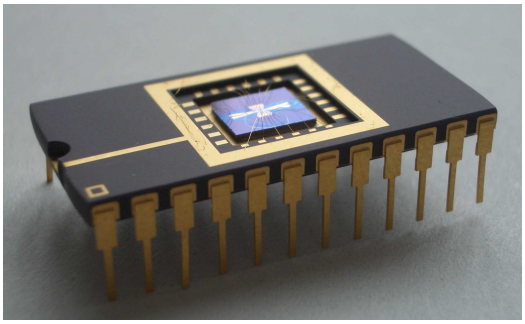

Figure 3.2: Sample inside the IC-Socket. Bonded gold wires connect the design with the socket pins

For most measurements, the sample is glued with conductive silver paste to an IC-socket. For an easy connection, the contact pads of the structure are then wire bonded to the IC-socket. Figure 3.2 shows a complete sample in the IC-socket.

3.2 Problems during the measurements

Even for the first simple measurements, there were several problems that occurred during the measurements. Some were expected, others not.

One major problem is electromigration [25] that is generally the result of momentum transfer from electrons, which move in an applied electrical field to the lattice of the conducting material [4]. Thus, the electromigration occurs when many electrons massively scatter inside the conducting material. This massive scattering moves material and thereby deteriorates the conductivity of the material. The predominant failure mechanism for conducting lines is the growing of voids over the entire line. Very small imperfections al-

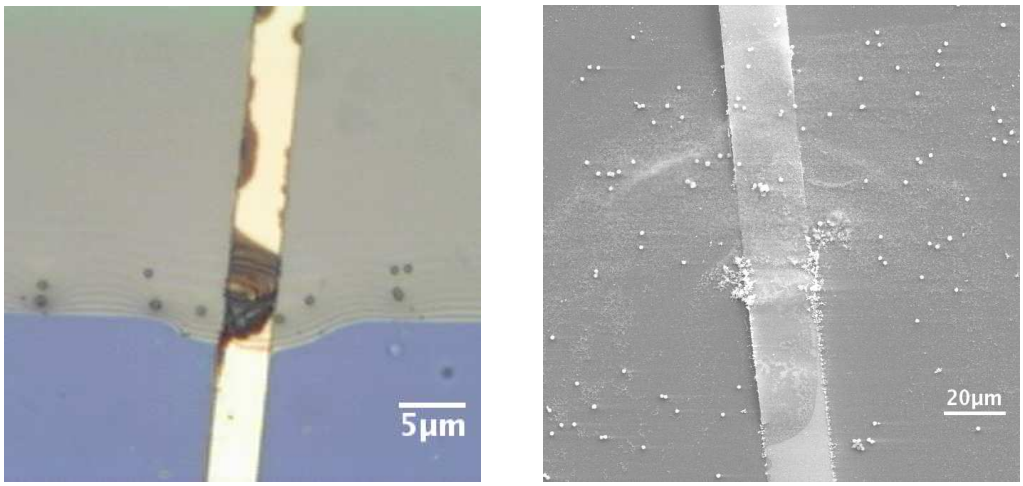

(a) Optical image (b) SEM image

Figure 3.3: Examples for the electromigration of a conducting line

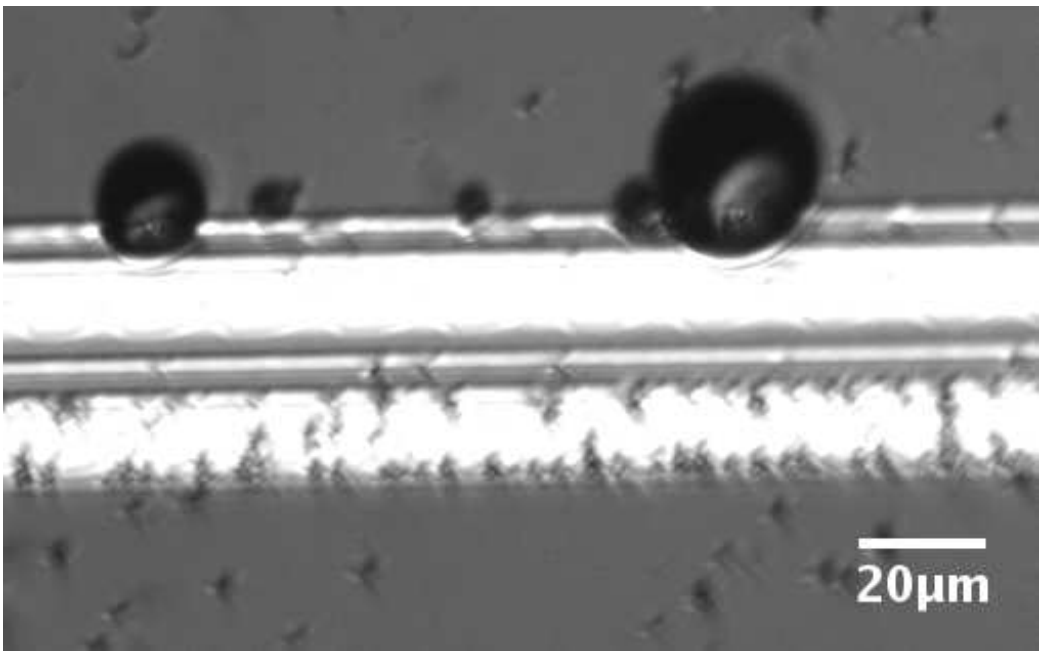

Figure 3.4: Water is boiling because of an overheating conducting line

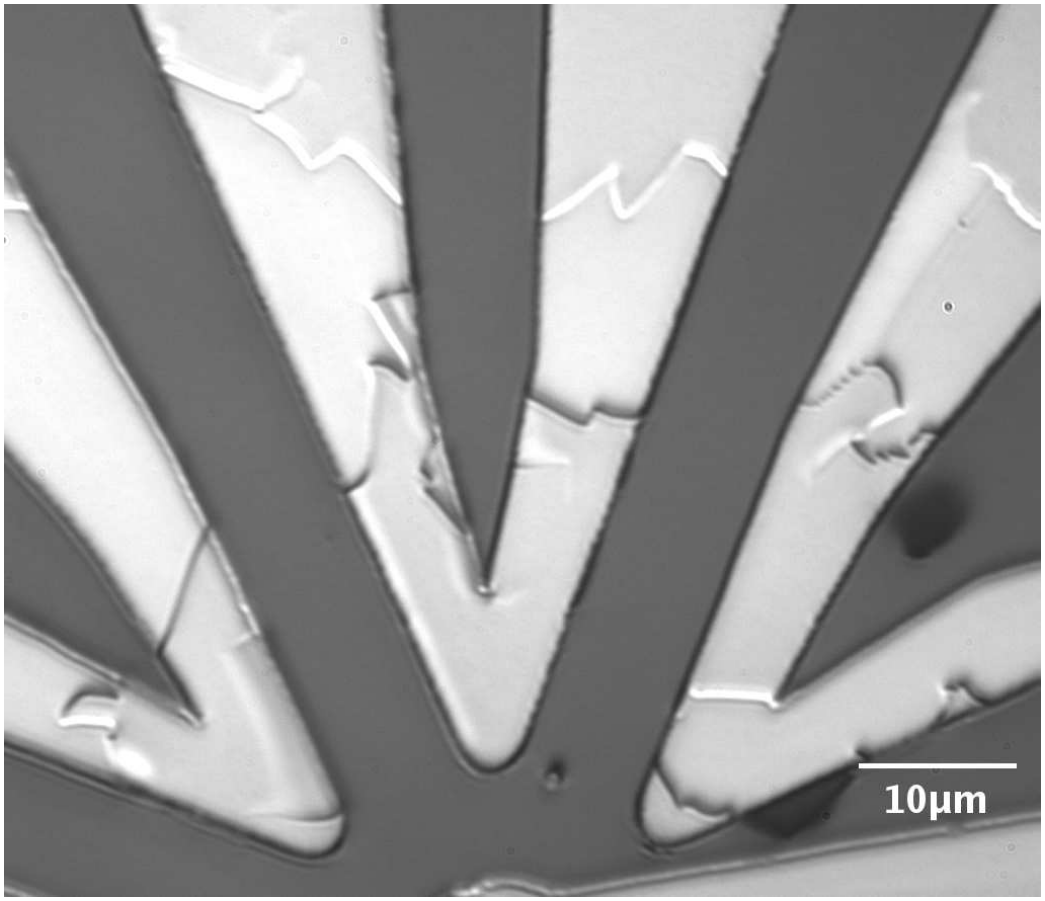

Figure 3.5: Splintered glass on top of the conducting lines

ready amplify the scattering, and are often nucleation centers for the growth of large voids.

Figure 3.3 shows examples for disconnected conducting lines due to electromigration. In the image of the optical microscope (a), you can see clearly the part where the gold of the conducting line turned black and the electromigration has destroyed the line. The change of the material properties can also be seen in the SEM image (b).

A related problem often occurs before the electromigration. The conducting line is overheating, and with it, local boiling inside the water drop occurs. Initiated again by imperfections inside the conducting line, some points become very hot, and the water above these points starts boiling. As shown in figure 3.4, these hot spots trigger bubbles inside the water drop. It is observed that the bubbles nearly always occurred at the edges of the

conducting line. This is an indication for the fact that there are more imperfections at the edges of the conducting lines due to nooks and ridges from the lithography.

Besides the problem that all magnetic particles are strongly pushed away by the rising bubbles, the bubbles can also destroy the SiO_2 protection layer and, therefore, destroy the sample. Figure 3.5 shows an optical image of a sample surface after those bubbles rose from the conducting lines. The protection layer is clearly destroyed, although no electromigration occurred.

For measurements with two or more conducting lines, it is important that there is no current flow between the lines. Because, if the current flows through the protection layer and the water drop you have unwanted electrolysis on the sample, and such a current often initiates overheating and electromigration. The resistance over the water drop or the Si-wafer between the lines is not very high ($\approx 50\,\mathrm{kOhm}$), so that a current can easily flow when the potential is switched from one to another line. Therefore, the potential has to be zero, when the power source is switched on to another conducting line.

3.3 Examples for on-chip manipulation with magnetic markers

Keeping all these precautions in mind, magnetic markers can be manipulated with conducting lines in many different ways. This section presents several possibilities to manipulate markers that were tested during this thesis, and compares the results with similar experiments of other research groups.

3.3.1 Current through a straight line (proof of principle)

As a starting point, the principle of this manipulation technique is tested with the simplest setup. A single straight conducting line with two contact pads at both ends is patterned with optical lithography. Above the conducting line, a drop of water with magnetic markers is placed. A current through the line creates a magnetic gradient field, that magnetises the superparamagnetic markers, aligns them to the magnetic field and pulls the markers to the conducting line. Figure 3.6 shows 5 selected images of the video of this simple experiment.

A constant current of 5 mA is already enough to attract a magnetic marker that is about 33 μm away. Without the magnetic field, the marker just follows

(a) 0 sec (b) 10 sec (c) 20 sec

(d) 30 sec (e) 33 sec

Figure 3.6: A 5 mA current through the straight conducting line (width = 3.8 μm) attracts the magnetic marker. The images have a size of 63 μm × 37.8 μm. See the CD for the complete Video.

the brownian motion [78], but with the magnetic gradient field it slowly moves towards the conducting line. The marker accelerates towards the conducting line until it reaches the local field maxima on top of the line. Before it reaches the conducting line, the maximum velocity of the bead is about 6 μm/sec.

In order to describe the forces that act on the magnetic marker, the friction of the marker in the fluid (STOKES' law) has to be subtracted from the magnetic force (see equation 1.10 on page 22):

$$\vec{F} = \vec{F}_{\text{mag}} - \vec{F}_{\text{friction}} = \frac{m \cdot \mu_0 I}{2\pi R^2} - 6\pi r \eta \vec{v} \tag{3.1}$$

Here we assume a spherically shaped marker with radius r, a viscosity η of the water drop and an actual velocity $\vec{v}$ of the marker. Using equation 3.1, the maximum possible velocity can be calculated, when $\vec{F}_{\text{mag}} = \vec{F}_{\text{friction}}$. With a maximum current of $I = 150\,\text{mA}$, a magnetic moment of $m = 1.82\,\text{fAm}^2$ of the particle (see table 1.1), a distance $R = 2\,\mu$m, a radius of the marker $r = 1\,\mu$m and a viscosity for water of $\eta = 1\,\text{mPa sec}$ at room temperature, the maximum possible velocity is:

$$\vec{v} = \frac{m \cdot \mu_0 I}{12\pi^2 r \eta R^2} = 7 \cdot 10^{-4} \frac{\text{m}}{\text{sec}} \tag{3.2}$$

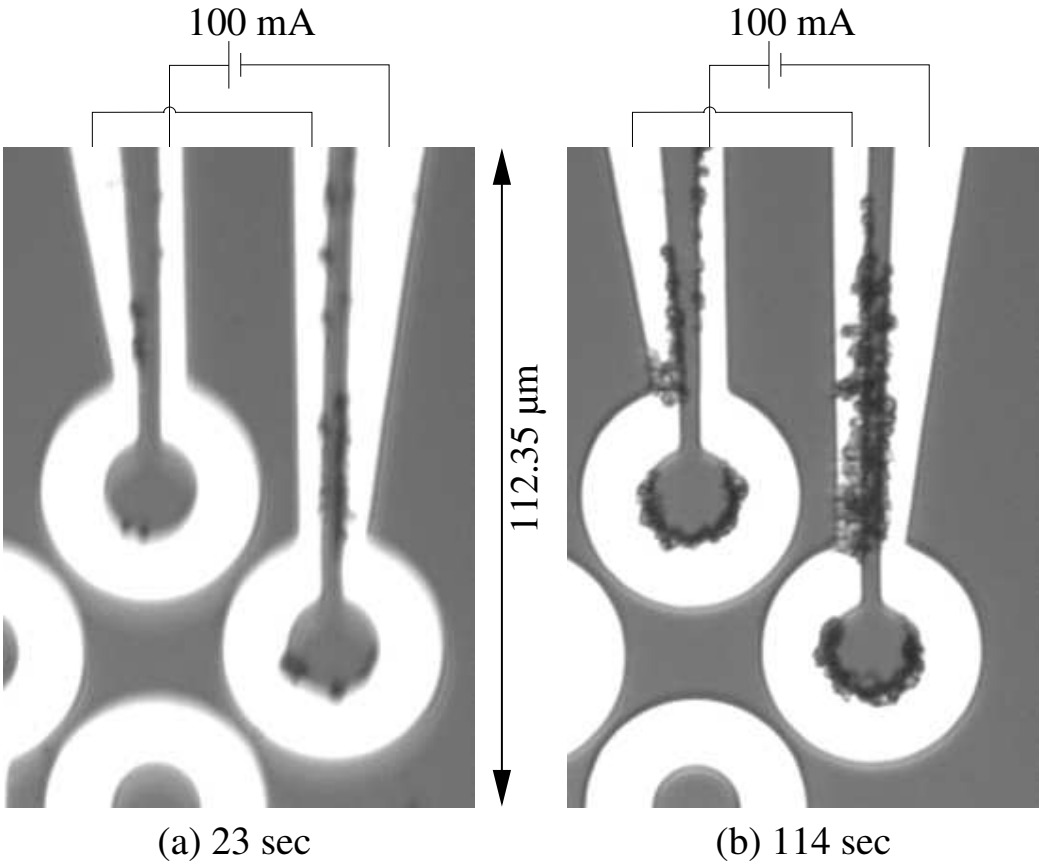

Figure 3.7: Trapping magnetic markers inside a ring shaped conducting line. See the CD for the complete video.

This initial experiment proves that in principle the manipulation works well. Several more examples for particle manipulation are following.

3.3.2 Trapping markers in a ring

Figure 3.7 presents an approach to trap several magnetic markers inside a ring shaped structure. The ring has an outer diameter of 37.1 μm and an inner diameter of 14.9 μm, so the conducting line is 11.1 μm wide. A potential is applied to both top rings with a current of 100 mA. Two images of the video are presented here, after 23 secs (a) and 114 secs (b).

Attracted by the magnetic field of the conducting rings, the magnetic markers follow the gradient to the nearest local maximum. From figure 3.7(a), it is clear that there are three local maxima. Two maxima are at both inner

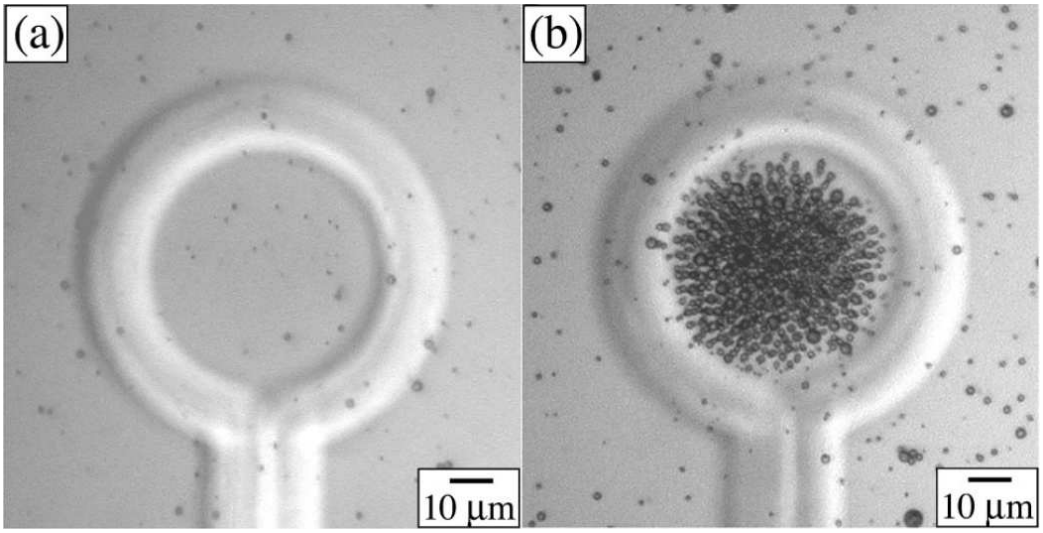

Figure 3.8: Trapping many magnetic markers inside a ring shaped conducting line, from [85]

sides of the two supply lines above the ring, and the third is at the bottom of the inner side of the ring. After 114 secs, a lot more beads are attracted and populate the conducting rings (b). The beads at the two maxima between the supply lines build up one big crowd, and inside the ring structure, the beads align to the local maximum at the lower edge of the inner ring.

As expected from EARNSHAWS theorem (confer page 22) the beads do not cumulate in the center of the ring, but at the inner edge. This is also true for the inner side of the supply lines. The local maxima are directly at the edges, and not in the middle between the supply lines.

LEE *et al.* made a similar experiment in 2001 [85]. They structured a ring shaped trap for magnetic particles using the electro-plating technique (see figure 3.8). Although they used similar magnetic markers (BANGS LABORATORIES, diameter 1-2 μm), the ring structure is much bigger and, due to the electro-plating technique, the ring is much higher (the height is not given exactly, but probably about 3 μm). Applying a high current of 350 mA, they cumulated hundreds or thousands of particles inside the ring structure. Figure 3.8(b) does not show the expected maxima at the edges, but a nearly uniform distribution inside the ring. There are several possible explanations for this differing result. First of all, the ring structure elevates several micrometer above the surface, and therefore, the ring is a high wall for the particles inside the ring. When the current is turned off, the particles move away from the wall to the middle of the ring. The elevated structure is also the reason

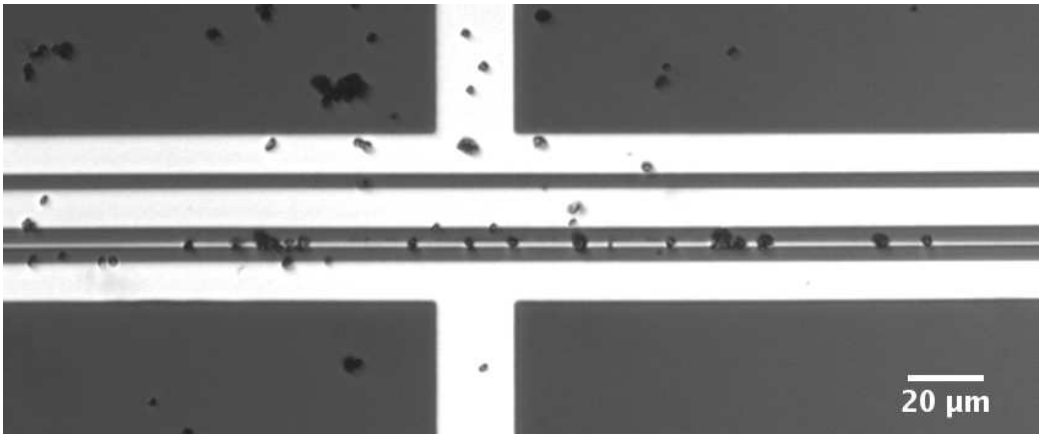

Figure 3.9: Manipulation with magnetic and electric fields. A current through the thin and wide lines in the middle generates a magnetic field, and the top and bottom lines are electrodes of a capacitor to create an electric field. See the CD for a complete video.

why there are no particles between the supply lines. Another possible explanation is that there are so many particles inside the ring that they show clustering effects. The results can not really be explained without seeing the complete process in a video (unfortunately the video is not available). Because we are more interested in manipulating very few or only single particles, this example is not investigated further, and other approaches were tried.

3.3.3 Manipulation using electric fields

Nearly all materials can be manipulated with electric fields. If a material is charged, it can easily be moved in an electric gradient field (the direction depends on the charge). If a material is not charged, the electric field induces a dipole moment within in the material and the induced dipole moment is then affected by the electric field (e.g. this is used in dielectrophoresis experiments, see below). In the experiments presented in this chapter the magnetic beads are also charged, and so they can easily be manipulated.

Figure 3.9 shows a setup that uses magnetic and electric fields to manipulate magnetic markers. Currents through the two lines in the middle (wide and thin line) create magnetic fields, and the top and bottom lines are electrodes of a capacitor creating an electric field between them.

In the experiments, the magnetic markers are collected with a small current on the lines in the middle (see the CD for the complete video). Then,

the current is turned off and an electric field is applied on the outer electrodes. The movement of the beads is viewed and recorded through the optical microscope, as before.

When the electric field is turned on, many markers are drawn quickly towards one of the electrodes. Only very few don't move at all. Although this observation shows that the markers can be manipulated with electric fields, it also reveals the major problem of this method. The experiment shows that the markers are charged and, therefore, attracted or rejected in the electric field. This is quite similar to the oil-drop experiment of MILLIKAN[1] in 1907 [94]. But here it is unclear how much the markers are charged and if they are positively or negatively charged. The video shows all three possibilities (positively charged, negatively charged and uncharged) in the same sample. Therefore, this method is not usable for a controlled manipulation of magnetic markers. However, the electric force exerted on many markers seems to be much stronger than the force that can be applied with the magnetic field. Therefore, we will briefly refer to this method in chapter 4.1.

Another approach to manipulate markers with electric fields, that is not used in this thesis, is to use ac fields that exert a dielectrophoretic force on the markers. Dielectrophoresis describes the movement of particles caused by the interaction of the induced dipole moment and an external electric field [34]. The dielectrophoretic force depends on the frequency of the external ac electric field and on the magnitude of the complex dielectric constant of the particle in relation to that of the used medium. This method is especially interesting, because just by changing the frequency, you can change from an attractive force to a repulsive force. But using electric fields also has the disadvantage that everything on the sample is manipulated nonselectively. All kinds of particle traps can be built with this technique, and so there is a lot of research done about dielectrophoresis. Manipulation [81] and separation [96] of bio-particles or nanoparticles [74] are done with dielectrophoresis as well as the use of dielectrophoresis in diagnostic instruments [48]. Furthermore, microspheres were specially engineered for their dielectric properties [128]. The combination of magnetic on-chip manipulation techniques with on-chip dielectrophoresis is a promising field for future research.

[1] MILLIKAN got the nobel prize in 1923 for his work on the elementary charge of electricity (using the oil-drop method) and on the photoelectric effect.

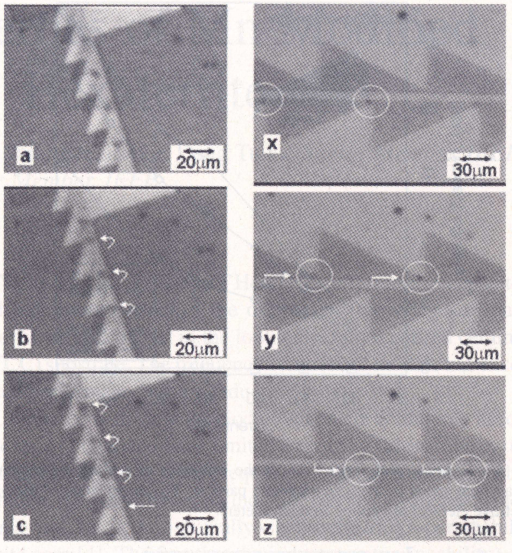

Figure 3.10: Transportation of single beads, from Wirix-Speetjens and De Boeck [136]

3.3.4 Transportation and positioning of magnetic markers

In 2004 Wirix-Speetjens and de Boeck presented [136] an interesting method to transport magnetic particles along a defined pathway using an alternating magnetic gradient field. In a quite simple setup with only two sawtooth shaped conducting lines, they guided single particles along a predefined line. They used 2 μm Micromod beads, and an alternating current of 50 mA at a frequency of 0.1 Hz in their experiments.

Figure 3.10 shows their results for a dual metallisation device (a,b,c) and for a single metallisation device (x,y,z). In the images, the white arrows indicate the stepwise movement of the single magnetic particles. The movement in one direction only works if the two conductors are very well aligned. Otherwise, the magnetic particle moves back and forth between two local maxima. The velocity of the magnetic particle can be adjusted by changing the current and by changing the proportion between the width and the length of the sawtooth structure.

Because this thesis combines magnetic manipulation and detection, a different structure is designed that allows the transportation of a bead to several defined positions. Figure 3.11 presents the star like structure and the positioning of a few beads at defined locations. Outside the optical microscope

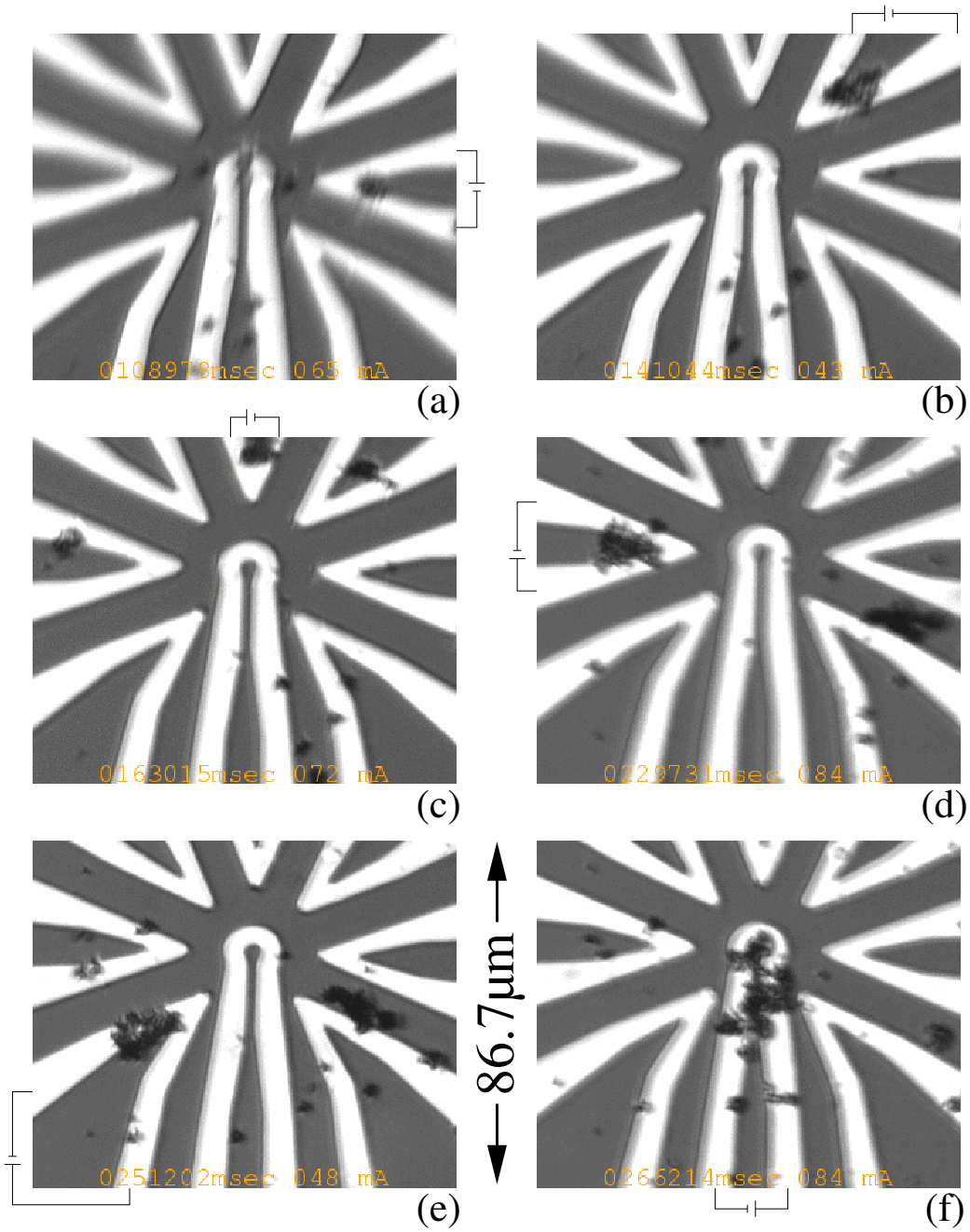

Figure 3.11: Moving magnetic particles to several defined positions with a star like structure.

images of figure 3.11(a-f), it is always sketched where the potential is applied. The time and the actual current during these six images of the video are written in orange at the bottom of the images. At the beginning a few magnetic beads are collected in the corner of the right conducting line (a). Then, the current is turned off in the right line and the top-right line is turned on (b). The beads directly move from the right to the top-right corner (see the attached CD for the complete video). In the same fashion the beads are moved counter-clockwise around until they are finally collected in the middle ring (f).

The accuracy of the positioning inside the corner only depends on the accuracy of the lithography. Using optical lithography, we are restricted by the wavelength of light. So in this experiment, the accuracy of the positioning can only be about 1 μm (about the size of the used magnetic beads). Changing to e-beam lithography would allow a much better positioning accuracy of about 50-100 nm.

During the experiment, that takes about 5 minutes, more and more beads are collected from the vicinity. Therefore, the number of beads in the corners increase steadily. While in the first corner, there were only about 5 beads, in the end there are probably more than 30 beads. Although it isn't tested, this experiment can certainly be done with single beads. As will be shown in chapter 5, this mainly depends on the concentration of the beads in the solvent.

What cannot be seen in the six images, but in the complete video, is a problem with the top-left conducting line. Immediately after this line is turned on, bubbles rise from the surface and turn the microscope image completely black (that's the reason for not providing the image here). For a discussion of this bubble problem, see section 3.2. Although the top-left conducting line is not working, the experiment can go on. So the principle of this transportation and positioning technique for magnetic particles works very well.

3.4 Discussion

Starting with a proof of principle experiment, it is shown that the on-chip manipulation and transportation of magnetic particles works as well as the positioning of the particles in specific predefined places. Despite a few problems during the experiments and the preparation, all kinds of manipulations can be achieved with conducting lines on a chip. For nearly all transportation and positioning tasks, a specially designed structure can easily be prepared. It is shown that a small current ($\approx$5 mA) is enough to manipulate the mag-

netic particles, and that the manipulation of a single particle is possible. The accuracy of positioning magnetic beads only depends on the accuracy of the lithography method.

The behaviour of a single particle in a hydrodynamic system was simulated by Jan Stallkamp in 2003 [118]. The recent method of Lattice-Boltzmann-simulations enables deeper insight into the behaviour of colloidal systems, and is especially interesting for particles with attached biomolecules.

After this general approach to the on-chip manipulation and positioning, two special applications will be presented. In chapter 4, a manipulation method will be used to measure the bond-forces between two biomolecules. And finally, a single bead will be exactly positioned on top of a TMR-Sensor in chapter 6.

Chapter 4

Bond-Force measurements

This chapter presents a new technique to measure the bond-force between two biomolecules. The manipulation method presented in chapter 3, together with a special customised design, is used to pull at a bond between two biomolecules until it breaks. One biomolecule is attached to the magnetic bead and the other is connected to the sample surface.

The setup for these experiments is shown in figure 4.1. Two conducting lines (a wide and a narrow one) are structured and covered by SiO_2 (see section 3.1 for a comprehensive explanation). The sample surface is then covered in a special process (see section 4.3) by one kind of biomolecules (red in figure 4.1). Commercially available magnetic markers that are covered with a matching biomolecule (green in figure 4.1) are put in solution on the sample surface. The beads are collected on top of the thin conducting line with a small current, so that the biomolecules at the markers can bind to the biomolecules on the surface. After a few minutes, the small current is turned off and a current through the wide conducting line is turned on. This current, and with it the magnetic force on the marker, is increased very slowly, while the beads on the sample are recorded by a CCD-camera (confer section 2.7 for the complete description of this setup). All beads that did not bind to the surface are directly drawn off the thin conducting line. The other beads stay until the applied force $\vec{F}_{\text{bond}}$ is so high that the bond between the biomolecules breaks. Because the current and all other needed variables (confer equation 1.10) during the rupture events are

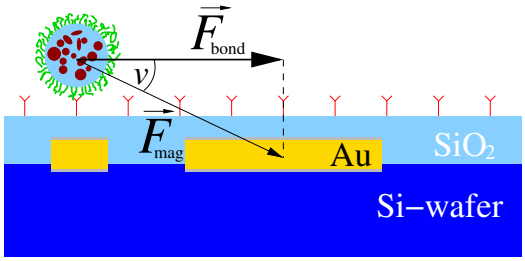

Figure 4.1: Sketch for the bond-force measurements

known, the magnetic force $\vec{F}_{\mathrm{mag}}$ can be calculated [1]. And because the angle $\nu \leq 5^{\circ}$ in our experiments (confer figure 4.1), we can state with an error of less than 1 % that $F_{\mathrm{bond}} \approx F_{\mathrm{mag}}$. Hence, the rupture force between the magnetic marker and the surface can be calculated directly.

4.1 Sulfur-gold bond

The sulfur-gold bond has several advantages and was, therefore, the first bond tested in this thesis. One advantage is that it is a strong covalent bond with a high bond enthalpy of $418 \pm 25\,\mathrm{kJ/mol}$ [135]. Because nearly all bonds between biomolecules are weaker, this would be a good proof of principle for the method. Furthermore, this bond is well known, e.g. Grandbois *et al.* presented AFM experiments in 1999 [54] where they measured a bond-force of $1.4 \pm 0.3\,\mathrm{nN}$ at loading-rates of $10\,\mathrm{nN/sec}$ for the sulfur-gold bond.

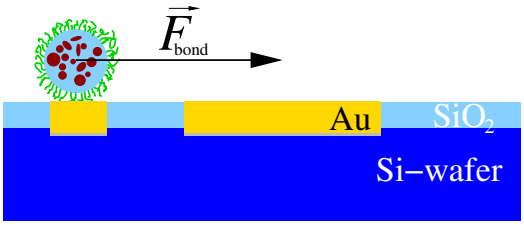

Figure 4.2: Sketch for the Sulfur-gold bond measurements

Another key advantage is the simplified setup shown in figure 4.2. Magnetic markers functionalised with a SH-group on the surface can directly bind to the patterned gold lines. The fabrication of the sample is much easier, because there is no surface preparation involved and even the SiO_2 protection layer is omitted. Suitable magnetic markers are commercially available in a wide variety. The Sicastar-SH particles from Micromod (with a diameter of $1.5\,\mu\mathrm{m}$) were used because these particles passed some important tests.

The most important property is that the markers only bind specifically to gold and not on the SiO_2 surface of the wafer. To ensure this, we tested the Sicastar-SH markers on SiO_2 surface and Micromod Sicastar markers without a SH-group on a gold surface. In both tests, the markers did not bind to the surface.

During the experiments, it became apparent that the binding only works good when the sample was freshly made. Even an ultrasonic bath in acetone didn't change this behaviour. This was very much unexpected, because the gold lines, buried in SiO_2, should not change over time, and the magnetic markers are always the same. So, we examined whether the gold surface changes over time. Auger measurements of a freshly made gold surface and

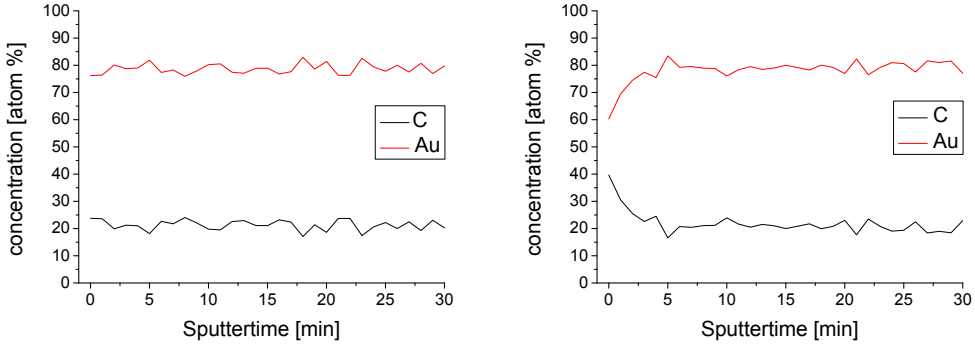

(a) Only 5 minutes on air

(b) 6 weeks on air

Figure 4.3: Auger measurements of sputtered gold surfaces

of a 6 weeks old gold surface are compared in figure 4.3. The Auger measurements clearly show that with time, carbon is deposited on top of the gold surface. So, the fact that the markers do not bind well to an older surface supports our main concern that we only examine the sulfur-gold bond and no unspecific binding. Therefore, we had to prepare fresh samples or expose the sample for 30 sec to ion beam milling (see section 2.2).

Results and Discussion

In all our experiments with magnetic gradient fields, the sulfur-gold bond could not be broken. The markers either did not bind at all, or could not be ripped off the gold line, even with currents of up to 150 mA. The maximal force with a current of 150 mA, a magnetic moment of the beads of 0.4 fAm^2 and at a distance of 9.63 μm, can be calculated as 129 fN. This is 4 magnitudes lower than observed in AFM measurements [54] and obviously too weak. But it may not be that far away, when thinking about the loading-rate dependency found for other bonds (confer section 1.1.4).

Although the sulfur-gold bond could not be broken with an applied magnetic gradient field, it can be broken with an electric field. Using the setup, already presented in section 3.3.3, the rupture of the sulfur-gold bond works in principle. Figure 4.4 shows three images from the video of the rupture

[1] STOKES law does not apply for these experiments, because the particle does not move until the bond is ruptured. So the velocity $\vec{v} = 0$ and therefore the friction $\vec{F}_{\text{friction}} = 0$.

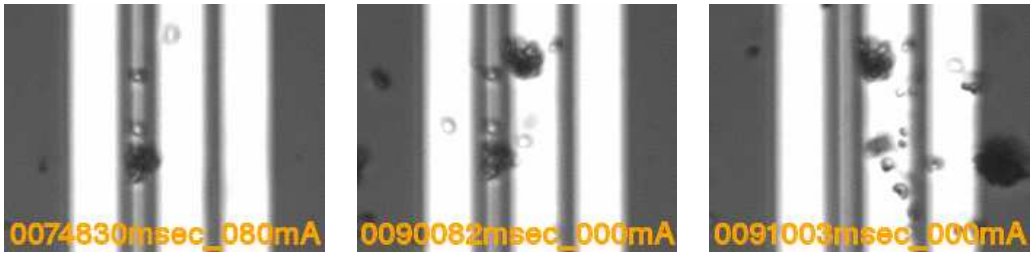

(a) Applying a current of 80 mA through the wide line in the middle

(b) Directly before the electric field is turned on

(c) Directly after the electric field is turned on

Figure 4.4: The sulfur bond cannot be broken with the maximum magnetic field (a), but with an electric field between the outer electrodes, (b) and (c). See the CD for the complete Video.

events. In the first image the two single beads on the thin line and the bead agglutination below still bind to the gold surface (a), so the magnetic force at the maximal possible current of 80 mA is still too weak. But when the electric field is turned on, all beads are ruptured. See before (b) and after (c) the electric field is turned on. However, the uncertainty of the charge carried by each bead (confer section 3.3.3) prohibit a calculation of the bond-force.

Because this very strong covalent bond could not be broken with the magnetic gradient field, non-covalent but still strong ligand-receptor bonds were used for the next experiments. The following sections present measurements of the streptavidin-biotin and the avidin-biotin bonds.

4.2 Sample preparation for ligand-receptor bonds

For all following bond-force measurements, the samples are initially prepared as shown in figure 3.1(a-e). Figure 4.5 presents the design that is used for the optical lithography in step (a). There are two thin ($\approx 2\,\mu$m wide) and two wide lines ($\approx 12\,\mu$m) which are always connected by a contact pad at both ends. The outer part of the design, where the conducting lines broaden, was done to avoid problems during the laser lithography. Very thin and long lines were often disconnected or joined with neighbouring lines. This design, with very few corners and broadened lines minimised such problems.

First, the markers will be collected on the thin lines, before a high current

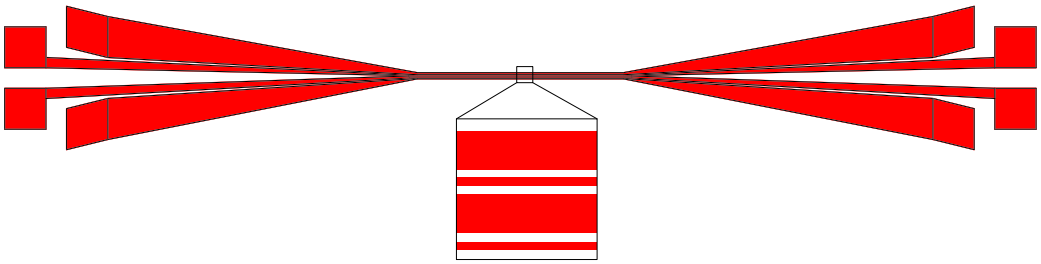

Figure 4.5: Complete design used for all bond-force measurements. The measurement area is magnified.

through the wide line tries to rupture the examined bond between marker and surface. The SiO_2 protection layer in step (e) is imperative for the subsequent biological surface preparation (see section 4.3). Typically, the design of figure 4.5 is structured three times in a row on one piece of Si-wafer. This wafer piece is then glued with conducting silver paste to an IC-socket, and the structure is connected to the socket by wire bonding.

4.3 Surface preparation for the bond-force measurements

For the bond-force measurements of the ligand-receptor bonds, the surface of the samples need a special preparation. This was done by Paul-Bertram Kamp within a collaboration of the Sonderforschungsbereich 613 (Project K3). The surface preparation was always done after the following recipe:

Before any biological preparation of the surface, the sample is heated at 120 °C for 5 min to dry it. The surface is then silanized with an epoxy-silane by heating the sample for two hours at 80 °C in a solution of 2.5 % 3-Glycidyloxy-propyl-trimethoxysilane in xylol and 0.1 % triethylamin (all chemicals from Sigma-Aldrich, Taufkirchen, Germany). The silanisation is followed by 3 washing steps with acetone and finished by drying the sample at 100 °C for five minutes. On top of the silanized surface, 0.3 μl biotinylated oligonucleotides (biotin-5'-agggttttcccagtcacgacgtt-3', Sigma-ARK, Germany), diluted 1:1 with 58 % DMSO, 40 % Methanol and 2 % TEMED, are pipette-spotted. Directly after spotting, the samples are stored in a damp atmosphere for 1 hour. Then, the samples are heated for five minutes at 100 °C and exposed to 300 mJ UV light. Three washing steps follow with a washing buffer of 50 mM Na_2HPO_4, 10 mM Tris-Base, 5 mM EDTA, 0,1 % SDS, 0.01 % N-laurosyl sarcosine, 0.01 % Tween 20, 0.01 % Triton X100,

0.1 M NaCl and 0.5 % polyethylene glycol 4000 at a pH of 8.5 (adjusted with acetic acid) and another washing step with distilled water. To deactivate the excessive epoxide groups, the sample is incubated for 1 hour at 55 °C in 1 M sodium acetate buffer containing 2.5 % polyethylene glycol 4000 with a pH of 5.0. Finally, the samples are washed three times in washing buffer (see above) and one time in distilled water for five minutes. The samples are stored at room temperature until usage.

The concentration of the biotinylated oligonucleotides is a critical parameter for the experiments, since a too high concentration result in several bonds per bead and with a too low concentration, there are nearly no bonds at all. Both cases have to be avoided and, therefore, different concentrations were tested and also adjusted to the used beads (different beads have different binding properties). The final concentrations of oligonucleotide used in these experiments are between 10 and 1000 nM.

4.4 Selection of suitable magnetic markers

For all bond-force measurements, it is absolutely necessary that there is no unspecific binding between the magnetic markers and the sample surface. Therefore, all markers were tested and carefully selected.

First, all 12 different magnetic markers we had at our disposal were tested for unspecific binding to the SiO_2 surface of the wafers. To test this, a drop of water containing many beads were pipette-spotted on to the wafer. After waiting for a few minutes, the wafer is washed in distilled water and blow dried with nitrogen. Then, the wafer is examined for magnetic beads that still adhere to the wafer. Only the types of beads that did not adhere to the wafer were used for a second test.

For the ultimate test, samples were prepared as described above with only one alteration. The pipette-spotting of the biotinylated oligonucleotides was omitted during the surface preparation. Because of the missing biotin, the beads cannot bind specifically to the surface. Therefore any binding event would be an unspecific bond, which is not allowed. It was tested several times with all beads used for the bond-force measurements that they never bind unspecific to the sample surface.

The three types of beads that are used, because they meet these requirements, were already presented in section 1.2.

4.5 Bond enthalpy of all involved bonds

When the magnetic force is applied to the magnetic marker, the force is applied to all bonds between the surface and the marker. Because the weakest bond will break first, only this bond can be examined in these experiments. Because we want to examine the ligand-receptor bonds, we have to make sure that these bonds (streptavidin-biotin or avidin-biotin) are the weakest.

Figure 4.6 shows all involved bonds and their corresponding bond enthalpy. Except for the ligand-receptor bonds, all bonds are covalent bonds with a bond enthalpy of several hundred kJ/mol. The weakest covalent bond is O-N with a bond enthalpy of 181 kJ/mol. But the non-covalent ligand-receptor bonds we want to examine are clearly weaker. For full binding capacity (i.e. all four binding sites occupied), streptavidin-biotin has a bond enthalpy of 96.2 kJ/mol and avidin-biotin of 85 kJ/mol [55]. Therefore, it is clear that only the ligand-receptor bonds will be ruptured in the experiments and nothing else.

4.6 Results

All bond-force measurements are viewed with an optical microscope and recorded with a CCD-camera system (see section 2.7 for more information about the setup). Figure 4.7 shows three images of such a video where two rupture events are recorded. The current is slowly increased during the measurement and two beads still bind to the biotinylated surface at a current of 73 mA (a). One second later, at a current of 74 mA, the upper marker is gone, so the bond was ruptured (b). Several seconds later, at a current of 81 mA the bond of the second marker was ruptured (c).

The recorded videos of all measurements were evaluated for such rupture events (see CD for videos of all rupture events). In order to calculate the bond-force F_{mag} with equation 1.10, we need three variables. We get the current I and the distance R directly from the recorded video, and together with the magnetic moment m of the markers (see table 1.1 on page 18), the magnetic force for every rupture event is calculated.

Figure 4.8 presents the results of all bond-force measurements with Chemagen beads (a) and Micromod beads (b). The measured bond-forces for the streptavidin-biotin bond (a) are very low (in the range of 25-475 fN), and the distribution clearly shows two maxima. The average of the first maximum is at a bond-force of 55.9 fN ($\sigma_{\bar{x}} = 18,9$ fN) and the average of the second maximum is at 244,7 fN ($\sigma_{\bar{x}} = 64,5$ fN). There is also a single event at 457 fN, which will be discussed later. The bond-forces of the avidin bonds are even

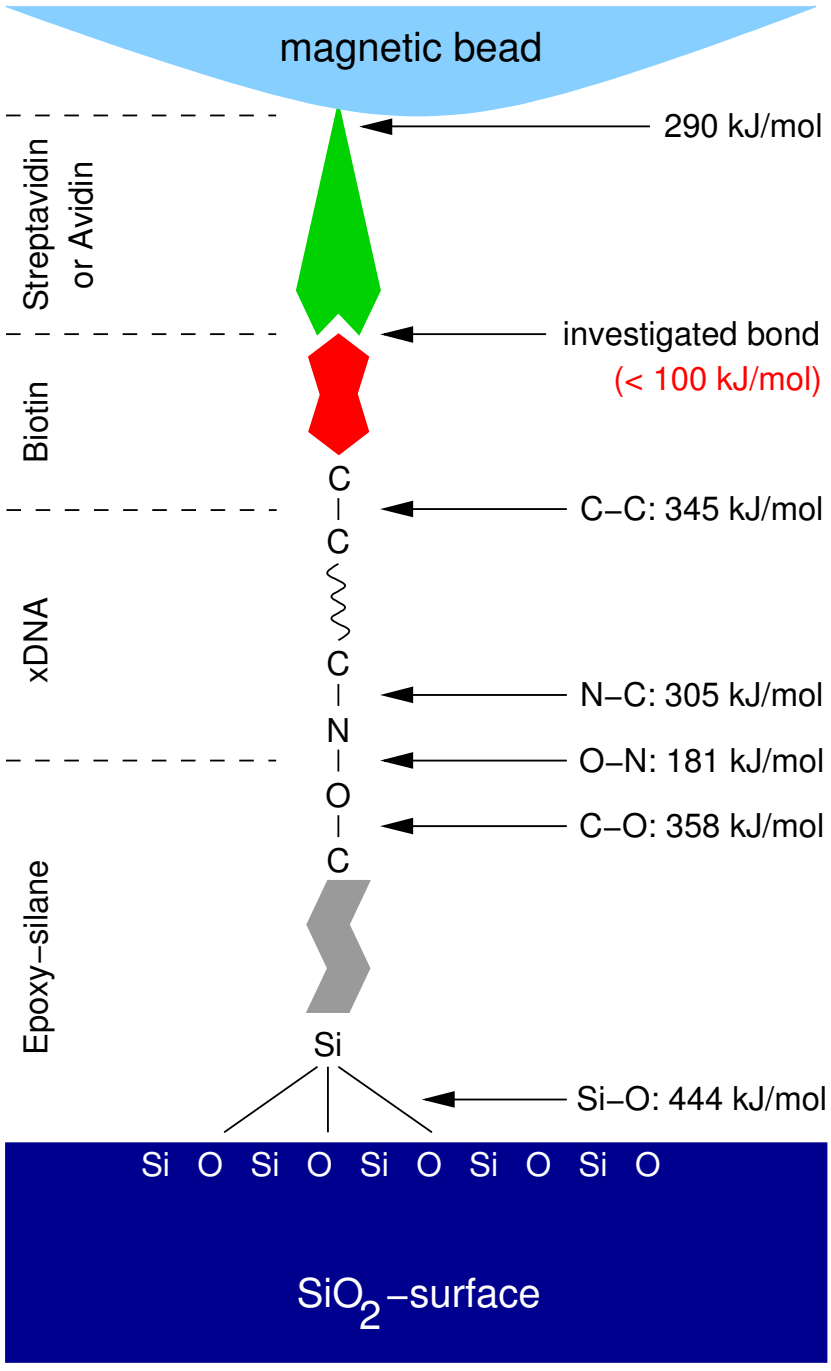

Figure 4.6: Bond enthalpy of all bonds between the surface and the magnetic marker. The xDNA strand has a phosphor backbone with a bond enthalpy for the P-O bond of 407 kJ/mol. Enthalpy values are from [108, 92]

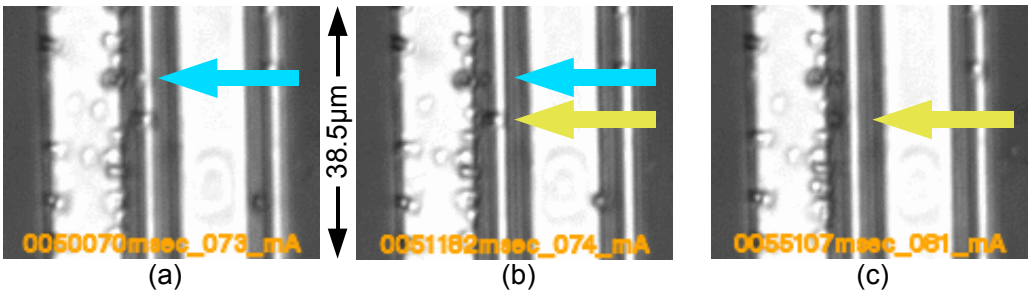

Figure 4.7: Three images of a recorded video. At 73 mA two streptavidin markers still bind to the biotin (a). At a current of 74 mA, the upper marker is ruptured (b), and at 81 mA the lower is ruptured (c). See CD for the complete video.

lower in the range of about 10-90 fN. Again, there are two maxima in this distribution, but they are not clearly separated. The first maximum (in the range of 0-40 fN) is at 15.9 fN ($\sigma_{\bar{x}} = 2,2$ fN) and the second maximum (in the range of 40-90 fN) is at 58,4 fN ($\sigma_{\bar{x}} = 5,0$ fN). It is apparent that for both bonds, the second maximum is about 4 times higher than the first maximum, which dashes the idea that this is just a double bond. A detailed explanation will be given below.

The streptavidin-biotin bond was tested additionally with markers from the SERADYN company (confer section 1.2). These markers did not bind very well, and therefore, only very few events could be measured (see the CD for all rupture events with the SERADYN markers). The mean value of these events is quite near to the first maxima of the rupture events with CHEMAGEN beads, at 57,6 fN ($\sigma_{\bar{x}} = 47,8$ fN).

The width of the maxima in these distributions is mainly caused by the distribution of the magnetic moment of the markers. The magnetic moment can only be measured for hundreds or thousands of beads, and then the average over all beads is calculated. Because the beads have a wide distribution in size, the magnetic moment has probably a similarly wide distribution.

In order to investigate the streptavidin-biotin bond even more with this method, we tried to put the system upside down. The streptavidin was put on the surface, where it can bind to gold, and biotinylated magnetic markers were used on top. Unfortunately, the biotinylated markers already bound directly to the gold surface without any streptavidin. Therefore, one major necessity of the experiments wasn't met, and the upside-down system could not be used.

The number of bonds between a bead and the surface depends on the

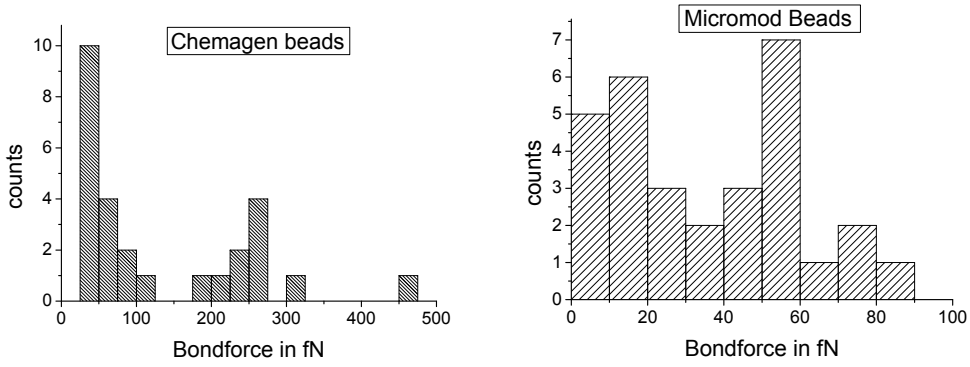

(a) streptavidin-biotin bond

(b) avidin-biotin bond

Figure 4.8: Distributions of the measured bond-forces for streptavidin-biotin (a) and avidin-biotin (b) bonds.

concentration of the biotinylated oligonucleotides on top of the surface. During the first experiments, a very high concentration was used and, therefore, nearly all markers bound to the surface and no marker could be ripped of. Of course, the reason for this was that the markers had several full bindings and, therefore, couldn't be ruptured. When no biotinylated oligonucleotides are on the surface, of course no bonds at all occurred (confer section 4.4). For the bond-force measurements in this thesis, the best concentration of oligonucleotides is between 10 and 1000 nM.

4.7 Discussion

At first, the very low bond-forces and the two maxima may look a little dubious, but after a thorough investigation it is clear that they fit very well to the investigations of other groups.

Other experimental [91, 28, 39, 40, 109, 134, 15] and theoretical publications [59, 70, 65, 121] already showed that the bond-force of ligand-receptor bonds is highly dependent on the loading-rate (i.e. the rate of force increase F'). Figures 4.9 and 4.10 present graphs of the streptavidin-biotin and avidin-biotin bond-forces in dependency of the corresponding loading-rate. The values for the bond-forces are from AFM measurements [97, 23], DFS measurements [91] and the results in this thesis. The bond-force is plotted

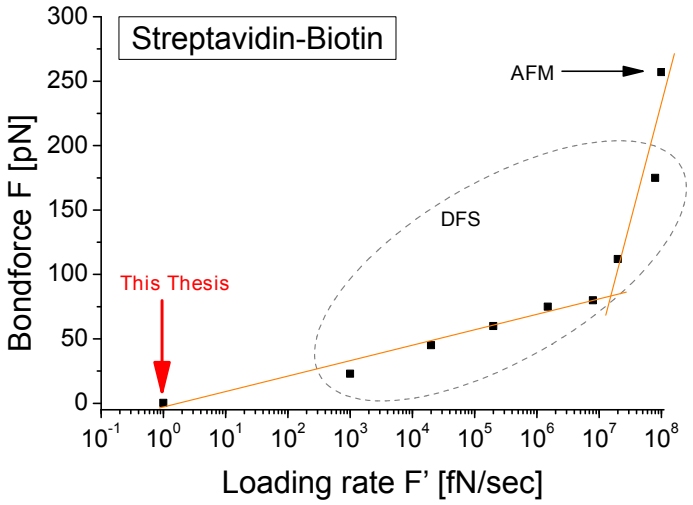

Figure 4.9: Bond-Force dependency on the loading rate for the streptavidin-biotin bond. The values for the atomic force microscopy (AFM) are from [97] and the values for the dynamic force spectroscopy (DFS) are from [91].

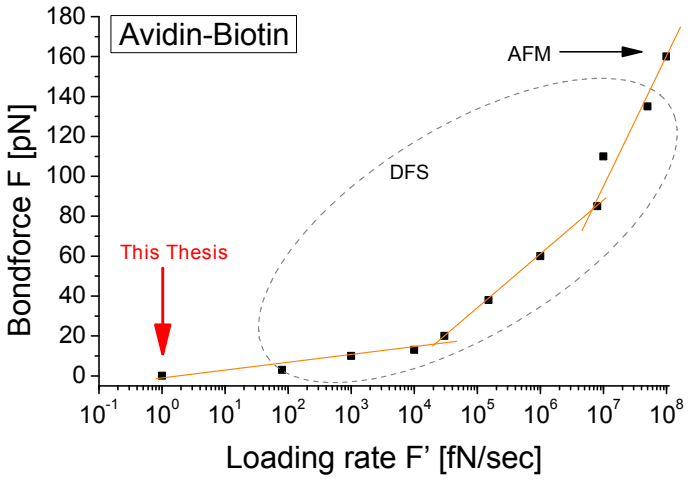

Figure 4.10: Bond-Force dependency on the loading rate for the avidin-biotin bond. The values for the atomic force microscopy (AFM) are from [44] and the values for the dynamic force spectroscopy (DFS) are from [91].

against the logarithm of the loading-rate, because it is proportional to the logarithm of the loading-rate. As it was already shown by MERKEL *et al.* in 1999 [91], the streptavidin-biotin bond can be divided in two linear regions, and the avidin-biotin bond can be divided into three linear regions. These different force regimes can be attributed to the behaviour of a one (or more) state energy potential that experiences an outer force (confer section 1.1.4 for the transition-state-theory and Kramers model). The bond-forces measured in this thesis extend the lower linear region for about 2 (avidin-biotin) to 3 (streptavidin-biotin) orders of magnitude down. At an extremely low loading-rate of only 1 fN/sec, the streptavidin-biotin bond-force is only ≈245 fN, and the avidin-biotin bond-force is only ≈58 fN. So the logarithmic dependence between bond-force and loading-rate is still valid for loading-rates down to 1 fN/sec.

Together with the low force events from [91], a linear fit can be applied to the measurements and the off rate k_{off} can be calculated. From equation 1.1 we can derive for the off rate: $k_{\text{off}} = \frac{x_\beta \cdot r_0}{k_B T}$. Using this equation, we get for the avidin-Biotin bond $k_{\text{off-Avidin}} = 1.3 \cdot 10^{-3}\,\text{sec}^{-1}$ and for streptavidin-biotin bond $k_{\text{off-Strept}} = 4.8 \cdot 10^{-4}\,\text{sec}^{-1}$, which is much higher than calorimetric measurements of GREEN in 1975 [57] ($k^{\text{Green}}_{\text{off-Avidin}} = 4 \cdot 10^{-8}\,\text{sec}^{-1}$ and $k^{\text{Green}}_{\text{off-Strept}} = 3 \cdot 10^{-6}\,\text{sec}^{-1}$). However, recent measurements [134], using label exchange experiments, showed an off rate for streptavidin-biotin between $k^{\text{Williams}}_{\text{off-Strept}} = 1 \cdot 10^{-5}\,\text{sec}^{-1}$ and $8.7 \cdot 10^{-7}\,\text{sec}^{-1}$ which is only a little bit higher than our measurements. Using only AFM measurements, all rupture events are quite far away from the natural off rate and that is the reason for the wide range. Because our measurements are much closer to the natural off rate the result of the linear regression is more precise.

While measuring very low bond-forces at very low loading-rates, another particular feature of the ligand-receptor bonds can be seen in the measurements. The fact that the second bond-force maxima for both investigated bonds is 4 times higher than the first maxima substantiates the theory of positive cooperativity for these ligand-receptor bonds. The affinity of these bonds, and with it the bond-force, only changes when the protein binds four ligands. There is no difference between one, two and three ligands bound to the protein. But with four ligands, a structural change in the protein induces a change of the affinity of the bond [133]. Only then, all four ligands add to the bond-force that is then four times higher than a single bond. For a more comprehensive explanation of the cooperativity in ligand-receptor bonds, see section 1.1.4. Even the single high force event for the streptavidin-biotin bond at 457 fN supports the cooperativity, because it is approximately twice the second maxima (244,7 fN with $\sigma_{\bar{x}} = 64,5\,\text{fN}$), and, therefore, corresponds

to a full double bond with two streptavidin proteins and eight biotin ligands.

Section 4.3 presented a dependency between the concentration of the biotin on the sample surface and the number of breakable and unbreakable ligand-receptor bonds. For concentrations above 1000 nM, no bonds could be ruptured in this setup. This is a clear indication for two or more full bonds, so the cumulated bond-force is higher than the highest bond-force that can be applied in this setup.

Several bonds per marker were very likely another problem for the examination of sulfur-gold bonds (confer section 4.1). Because the magnetic SH-markers can bind everywhere on the gold conducting line, there are most likely two or more bonds between the marker and the surface. And because it is not so easily possible to adjust the concentration of the gold atoms on the surface, as it is with biotinylated oligonucleotides, the sulfur-gold system is not really feasible.

In summary, this new method opens up the possibility for new ultra low force measurements with extremely low loading-rates. It is a very interesting tool to examine biological bonds, because it has several advantages. First of all, the maximum applied forces are strong enough for nearly all biological bonds (streptavidin-biotin is the strongest known non-covalent bond). But in contrast to e.g. AFM experiments, the loading-rate is very low. This means that the experimental conditions are more similar to the in vivo conditions of the ligand-receptor pair, although it is an in vitro experiment. This method can give more insights on the bond behaviour for near equilibrium conditions of biological bonds, and may add to new developments [105] in this research area.

Chapter 5

Exact positioning of single magnetic particles

In the last two chapters several examples for the manipulation of magnetic beads were presented, and bond-force measurements were introduced as an application for the manipulation techniques. This chapter presents the development of special designs to position *single* magnetic particles at predefined places. This positioning technique will be demonstrated for a special application in the subsequent chapter.

The preparation steps for the samples in this chapter are identical to those for the samples used for the manipulation experiments. Section 3.1 describes the basic processes in detail. The only difference is the used lithographic design.

5.1 Development of the lithographic design

The lithographic design of the conducting lines determines the generated magnetic field, and with it the behaviour of the magnetic particles on the sample surface (see section 3.3 for several examples). So, before a new design is created, the requirements for the magnetic field and the sample have to be clear.

The aim of the new design is the positioning of a single magnetic particle directly on top of a TMR sensor (confer chapter 6). To get reproducible results within one experiment it is desirable to have a sensor array with a single bead on every sensor. On the one hand, it would be preferable to occupy several positions with one conducting line, because the used IC-socket has only limited contacts. On the other hand, it would be beneficial if every position could be controlled individually. Balancing both requirements, a

rectangular conducting line was designed that allows the positioning at four predefined places (every corner of the square).

Figure 5.1(a) presents the rectangular design during a first positioning process. The magnetic particles in both top corners prove that this design works in principle, but some unwanted effects can also be seen. At the bottom left of the structure, a local maximum is at the round curve of the supply line(see respective particle agglutination). However, at the desired position in the corner, there are no particles. There are also several beads at the inner and outer edges of the rectangular design and not mainly in the corners.

Therefore, the design is changed to get rid of these problems. Figure 5.1(b) shows the second tested design to position four single particles at four predefined places. This design gets rid of the local maximum at the supply line, but there are still several particles on the outside of the structure. Also, the positioning is not really exact in this design. Most particles are near the inner corners, but not directly in the corner (see for example the bottom left corner).

This leads to a third design, presented in figure 5.1(c). Again, the supply line has no unwanted local maxima near the wanted positions, and the arched conducting lines allow very precise positioning of particles in the corners. Both top corners in figure 5.1(c) contain one single bead. The beads have a diameter of 1.5 μm and are positioned within an area of the same size. There are still some particles at the outer edge of the structure, but no one near the defined positions. After the development of this design, it was used for all positioning experiments in chapter 6. Still, some particular conditions have to be met to get good results in the positioning experiments.

5.2 Specialities regarding the measurement conditions

In order to position single beads at predefined places, some conditions have to be adjusted. First of all, the concentration of the beads in the water drop has to be right. A too high concentration results in more than one bead at every position, and with a too low concentration, there is a high probability that there is no bead at all in the vicinity of the generated magnetic field. For the used Micromod particles (confer section 1.2), concentrations of 2-5 μg/ml worked very well.

As another problem, clustering was observed during several experiments. The magnetic particles often clumped together, although the particles are superparamagnetic and their concentration in water was very low. To get

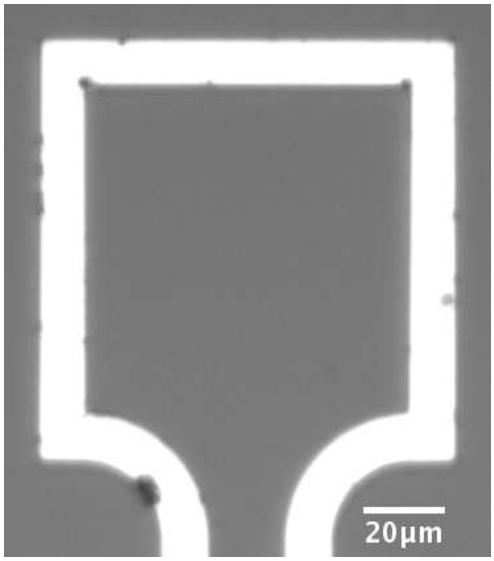

(a) First design tested for the positioning of single particles. Actual current is $I = 101\,\mathrm{mA}$.

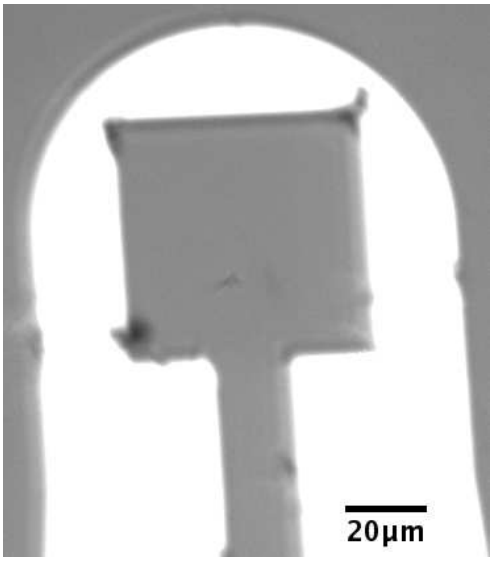

(b) Second tested design. Actual current is $I = 102\,\mathrm{mA}$.

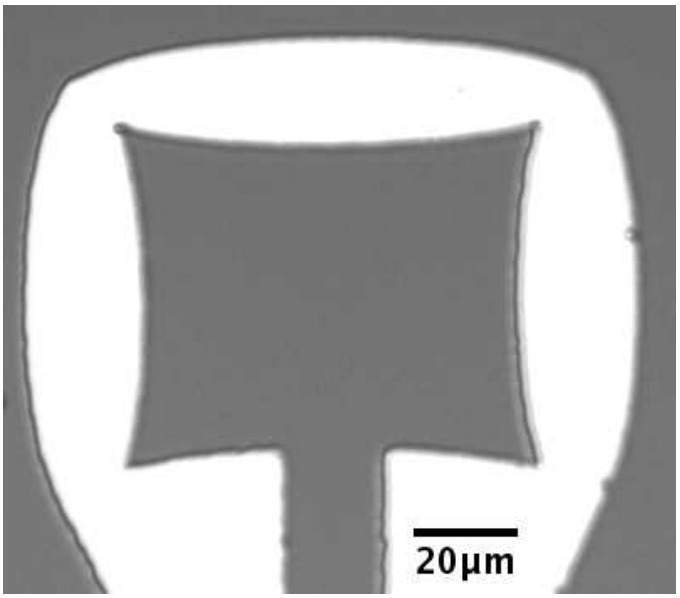

(c) Final design that was used for the positioning in chapter 6. Actual current is $I = 92\,\mathrm{mA}$.

Figure 5.1: Three different designs to position single magnetic particles. The design is evolving from (a) to (c). See the CD for complete videos of the positioning experiments.

rid of this clustering effect, the water-particle mixture has to be thoroughly shaken directly before the experiment. Luckily, these two requirements can easily be met, but they cannot be ignored.

5.3 Results and discussion

This chapter presents the development of a lithographic design that allows the positioning of four single magnetic markers at four predefined places. Taking all requirements into account, the design evolved over several steps (confer figure 5.1) into the final design that accomplishes all demands of the following experiments. For future developments of new lithographic designs, a finite-element simulation software could accelerate the development. The generated magnetic field can easily be calculated, and taking the friction in a liquid into account (see page 45 for more information on STOKES' LAW), the whole path of a single magnetic particle can be simulated. Such simulations would shorten the development time a lot and give more insights into the newly developed system.

Although the final design works well for the intended application, there is still room for improvements. Figure 5.1(c) shows the final design during the experiments. Two single beads are very well positioned in the top corners,

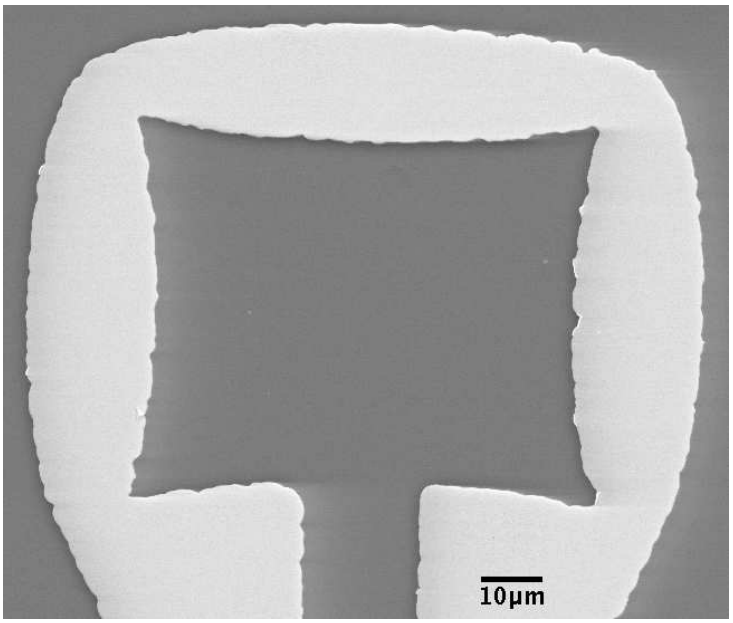

Figure 5.2: SEM image of the final design.

but there are also beads at the right edge of the structure. Thus, there are still some unwanted local maxima, and such additional maxima at the edges were observed in nearly all experiments. Examining the sample after the experiments in the SEM (see figure 5.2) exposes the reasons for the local maxima. There are still a lot of nooks and wrinkles at the edges of the structure. This is due to impurities in the optical resist or an mechanical oscillation of the laser lithography system (caused by a too small sample size). These small corners are responsible for the additional local maxima, to which some of the particles are drawn. So for very small or very exact structures, e-beam lithography should be used to minimise this problem.

This is another indication for the fact that the magnetic particles can be positioned within the same accuracy as the the lithography method. For bigger structures, the optical lithography is fine, but for very exact structures, e-beam lithography (which takes more time) has to be used.

The developed structure is used in the following chapter to position single magnetic markers on top of small rectangular TMR elements.

Chapter 6

A single magnetic particle on a TMR sensor

The positioning structure that was developed in chapter 5 is now used to position single magnetic particles on top of small TMR sensors. This is the first step to investigate the response of the sensors to single particles.

Many new applications are conceivable with these manipulation and positioning techniques. E.g., by using micro-patterning techniques for biomolecules [100] on a magnetoresistive sensor and applying a magnetic field out of plane to a bound biomolecule on top of the sensor, the sensor can give a force-distance curve for the bond between bead and surface.

6.1 Development of the TMR-Stack

A special TMR layer stack is developed for this experiments. The main requirement is that the TMR sensor can detect a single magnetic marker. It was shown theoretically that this is generally possible [18] when the element size is about the same size as the bead. But some special properties of the layer stack are wanted to improve the detection limit. Because the stray field of a single bead is quite small, it will only influence the soft magnetic layer of the TMR sensor locally. To avoid irreproducible switching induced by the small stray field of the particle, the TMR curve (i.e. resistance vs. external field) should have a slow ascending slope around zero magnetic field. This slow ascending slope in the TMR curve means for the TMR element that the softer top ferromagnet is switching reproducible from the parallel to the anti-parallel state. Such a switching behaviour is achieved through a special orthogonal pinning of the top and bottom ferromagnetic layers.

During the sputtering of the TMR layer stack, two magnetic masks are

applied. The lower part of the stack, including the bottom ferromagnet and the aluminium-oxide barrier, is sputtered with a 0° magnetic mask, and the upper part is sputtered in a 90° magnetic mask. So, the two ferromagnetic layers are aligned orthogonal to each other (confer figure 6.1a) and because of the pinning to an antiferromagnet, they stay that way when all external fields are removed.

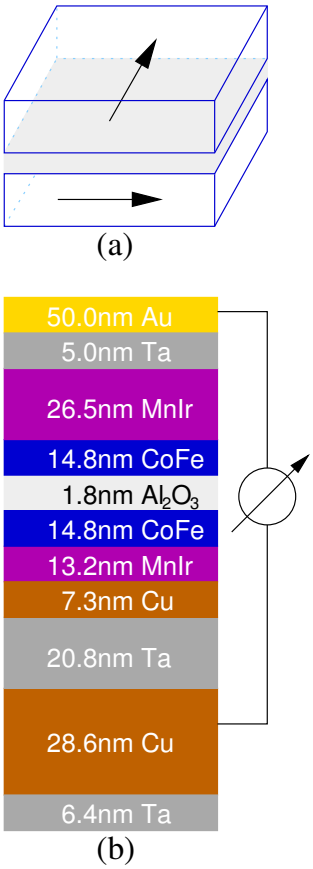

Figure 6.1: (a) Orthogonal pinning of top to bottom magnetic electrodes. (b) Layer stack used for the TMR sensor.

Several different layer stacks are sputtered (see section 2.1 for information about the used apparatus) and tested for their magnetic properties. The sputtered samples were structured using the UV-mask lithography system (confer section 2.3) with the standard mask (figure 2.3). After ion beam milling down to the bottom electrode (see section 2.2 for more information about the Ar-ion etching process) and removing the resist, the TMR and the I/V curves for the tunnel barrier of the layer stacks are measured. Because the development of the layer stack is not in the main focus of this thesis, only the measurements of the final layer stack are presented here [1].

Figure 6.1(b) presents the most suitable layer stack that was chosen for the experiments. The bottom electrode consists of two tantalum and two copper layers of different thicknesses, which are necessary for the Ar-ion etching process. The TMR element itself is composed of a strongly pinned cobalt iron layer (bottom), the tunnel barrier and a weakly pinned cobalt iron layer (top). A protective tantalum layer and a gold layer on top to connect the TMR elements completes the layer stack. The full stack from bottom to top can be written as: Ta(6.4 nm) / Cu(28.6 nm) / Ta(20.8 nm) / Cu (7.3 nm) / $Mn_{83}Ir_{17}$(13.2 nm) / $Co_{70}Fe_{30}$(14.8 nm) / Al_2O_3(1.8 nm) / $Co_{70}Fe_{30}$(14.8 nm) / $Mn_{83}Ir_{17}$ (26.5 nm) / Ta(5.0 nm) / Au(50 nm).

The top cobalt iron is pinned by a thicker manganese iridium layer than the bottom ferromagnetic layer. Because the exchange bias correlates with the thickness of the antiferromagnet (confer figure 1.14 on page 28), the magnetisation of the top ferromagnetic layer can rotate more easily (confer section 1.5.3). Together with the orthogonal directions of the pinning, this layer stack switches repro-

[1] The development and evaluation of different layer stacks for magnetoresistive sensors, used for the detection of single beads is done by coworkers of our group [19, 114]

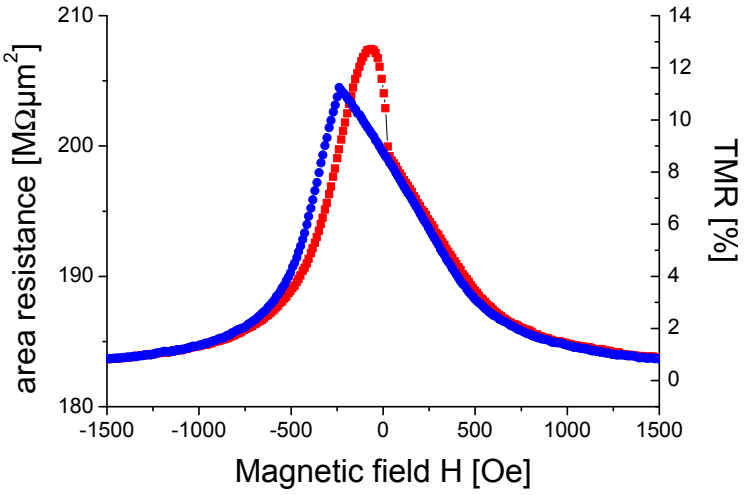

Figure 6.2: Major loop from the final layer stack of a typical 300×300 μm^2 TMR element.

ducable around zero field. So it achieves the slowly ascending slope of the TMR curve and therefore prevents any irreproducible switching of the soft magnetic layer.

Results and discussion

Figure 6.2 presents the measurement of a typical 300×300 μm^2 TMR element. At an area resistance between 183 and 210 M$\Omega\mu$m^2, the measured TMR ratio is 13.1 %. The in-plane magnetic field is applied parallel to the pinning of the bottom electrode. For further characterisation of the layer stack, I/V curves are measured and evaluated. Figure 6.4(a) shows a measured I/V curve for this element. For the evaluation, the plot was differentiated and fitted with standard software, see figure 6.4(b). Using BRINKMANS equations (confer page 26) with an effective

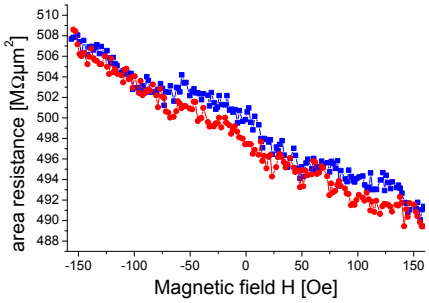

Figure 6.3: Minor loop from the final layer stack of a typical 300×300 μm^2 TMR element.

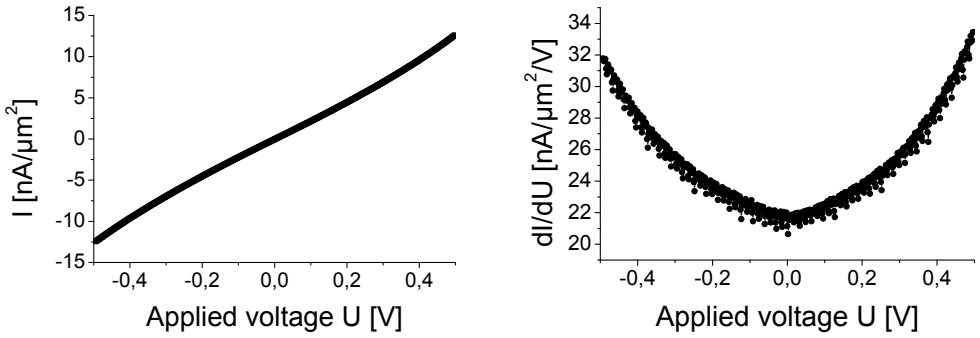

(a) Original I/V curve.

(b) Differentiated I/V plot that is used for the BRINKMAN fit.

Figure 6.4: I/V measurements of the used layer stack.

electron mass of $m_{\text{eff}} = 0.4 \cdot \mathrm{m_E}$, the barrier height has a reasonable value of $\nu = 2.62\,\text{eV}$. The barrier thickness of $b = 1.95\,\text{nm}$ is a little bit thicker but still close to the expected 1.8 nm. The asymmetry $d\nu = -0.22\,\text{eV}$ lies also within the expected range.

The used TMR layer stack was not developed to have the highest possible TMR ratio or to get a very robust tunnel barrier. The aim was instead a slow ascending slope around zero magnetic field. Therefore, the TMR ratio of 13.1 % is not very high, but still quite good for this system and a large TMR element. An annealing of the whole sample cannot be done, because it would destroy the orthogonal pinning of the two electrodes. But an unannealed tunnel barrier is not as good as an annealed barrier. The TMR ratio is less for an unannealed TMR element and the barrier can easily be destroyed (an applied voltage of 1 Volt mostly destroys the tunnel barrier). Also, the parameters given by the BRINKMAN-fit are not extremely good, but reasonable for the targeted application. In any case, the main goal, i.e. a slow ascending slope around zero field and no irreproducible switching, is achieved nicely (see minor loop in figure 6.3).

6.2 Sample preparation

The complete sample preparation for the TMR elements and the manipulation system on top is a very elaborate process. It involves four different

lithography steps and takes about 10 days altogether. This section gives a detailed description of all preparation steps.

The first preparation step is the sputtering of the TMR layer stack. While the development of the stack was described before, there are two things that are vital for the success of sputtering a working TMR layer system. The size of the Si-wafer substrate has to be 15×15 mm, because this is the minimum size for both optical lithography steps, and it is the maximum size for the sputtering in a magnetic mask. It is also vital that the substrate is electrically connected to the substrate holder with silver paste. Otherwise, the tunnel barrier is broken. The TMR layer stack is sputtered in the professional sputtering machine CLAB 600 from LEYBOLD (confer section 2.1).

Starting with the Si-wafer and the TMR layer stack on top, the samples undergo many steps until the final structure is achieved. Figure 6.5 illustrates all necessary steps of the structuring process. As first lithographic step, the supply line for the bottom contact is structured with e-beam lithography directly in the center of the sample surface (a) (please see section 2.4 for more information on e-beam lithography). This structure is etched for 1750 secs (see section 2.2 for more information about the etching process) into the layer system (b) before the resist is removed (c) and the second e-beam lithography step is performed. Now, the design for the TMR elements is written to the e-beam resist (d). This and all subsequent lithography steps have to be aligned to the first structure. To do this more easily, a special cross like structure is written during the first lithographic step in the center of the design. After the development of the resist, the sample is etched again. The etching time is now 2000 secs, so only the bottom contact lines and the elements remain (e). Before the resist is removed, the elements are covered with an insulating layer of 100 nm SiO_2 (f). Removing the resist leaves the protected TMR elements with an unprotected top contact (g). The bottom contact of the element is contacted through a short-circuited TMR element (see right element in the sketches).

To structure the contact lines, optical lithography is used because it is faster for big structures. For the optical lithography, the area is exposed where the resist is removed during the development (h), because a positive resist is used (please see section 2.3 for more information about the optical lithography). A layer of 50 nm gold is sputtered as contact lines for the TMR elements (i). Below and above the gold layer, tantalum is used as an adhesive agent between gold and glass. The tantalum is essential, because without the adhesive agent the protection layer is not completely sealed, and so the TMR elements can easily be destroyed. After removing the resist, the structuring process for the TMR elements is finished. Then, all elements are measured and checked.

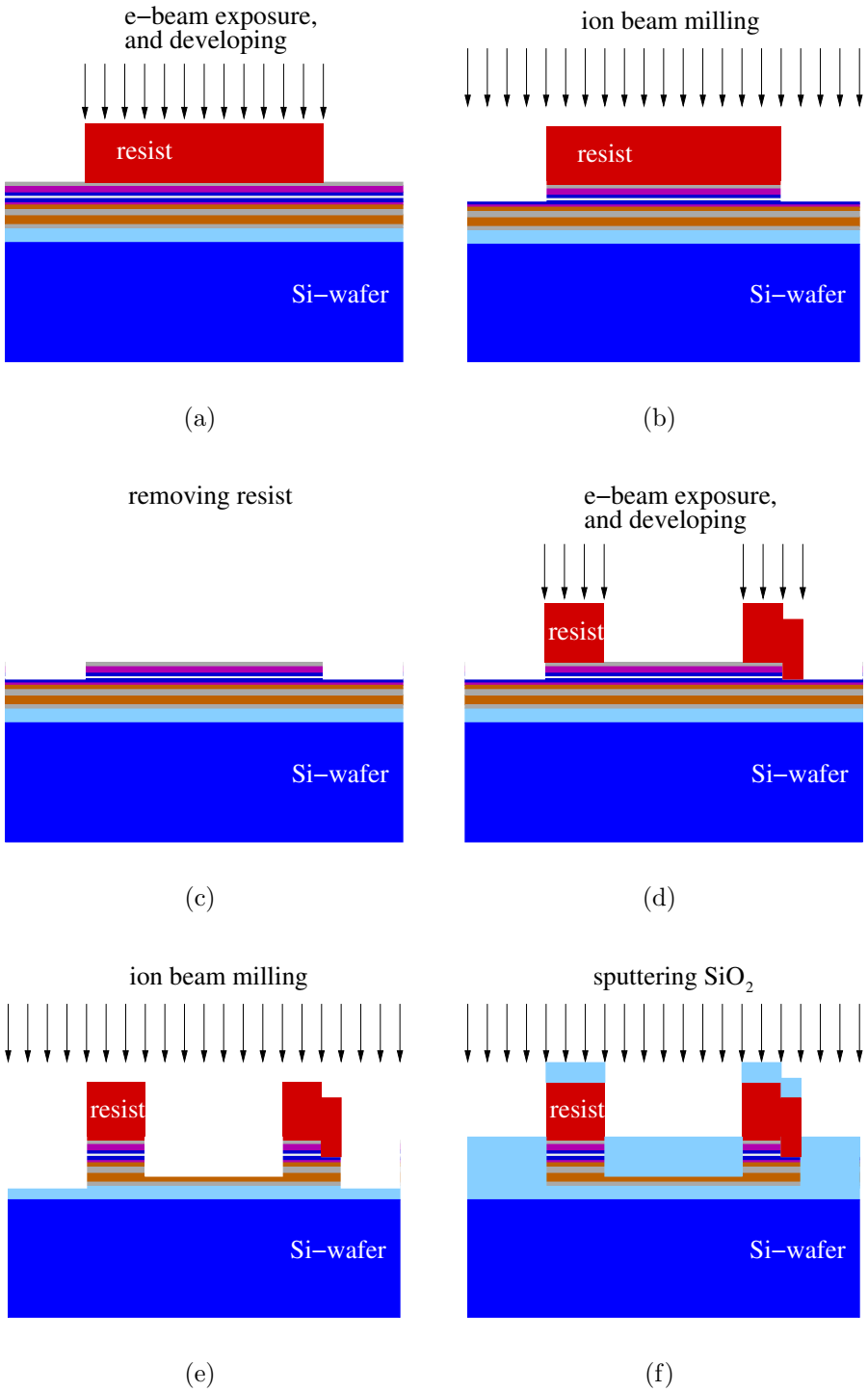

Figure 6.5: Side view of all preparation steps for the TMR elements and the manipulation system on top.

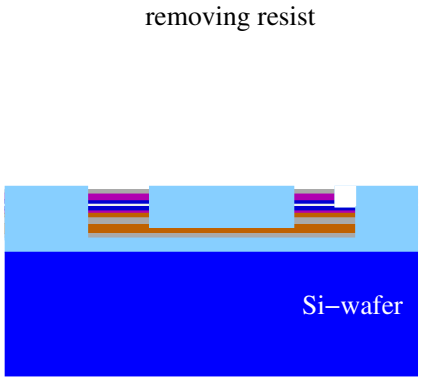
removing resist
Si–wafer

(g)

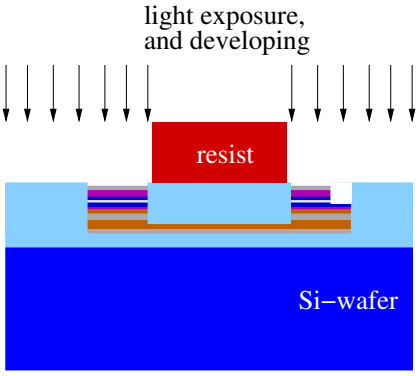
light exposure,
and developing
resist
Si–wafer

(h)

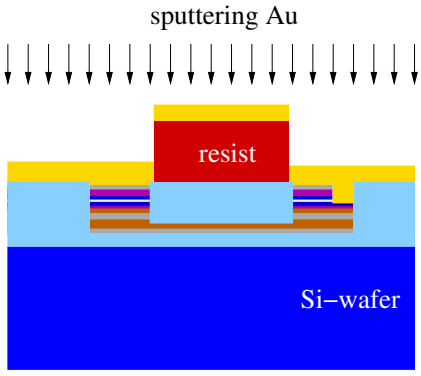
sputtering Au
resist
Si–wafer

(i)

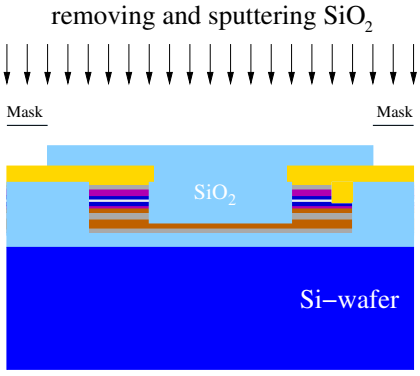
removing and sputtering SiO2
Mask
Mask
SiO2
Si–wafer

(j)

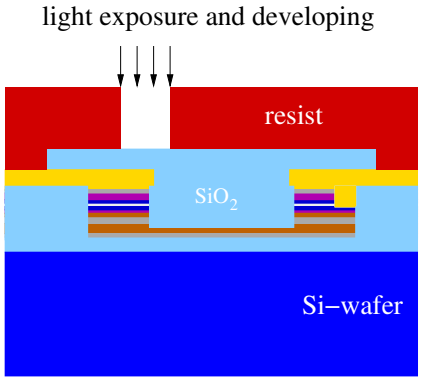
light exposure and developing
resist
SiO2
Si–wafer

(k)

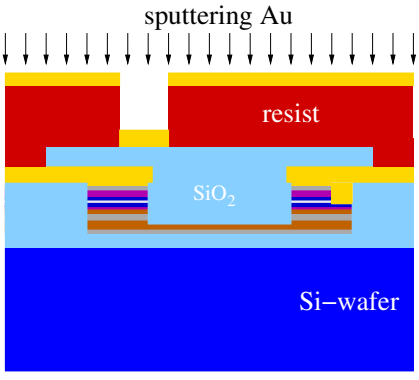
sputtering Au
resist
SiO2
Si–wafer

(l)

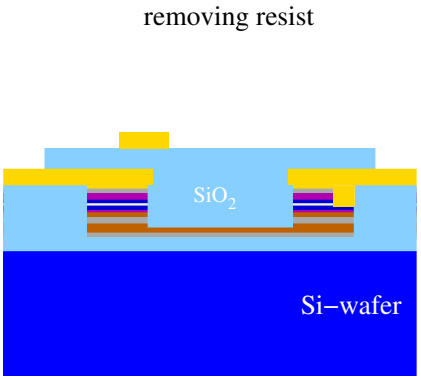

(m) Side view of the completed sample.

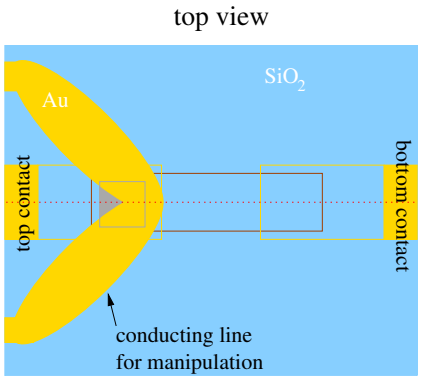

(n) Top view sketch of the finished sample. The red dashed line shows the cut of the side view.

Only if the elements are fine, another protective SiO_2 layer of 100 nm is sputtered in a mask that keeps the contact pads free (j). With the final lithography step (k), the design for the positioning system is structured on top of the TMR elements (chapter 5 describes in detail the development of the positioning system). 100 nm gold is sputtered into the structured positioning design (l), again using tantalum as adhesive agent between SiO_2 and gold. After removing the resist, the sample is finished (m).

The TMR element on the left can be contacted by the top gold contact to the left and the bottom contact through the short-circuited element on the right. Besides the supply lines, it is completely enclosed in insulating SiO_2. The top view of the completed sample (n) reveals how the positioning system for the magnetic markers is set on top of the elements. Exact alignment is again mandatory for successful positioning.

Finally, the completed sample is cut in smaller pieces to fit into a IC-socket. It is glued into the socket with silver paste and connected by wire-bonding. Thus, the sample can be measured easily in the given setup (confer section 2.7 for more information about the measuring system).

For these samples, the conducting lines of the positioning system are not embedded into the underlying SiO_2 layer, as it was done in the chapters before. This was necessary because we want to maximise the magnetic stray field of the markers, and to achieve this, the distance between marker and sensor should be as small as possible. The protection layer between the conducting line for the positioning system and the water is not mandatory,

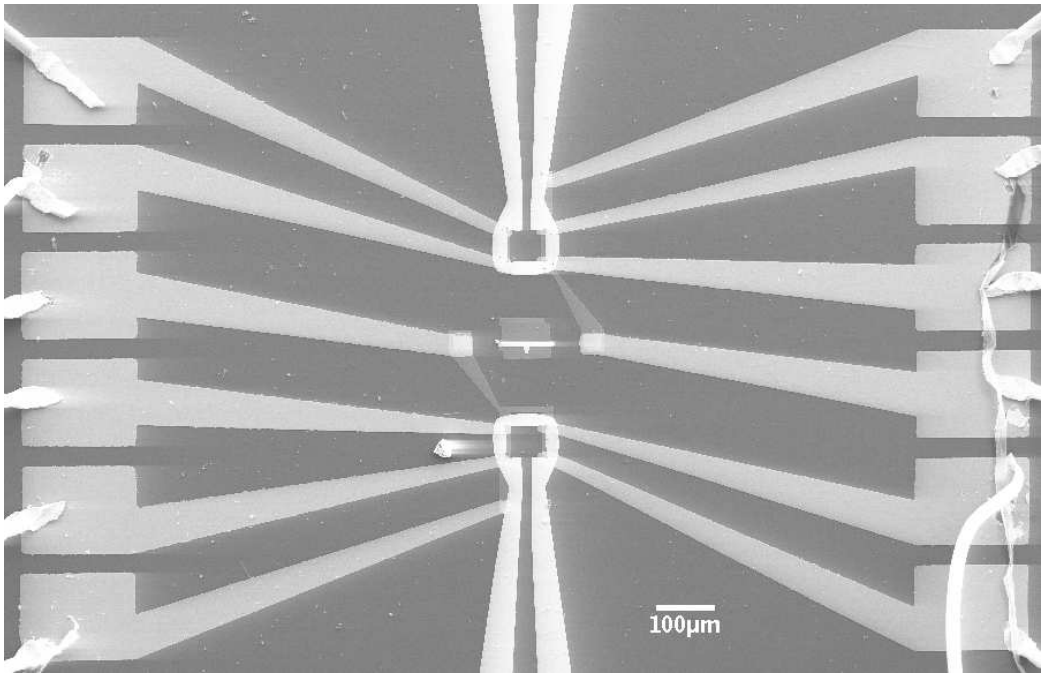

Figure 6.6: SEM image of the completed sample.

and so this setup is chosen. The magnetic marker can be positioned in the corner, right beside the conducting line, so the distance between marker and sensor is only about 150 nm (100 nm SiO_2 protection layer and 50 nm gold from the top contact line).

6.3 Results

Figure 6.6 presents an SEM image of a working sample. The wire-bonded contact pads which connect to the TMR elements can be seen on both sides. The conducting lines for the positioning structure come from the top and bottom of the image. The alignment cross is right in the center, and two larger test TMR elements are right and left from the alignment cross.

The size of the TMR elements on the sample is: $2\times2\,\mu m^2$, $4\times4\,\mu m^2$, $6\times6\,\mu m^2$ and $8\times8\,\mu m^2$. For test purposes, two extra $30\times30\,\mu m^2$ elements were designed. Exemplarily, the measurements of a $2\times2\,\mu m^2$ element are presented here. Figure 6.7 shows the area resistance and TMR ratio of the element. The maximal TMR ration is 21.8 % at an area resistance of about 260 to 320 $M\Omega\mu m^2$. Again, there is the slow ascending slope at zero field. Measuring the I/V curve of the element (see figure 6.8(a)) and applying the

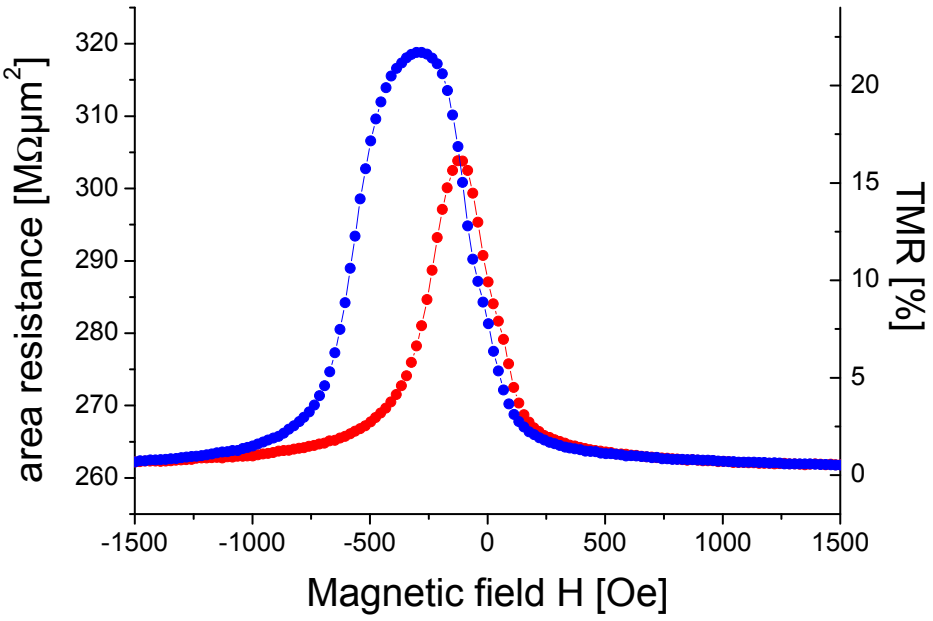

Figure 6.7: Major loop of a typical $2{\times}2\,\mu\mathrm{m}^2$ TMR element, of the structured sample.

BRINKMAN fit to the differentiated plot (b) gives the following results: barrier height of $\nu = 1.25\,\mathrm{eV}$, a barrier thickness of $b = 2.65\,\mathrm{nm}$ and an asymmetry $d\nu = -0.24\,\mathrm{eV}$. The other elements show similar values for the BRINKMAN fit and the TMR ratio.

As expected from chapter 5, the positioning system on top of the elements works quite well. Figure 6.9 shows two images of a video that was recorded during a positioning experiment. A single magnetic marker is drawn into the corner of the upper positioning structure by the magnetic gradient field. The images show the marker directly before (a) and after (b) the marker reaches the corner (center of the red circle marks the position of the bead). Although the conducting line is not embedded into the SiO_2, the positioning still works. Other recorded videos show that the conducting line is an obstacle, but many markers can easily leap over this barrier. It is no real drawback for the positioning system, therefore.

In the example of figure 6.9, the upper conducting line is not exactly aligned to the TMR elements, and so the marker is positioned beside the element and not directly on top of it (the TMR element in figure 6.9(b)

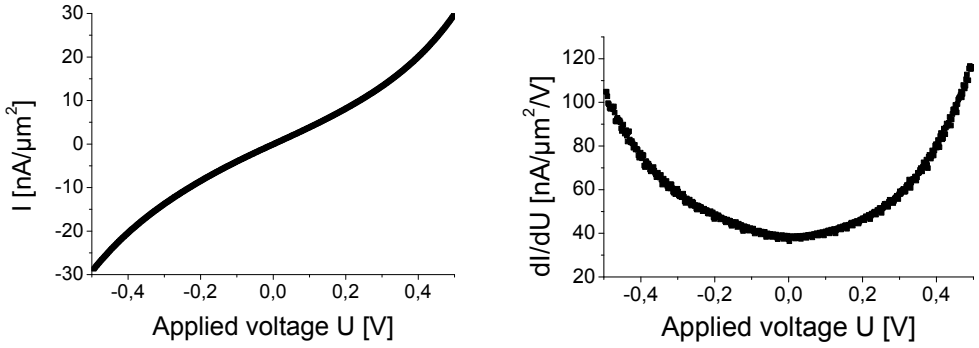

(a) Original I/V curve.

(b) Differentiated I/V plot that is used for the BRINKMAN fit.

Figure 6.8: I/V measurements of the $2\times2\,\mu m^2$ TMR element.

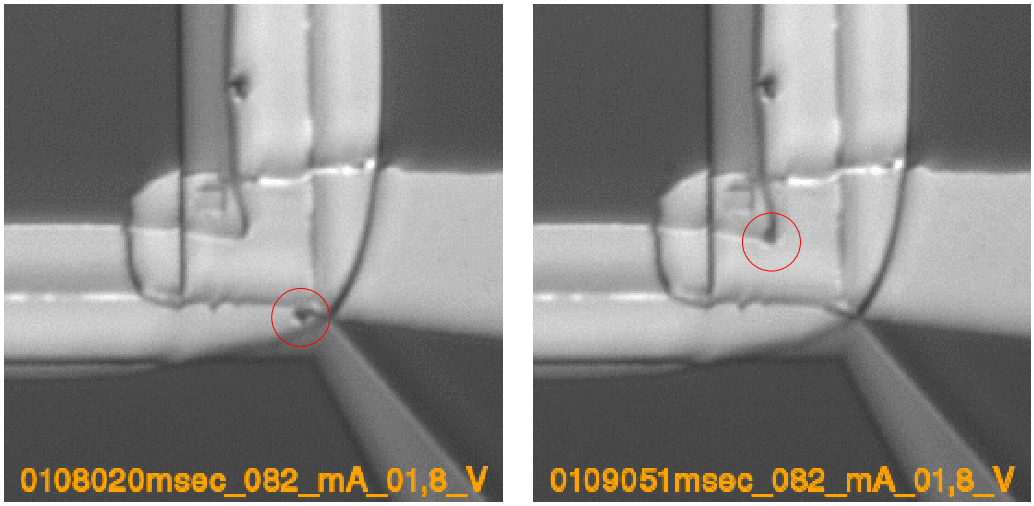

(a) (b)

Figure 6.9: Placement of a single magnetic marker (MICROMOD marker with a diameter of $1.5\,\mu m$) into the corner of the positioning structure, right before (a) and after (b) the marker reaches the final position. The images have a size of $86.7 \times 86.7\,\mu m^2$. See CD for the complete video.

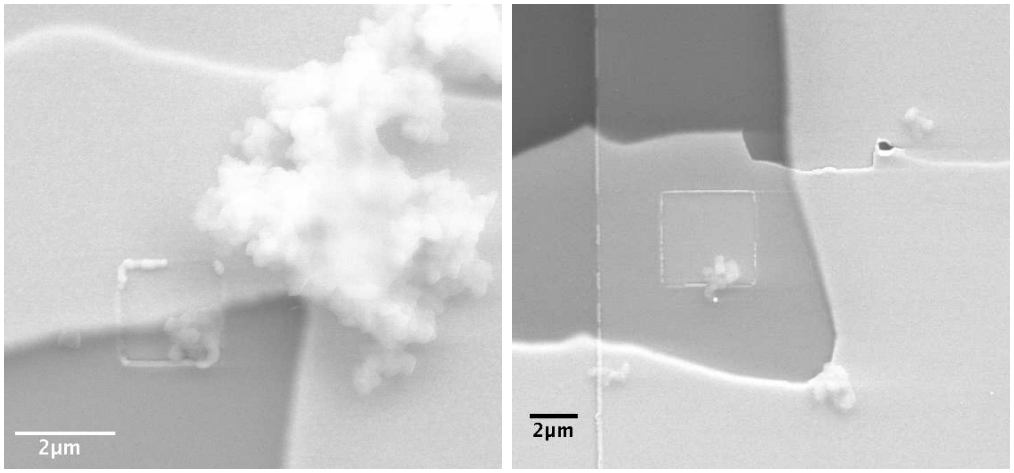

(a) Single marker on a $2\times2\,\mu m^2$ TMR element, besides a big agglutination of markers.

(b) Single marker on a $4\times4\,\mu m^2$ TMR element.

Figure 6.10: SEM images of well positioned single magnetic markers (MICROMOD, $\varnothing$=1.5 μm).

is the square that is top left from the magnetic bead). In this situation, another effect helps to position the magnetic markers directly on top of the TMR elements. As can be seen in SEM images (confer figure 6.10), the stray field of the TMR element itself draws the magnetic particle on top of the element. So, in order to position a magnetic marker on a magnetoresistive element, the positioning system does not have to be very exact, because the stray field of the element does the rest.

Figure 6.10 presents two SEM images as examples for a successful positioning. Figure 6.10(a) shows a single magnetic particle on a $2\times2\,\mu m^2$ TMR element besides a big agglutination of markers on top of the corner of the positioning system. The second image (b) presents a single 1 μm sized magnetic marker on a $4\times4\,\mu m^2$ sized TMR element (it is the same element as in figure 6.9). This image reveals clearly the two local maxima on the sample. One bead is directly in the corner of the positioning system (lower right) and one bead is on the TMR element (center). Therefore, the stray field of the TMR element adds a local maximum to the magnetic gradient field of the positioning system.

Until today there is one major drawback of these experiments. No TMR element survived the drop of water during the positioning. Although the

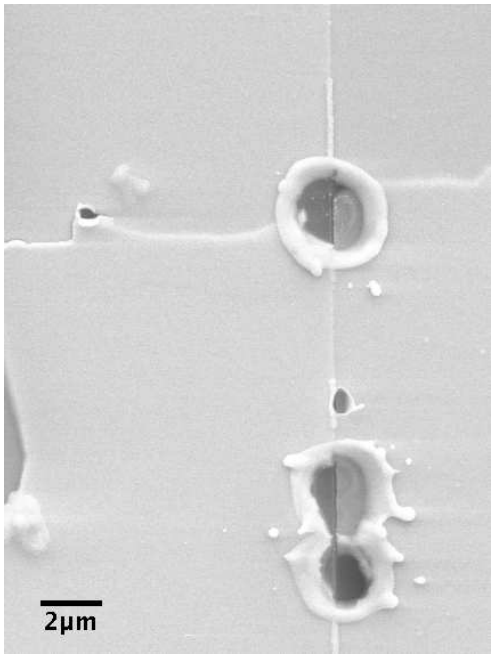

(a) SEM image of holes that destroyed the sample.

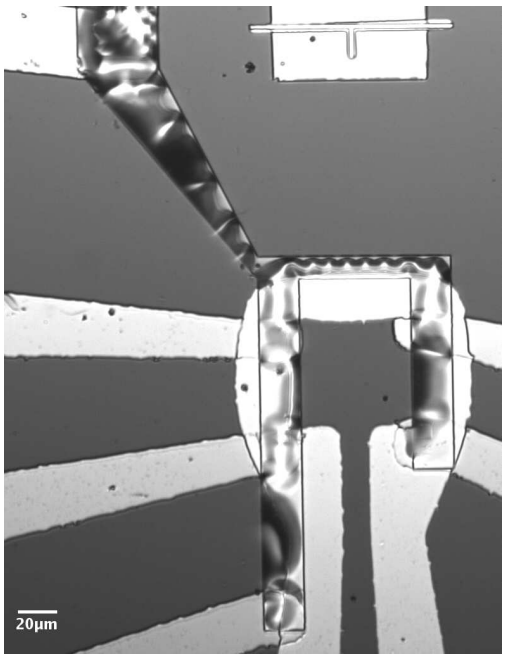

(b) Video image of water, destroying the bottom contact line of the TMR elements.

Figure 6.11: Destruction of the TMR elements.

SiO_2 protection layer is made precisely, the water always seems to find a way to creep below it. On some samples, the destruction can be seen easily, but on others, the tunnel barrier just seems to be destroyed without reason. Figure 6.11 presents two examples for obvious destructions. The first image (a) shows some holes that originate from the positioning experiments. Right at the end of the experiments, when the water drop dried out, several holes all over the sample sprung up and short-circuited the top and bottom contacts of the TMR elements through the protection layer. The reason for this is yet unclear. The second image (b) shows some dark structures directly on top of the bottom contact line. It looks similar to the splintered glass that was presented in section 3.2. The water somehow finds a way below the SiO_2 protection layer and destroys the TMR elements. These were just two examples where the reason for the short-circuited TMR elements was obvious. Other samples showed no visible signs of destruction, but all TMR elements were always short-circuited after the positioning.

6.4 Discussion

The main goal of this chapter, i.e. the positioning of single magnetic markers on top of small TMR elements, is achieved, although the TMR elements don't survive the drop of water, yet. The fabrication of a sample involves many steps (confer figure 6.5) and is, therefore, easily vulnerable to failures. The fabrication process needs several improvements until the TMR elements are functioning. The alignment for both optical lithography steps had to be improved several times, and a bottom contact over the whole sample area always lead to short-circuited TMR elements, because the insulating layer was not sealed everywhere.

But finally, it was shown that the samples work in principle. The TMR elements are measured right before the positioning of the magnetic markers, and show the wanted results. The positioning also works well, as shown for several examples.

To prevent the destruction of the TMR elements and to improve the positioning system, two suggestions for future experiments are made. Using e-beam lithography for the positioning system would greatly improve the accuracy of the alignment. The exposure of such big structures takes much longer with e-beam lithography than with optical lithography, but the better accuracy will be worth it. Especially for smaller beads that will be used in future experiments, the e-beam lithography will be mandatory.

A different coating technique is proposed to prevent the destruction of the elements. Using a Chemical Vapour Deposition (CVD) coating technique instead of sputtering, the protection layer probably has less defects and is, therefore, less vulnerable to the water molecules. A CVD coating machine will be soon available in our group, and so the CVD technique will be tried in future experiments.

Summary and Outlook

The use of magnetic markers and magnetoresistive sensor elements is a new research area that is very promising for the development of small and powerful biosensors. The magnetic approach has three major advantages over the conventional optical biosensors. The magnetoresistive sensors can be read out very easily, their overall production costs are very cheap because they are standard micro-chip techniques, and the magnetic markers, and with it the attached biomolecules, can be directly manipulated with an outer magnetic field.

This thesis presents an on-chip manipulation and positioning system for single magnetic markers. The setup is simple and easily customisable. Conducting lines are patterned with optical lithography on a Si-wafer chip. An applied current through the conducting lines creates a magnetic gradient field that interacts with the magnetic markers, so the magnetic markers follow the gradient of the field to a local maximum.

It is shown that this manipulation and positioning technique works in principle and, moreover, several applications are introduced. One application is a special design that allows the transportation of several markers and the positioning in predefined places. Additionally, the trapping of markers inside a ring structure is studied and the effects of an applied electric field on the magnetic markers are investigated. Single magnetic markers were positioned directly on top of small TMR sensors using a specifically designed structure. The magnetic stray field of the magnetoresistive sensors helped to position the magnetic markers on top of the sensors, although this is not necessary. The accuracy of the positioning system only depends on the accuracy of the used lithography. So for e-beam lithography the accuracy is below 100 nm. The manipulation system is eminently suited for a small handheld biosensor device because it fits together with the sensors directly on the Si-wafer chip.

As an application of the manipulation technique, bond-force measurements between two biomolecules were done. One biomolecule is attached to the sample surface and the other is connected to a magnetic marker. After the biomolecules bound, a magnetic field is turned on using the conducting

lines on the chip. The magnetic gradient field is slowly increased until the bonds between the biomolecules break. This event is monitored with a CCD-camera and evaluated to calculate the corresponding bond-force. Compared to other bond-force measurements, this method has an extremely low loading-rate (≈1 fN/sec) and, therefore, the measured bond-forces are extremely low as well. The two well known bonds streptavidin-biotin and avidin-biotin were investigated, and very low bond-forces were measured (full bond of streptavidin-biotin: ≈245 fN, avidin-biotin: ≈58 fN). The measured bond-forces are about 1000 times lower than produced by earlier measurements, which fits well to the loading-rate, which is also about 1000 times lower. This method also provides evidence for the cooperativity of these ligand-receptor bonds.

Several enhancements for the techniques are planned to improve future experiments. First of all, it is planned to use a CVD coating technique to improve the protection layer of the TMR elements, so they survive the aqueous conditions during the positioning. Afterwards, different layer stacks for the sensor can be tested, as well as smaller magnetic particles. With a single bead that binds to the surface of a magnetoresistive sensor and an applied out of plane magnetic field, force-distant curves can be measured using the sensor signal. To accelerate the development time, finite element simulations are proposed as a first step in the evolution of new designs.

Because of the exceptionally low loading rates, the method for the measurement of bond-forces is very interesting for other molecules too. In order to enhance the maximum possible force, Astrit Shoshi started experiments in our group to add magnetic materials to the conducting lines. For example, he added a GMR trilayer below the conducting line to enhance the magnetic field strength, without having to apply an external magnetic field.

Additionally, the combination of this manipulation technique with microfluidic systems [83, 125] will be very interesting for future experiments. The fluidic system allows a fast transportation of magnetic markers over large distances, and the magnetic manipulation system facilitates the exact positioning.

At a later stage, it would also be very interesting to apply this on-chip manipulation technique to a complete cell that has to be grown directly on top of the structured design. With a magnetic marker inside the cell and a sensor array below, measurements of the viscosity in different areas of the cell could be done. It would also be very interesting for in-vivo measurements of intermolecular forces, and to determine where in the cell a specific biomolecule can bind.

List of Figures

Bibliography

[1] Marcelo Alonso and Edward J. Finn. *Physik*. Addison-Wesley Verlag, 1977.

[2] Geoff Anderson, Yiming Huai, and Lena Miloslawsky. CoFe/IrMn exchange biased top, bottom, and dual spin valves. volume 87, pages 6989–6991. AIP, 2000.

[3] R. C. Anderson, X. Su, G. J. Bogdan, and J. Fenton. A miniature integrated device for automated multistep genetic assays. *Nucleic Acids Res*, 28(12):E60, Jun 2000.

[4] E. Arzt and W. D. Nix. A model for the effect of line width and mechanical strength on electromigration failure of interconnects with "near-bamboo" grain structures. *Journal of Materials Research*, 6:731–736, April 1991.

[5] M. N. Baibich, J. M. Broto, A. Fert, F. Nguyen van Dau, F. Petroff, P. Etienne, G. Creuzet, A. Friederich, and J. Chazelas. Giant magnetoresistance of (001)Fe/(001)Cr magnetic superlattices. *Physical Review Letters*, 61:2472–2475, November 1988.

[6] D. R. Baselt, G. U. Lee, M. Natesan, S. W. Metzger, P. E. Sheehan, and R. J. Colton. A biosensor based on magnetoresistance technology. *Biosens Bioelectron*, 13(7-8):731–739, Oct 1998.

[7] Andreas R. Bausch, Winfried Moller, and Erich Sackmann. Measurement of Local Viscoelasticity and Forces in Living Cells by Magnetic Tweezers. *Biophys. J.*, 76(1):573–579, 1999.

[8] G. I. Bell. Models for the specific adhesion of cells to cells. *Science*, 200(4342):618–627, May 1978.

[9] Kaspar Berneis, Michael La Belle, Patricia J. Blanche, and Ronald M. Krauss. Analysis and quantitation of biotinylated apob-containing

lipoproteins with streptavidin-cy3. *Journal of Lipid Research*, 43:1155–1159, 2002.

[10] H. Berney, J. West, E. Haefele, J. Alderman, W. Lane, and J. K. Collins. A dna diagnostic biosensor: development, characterisation and performance. *Sensors and Actuators B: Chemical*, 68(1-3):100–108, August 2000.

[11] F. Bertucci, K. Bernard, B. Loriod, Y. C. Chang, S. Granjeaud, D. Birnbaum, C. Nguyen, K. Peck, and B. R. Jordan. Sensitivity issues in DNA array-based expression measurements and performance of nylon microarrays for small samples. *Hum Mol Genet*, 8(9):1715–1722, Sep 1999.

[12] Binasch, Grünberg, Saurenbach, and Zinn. Enhanced magnetoresistance in layered magnetic structures with antiferromagnetic interlayer exchange. *Physical Review B. Condensed Matter*, 39(7):4828–4830, Mar 1989.

[13] Biochemikalien-Lexikon - Biotin. http://www.omikron-online.de/cyberchem/cheminfo/0546-lex.htm, 2004.

[14] M. Boas. *Biochem. J.*, 21:712, 1927.

[15] Pierre Bongrand. Ligand-receptor interactions. *Rep. Prog. Phys.*, 62:921–968, 1999.

[16] A. M. Bratkovsky. Tunneling of electrons in conventional and half-metallic systems: Towards very large magnetoresistance. *Physical Review B*, 56:2344?–2347, 1997.

[17] W. F. Brinkman, R. C. Dynes, and J. M. Rowell. Tunneling conductance of asymmetrical barriers. *Journal of Applied Physics*, 41(5):1915–1921, 1970.

[18] H. Brückl, M. Brzeska, D. Brinkmann, J. Schotter, G. Reiss, W. Schepper, P. Kamp, and A. Becker. Magnetoresistive logic and biochip. *Journal of Magnetism and Magnetic Materials*, 282:219–224, November 2004.

[19] M. Brzeska, M. Justus, J. Schotter, K. Rott, G. Reiss, and H. Brückl. Development of magnetoresistive sensors for the detection of single molecules by magnetic markers. *Molecular Physics Reports*, 39:32–38, 2004.

[20] BVK - Bundesverband Deutscher Kapitalbeteiligungsgesellschaften. http://www.bvk-ev.de/, 2005.

[21] Louis Chaiet and Frank J. Wolf. The properties of streptavidin, a biotin-binding protein produced by streptomycetes. *Archives of Biochemistry and Biophysics*, 106:1–5, 1964.

[22] Chemagen Biopolymer Technologie AG. http://www.chemagen.com/, 2005.

[23] A Chilkoti, T Boland, BD Ratner, and PS Stayton. The relationship between ligand-binding thermodynamics and protein-ligand interaction forces measured by atomic force microscopy. *Biophys. J.*, 69(5):2125–2130, 1995.

[24] V. Chu, S. Freitag, I. L. Trong, R. E. Stenkamp, and P. S. Stayton. Thermodynamic and structural consequences of flexible loop deletion by circular permutation in the streptavidin-biotin system. *Protein Sci*, 7(4):848–859, 1998.

[25] Computer Simulation Laboratory. What is electromigration? http://www.csl.mete.metu.edu.tr/Electromigration/emig.htm, 2005.

[26] G. Czihak, H. Langer, and H. Ziegler, editors. *Biologie*. Springer Verlag, 4 edition, 1990.

[27] U Dammer, M Hegner, D Anselmetti, P Wagner, M Dreier, W Huber, and HJ Guntherodt. Specific antigen/antibody interactions measured by force microscopy. *Biophys. J.*, 70(5):2437–2441, 1996.

[28] Roberto De Paris, Torsten Strunz, Krisztina Oroszlan, Hans-Joachim Güntherodt, and Martin Hegner. Force spectroscopy and dynamics of the biotin-avidin bond studied by scanning force microscopy. *Single Mol.*, 1:285–290, 2000.

[29] Anthony de Vries. *High Force Magnetic Tweezers For Molecular Manipulation Inside Living Cells*. Dissertation, Universiteit Twente, 2004.

[30] N. H. Dekker, C. S. Lee, V. Lorent, J. H. Thywissen, S. P. Smith, M. Drndic, R. M. Westervelt, and M. Prentiss. Guiding neutral atoms on a chip. *Phys. Rev. Lett.*, 84(6):1124–7, Feb 2000.

[31] Tao Deng, George M. Whitesides, Mala Radhakrishnan, Gary Zabow, and Mara Prentiss. Manipulation of magnetic microbeads in suspension

using micromagnetic systems fabricated with soft lithography. *Applied Physics Letters*, 78(12):1775–1777, 2001.

[32] G. T. DeTitta, R. Parthasarathy, R. H. Blessing, and W. Stallings. Carboxybiotin translocation mechanisms suggested by diffraction studies of biotin and its vitamers. *Proc Natl Acad Sci U S A*, 77(1):333–7, Jan 1980.

[33] Dabney Dixon and Don Harden. Some common cofactors. http://chemistry.gsu.edu/glactone/PDB/Cofactor/cofactor.html, 2005.

[34] L. Dong, J. P. Huang, and K. W. Yu. Theory of dielectrophoresis in colloidal suspensions. *Journal of Applied Physics*, 95:8321–8326, June 2004.

[35] Klaus Dose. *Biochemie*. Springer Verlag, 4 edition, 1994.

[36] Samuel Earnshaw. On the nature of the molecular forces which regulate the constitution of the luminiferous ether. *Trans. Of the Cambridge Philosophical Society*, 7(1):97–112, 1842.

[37] R. L. Edelstein, C. R. Tamanaha, P. E. Sheehan, M. M. Miller, D. R. Baselt, L. J. Whitman, and R. J. Colton. The BARC biosensor applied to the detection of biological warfare agents. *Biosens Bioelectron*, 14(10-11):805–813, Jan 2000.

[38] L. Ejsing, M. F. Hansen, A. K. Menon, H. A. Ferreira, D. L. Graham, and P. P. Freitas. Planar Hall effect sensor for magnetic micro- and nanobead detection. *Applied Physics Letters*, 84(23):4729–4731, 2004.

[39] E Evans, D Berk, and A Leung. Detachment of agglutinin-bonded red blood cells. I. Forces to rupture molecular-point attachments. *Biophys. J.*, 59(4):838–848, 1991.

[40] Evan Evans and Ken Ritchie. Dynamic strength of molecular adhesion bonds. *Biophys. J.*, 72:1541–1555, 1997.

[41] Henry Eyring. The Activated Complex in Chemical Reactions. *The Journal of Chemical Physics*, 3(2):107–115, 1935.

[42] H. A. Ferreira, D. L. Graham, P. P. Freitas, and J. M. S. Cabral. Biodetection using magnetically labeled biomolecules and arrays of spin valve sensors (invited). *Journal of Applied Physics*, 93(10):7281–7286, 2003.

[43] Figeys and Pinto. Lab-on-a-chip: a revolution in biological and medical sciences. *Anal Chem*, 72(9):330A–335A, May 2000.

[44] E. L. Florin, V. T. Moy, and H. E. Gaub. Adhesion forces between individual ligand-receptor pairs. *Science*, 264(5157):415–7, Apr 1994.

[45] S. Freitag, V. Chu, J. E. Penzotti, L. A. Klumb, R. To, D. Hyre, I. Le Trong, T. P. Lybrand, R. E. Stenkamp, and P. S. Stayton. A structural snapshot of an intermediate on the streptavidin-biotin dissociation pathway. *Proc Natl Acad Sci U S A*, 96(15):8384–9, Jul 1999.

[46] S. Freitag, I. L. Trong, L. Klumb, P. S. Stayton, and R. E. Stenkamp. Structural studies of the streptavidin binding loop. *Protein Sci*, 6(6):1157–1166, June 1997.

[47] Wolfgang Fritzsche and T. Andrew Taton. Metal nanoparticles as labels for heterogeneous, chip-based dna detection. *Nanotechnology*, (12):R63–R73, 2003.

[48] Peter R. C. Gascoyne and Jody V. Vykoukal. Dielectrophoresis-based sample handling in general-purpose programmable dignostic instruments. In *Dielectrophoretic Concepts for Automated Diagnostic Instruments*, volume 92, pages 22–42, 2004.

[49] M. González, L. A. Bagatolli, I. Echabe, J. L. Arrondo, C. E. Argaraña, C. R. Cantor, and G. D. Fidelio. Interaction of biotin with streptavidin. Thermostability and conformational changes upon binding. *J Biol Chem*, 272(17):11288–94, Apr 1997.

[50] Charlie Gosse and Vincent Croquette. Magnetic Tweezers: Micromanipulation and Force Measurement at the Molecular Level. *Biophys. J.*, 82(6):3314–3329, 2002.

[51] D. L. Graham, H. Ferreira, J. Bernardo, P. P. Freitas, and J. M. S. Cabral. Single magnetic microsphere placement and detection on-chip using current line designs with integrated spin valve sensors: Biotechnological applications. volume 91, pages 7786–7788. AIP, 2002.

[52] D. L. Graham, H. A. Ferreira, P. P. Freitas, and J. M. S. Cabral. High sensitivity detection of molecular recognition using magnetically labelled biomolecules and magnetoresistive sensors. *Biosensors and Bioelectronics*, 18(4):483–488, April 2003.

[53] Daniel L. Graham, Hugo A. Ferreira, and Paulo P. Freitas. Magnetoresistive-based biosensors and biochips. *Trends in Biotechnology*, 22(9):455–462, September 2004.

[54] Grandbois, Beyer, Rief, Clausen-Schaumann, and Gaub. How strong is a covalent bond? *Science*, 283(5408):1727–30, Mar 1999.

[55] N. M. Green. Thermodynamics of the binding of biotin and some analogues by avidin. *Biochem. J.*, 101:774–780, 1966.

[56] N. M. Green and M. D. Melamed. Avidin. *Biochem. J.*, 89:585–620, 1963.

[57] N. Michael Green. Avidin. *Advances in Protein Chemistry*, 29:85–133, 1975.

[58] W. R. Grove. On the electro-chemical polarity of gases. *Philosophical transactions of the Royal Society of London*, 142:87ff, 1852.

[59] H. Grubmüller, B. Heymann, and P. Tavan. Ligand binding: molecular mechanics calculation of the streptavidin-biotin rupture force. *Science*, 271(5251):997–9, Feb 1996.

[60] Paul György, Catharine S. Rose, Klaus Hofmann, Donald B. Melville, and Vincent Du Vigneaud. A further note on the identity of vitamin h with biotin. *Science*, 27:609, 1940.

[61] P. Hänggi, P. Talkner, and M. Borkovec. Reaction-rate theory: fifty years after Kramers. *Reviews of Modern Physics*, 62:251–342, 1990.

[62] Sonja Heitmann. *Cobalt / Copper Multilayers: Interplay of Microstructure and GMR and Recrystallization as the Key Towards Temperature Stability.* Dissertation, Universität Bielefeld, 2004.

[63] Christiane A. Helm, Wolfgang Knoll, and Jacob N. Israelachvili. Measurement of ligand-receptor interactions. *Proc. Natl. Acad. Sci. USA, Biochemistry*, 88:8169–8173, 1991.

[64] Wayne A. Hendrickson, Arno Pähler, Janet L. Smith, Yoshinori Satow, Ethon A. Merritt, and R. Paul Phizackerley. Crystal structure of core streptavidin determined from multiwavelength anomalous diffraction of synchrotron radiation. *Proc. Natl. Acad. Sci. USA Biophysics*, 86:2190–2194, 1989.

[65] Berthold Heymann and Helmut Grubmüller. An02/dnp-hapten unbinding forces studied by molecular dynamics atomic force microscopy simulations. *Chemical Physics Letters*, 303(1-2):1–9, April 1999.

[66] Peter Hinterdorfer, Werner Baumgartner, Hermann J. Gruber, Kurt Schilcher, and Hansgeorg Schindler. Detection and localization of individual antibody-antigen recognition events by atomic force microscopy. *PNAS*, 93(8):3477–3481, 1996.

[67] Holmgren Lab. Life science glossary. http://www.biochem.northwestern.edu/holmgren/Glossary/Definitions/Def-C/cooperativity.html, 2005.

[68] Andreas Hütten, Daniela Sudfeld, Inga Ennen, Gunter Reiss, Wiebke Hachmann, Ulrich Heinzmann, Klaus Wojczykowski, Peter Jutzi, Wahib Saikaly, and Gareth Thomas. New magnetic nanoparticles for biotechnology. *Journal of Biotechnology*, 112(1-2):47–63, August 2004.

[69] Institut für Chemie der FU-Berlin. http://www.chemie.fu-berlin.de/chemistry/general/units.html, 2005.

[70] S. Izrailev, S. Stepaniants, M. Balsera, Y. Oono, and K. Schulten. Molecular dynamics study of unbinding of the avidin-biotin complex. *Biophys. J.*, 72:1568–1581, 1997.

[71] John David Jackson. *Klassische Elektrodynamik*. De Gruyter, 1999.

[72] M. L. Jones and G. P. Kurzban. Noncooperativity of biotin binding to tetrameric streptavidin. *Biochemistry*, 34(37):11750–6, Sep 1995.

[73] M. Julliere. Tunneling between ferromagnetic films. *Physics Letters A*, 54:225–226, 1975.

[74] Arun T J Kadaksham, Pushpendra Singh, and Nadine Aubry. Dielectrophoresis of nanoparticles. *Electrophoresis*, 25(21-22):3625–32, Nov 2004.

[75] P.J. Kelly and R.D. Arnell. Magnetron sputtering: a review of recent developments and applications. *Vacuum*, 56:159–172, 2000.

[76] D. E. Koshland, G. Némethy, and D. Filmer. Comparison of experimental binding data and theoretical models in proteins containing subunits. *Biochemistry*, 5(1):365–85, Jan 1966.

[77] R. Kötitz, W. Weitschies, L. Trahms, W. Brewer, and W. Semmler. Determination of the binding reaction between avidin and biotin by relaxation measurements of magnetic nanoparticles. *Journal of Magnetism and Magnetic Materials*, 194:62–68, 1999.

[78] H. A. Kramers. Brownian motion in a field of force and the diffusion model of chemical reactions. *Physica*, 7:284, 1940.

[79] L. J. Kricka. Microchips, microarrays, biochips and nanochips: personal laboratories for the 21st century. *Clin Chim Acta*, 307(1-2):219–23, May 2001.

[80] M. Krishnan, V. Namasivayam, R. Lin, R. Pal, and M. A. Burns. Microfabricated reaction and separation systems. *Curr Opin Biotechnol*, 12(1):92–98, Feb 2001.

[81] C. H. Kua, Yee Cheong Lam, C. Yang, and Kamal Youcef-Toumi. Review of bio-particle manipulation using dielectrophoresis. In *Innovation in Manufacturing Systems and Technology*. 2005.

[82] L. Lagae, R. Wirix-Speetjens, J. Das, D. Graham, H. Ferreira, , P. P. F Freitas, G. Borghs, and J. De Boeck. On-chip manipulation and magnetization assessment of magnetic bead ensembles by integrated spin-valve sensors. *Journal of Applied Physics*, 91(10):7445–7447, 2002.

[83] Eric T. Lagally, Peter C. Simpson, and Richard A. Mathies. Monolithic integrated microfluidic dna amplification and capillary electrophoresis analysis system. *Sensors and Actuators B: Chemical*, 63(3):138–146, May 2000.

[84] Patrick Royce LeClair. *Fundamental Aspects of Spin Polarized Tunneling*. Dissertation, Universiteit Eindhoven, 2002.

[85] C. S. Lee, H. Lee, and R. M. Westervelt. Microelectromagnets for the control of magnetic nanoparticles. *Applied Physics Letters*, 79(20):3308–3310, 2001.

[86] Gil U Lee, David A. Kidwell, and Richard J. Colton. Sensing discrete streptavidin-biotin interactions with atomic force microscopy. *Langmuir*, 10:354–357, 1994.

[87] H. Lee and R. M. Westervelt. Microelectromagnets for the manipulation of biological systems. *APS Meeting Abstracts*, pages 14003–, 2003.

[88] O. Livnah, E. A. Bayer, M. Wilchek, and J. L. Sussman. Three-dimensional structures of avidin and the avidin-biotin complex. *Proc Natl Acad Sci U S A*, 90(11):5076–80, Jun 1993.

[89] W. H. Meiklejohn and C. P. Bean. New magnetic anisotropy. *Physical Review*, 102(5):1413–1414, 1956.

[90] W. H. Meiklejohn and C. P. Bean. New magnetic anisotropy. *Physical Review*, 105(3):904–913, 1957.

[91] R. Merkel, P. Nassoy, A. Leung, K. Ritchie, and E. Evans. Energy landscapes of receptor-ligand bonds explored with dynamic force spectroscopy. *Nature*, 397:50–53, 1999.

[92] Micromod Partikeltechnologie GmbH. http://www.micromod.de/, 2005.

[93] K. M. Millan, A. Saraullo, and S. R. Mikkelsen. Voltammetric DNA biosensor for cystic fibrosis based on a modified carbon paste electrode. *Anal Chem*, 66(18):2943–2948, Sep 1994.

[94] R. A. Millikan. On the elementary electrical charge and the avogadro constant. *Physical Review*, 2:109–143, 1913.

[95] Jacques Monod, Jeffries Wyman, and Jean-Pierre Changeux. On the nature of allosteric transitions: A plausible model. *J. Mol. Biol.*, 12:88–118, 1965.

[96] Hywel Morgan, Michael P. Hughes, and Nicolas G. Green. Separation of Submicron Bioparticles by Dielectrophoresis. *Biophys. J.*, 77(1):516–525, 1999.

[97] V. T. Moy, E. L. Florin, and H. E. Gaub. Intermolecular forces and energies between ligands and receptors. *Science*, 266(5183):257–9, Oct 1994.

[98] Errica Nardone, Camillo Rosano, Paolo Santambrogio, Flavio Curnis, Angelo Corti, Fulvio Magni, Antonio G. Siccardi, Giovanni Paganelli, Romeo Losso, Biancamaria Apreda, Martino Bolognesi, Alessandro Sidoli, and Paolo Arosio. Biochemical characterization and crystal structure of a recombinant hen avidin and its acidic mutant expressed in Escherichia coli. *Eur. J. Biochem.*, 256(2):453–460, 1998.

[99] B. P. Nelson, T. E. Grimsrud, M. R. Liles, R. M. Goodman, and R. M. Corn. Surface plasmon resonance imaging measurements of DNA and RNA hybridization adsorption onto DNA microarrays. *Anal Chem*, 73(1):1–7, Jan 2001.

[100] Reid N. Orth, T.G. Clark, and H.G. Craighead. Avidin-biotin micropatterning methods for biosensor applications. *Biomedical Microdevices*, 5(1):29–34, March 2003.

[101] Michael Panhorst. Herstellung von nanostrukturen mit s-layer maskentechnik. Diplomarbeit, Universität Bielefeld, 2000.

[102] Anne Pierres, Dominique Touchard, Anne-Marie Benoliel, and Pierre Bongrand. Dissecting Streptavidin-Biotin Interaction with a Laminar Flow Chamber. *Biophys. J.*, 82(6):3214–3223, 2002.

[103] M. Polanyi and E. Wigner. *Zeitschrift für physikalische Chemie A*, page 439, 1928.

[104] W.H. Press, B. Flannery, S. Teukolsky, and W. Vetterling. *Numerical Recipes in C*. Camebridge University Press, 1988.

[105] M. Raible, M. Evstigneev, P. Reimann, F. W. Bartels, and R. Ros. Theoretical analysis of dynamic force spectroscopy experiments on ligand-receptor complexes. *J. Biotechnol.*, 112(1-2):13–23, Aug 2004.

[106] RCSB Protein Data Bank. http://www.rcsb.org/pdb/.

[107] A. Richter, C. Schwager, S. Hentze, W. Ansorge, M. W. Hentze, and M. Muckenthaler. Comparison of fluorescent tag DNA labeling methods used for expression analysis by DNA microarrays. *Biotechniques*, 33(3):620–630, Sep 2002.

[108] Erwin Riedel. *Anorganische Chemie*. de Gruyter, Berlin, 5th edition, 2002.

[109] M. Rief, M. Gautel, F. Oesterhelt, J. M. Fernandez, and H. E. Gaub. Reversible unfolding of individual titin immunoglobulin domains by AFM. *Science*, 276(5315):1109–12, May 1997.

[110] Robert Ros, Falk Schwesinger, Dario Anselmetti, Martina Kubon, Rolf Schäfer, Andreas Plückthun, and Louis Tiefenauer. Antigen binding forces of individually addressed single-chain fv antibody molecules. *Proc. Natl. Acad. Sci. Biophysics*, 95:7402–7405, 1998.

[111] Marc D. Sacher. Präparation und charakterisierung von mehrfachbarrieren für magnetische tunnelelemente. Diplomarbeit, Universität Bielefeld, 2003.

[112] H. Salin, T. Vujasinovic, A. Mazurie, S. Maitrejean, C. Menini, J. Mallet, and S. Dumas. A novel sensitive microarray approach for differential screening using probes labelled with two different radioelements. *Nucleic Acids Res*, 30(4):e17, Feb 2002.

[113] T. Sano and C. R. Cantor. Cooperative biotin binding by streptavidin. Electrophoretic behavior and subunit association of streptavidin in the presence of 6 M urea. *J Biol Chem*, 265(6):3369–73, Feb 1990.

[114] Jörg Schotter. *Development of a magnetoresistive biosensor for the detection of biomolecules*. Dissertation, University of Bielefeld, October 2004.

[115] Seradyn Inc. http://www.seradyn.com/, 2005.

[116] John G. Simmons. Generalized formula for the electric tunnel effect between similar electrodes separated by a thin insulating film. *J. Appl. Phys.*, 34(6):1793–1803, 1963.

[117] A. Sommerfeld and H. Bethe. Elektronentheorie der Metalle. In H. Geiger and K. Schell, editors, *Handbuch derPhysik*. J. Springer Verlag, Berlin, 1933.

[118] Jan Stallkamp. Lattice boltzmann simulations of colloids in hydrodynamic fields. Diplomarbeit, Universität Bielefeld, 2003.

[119] P. S. Stayton. Biophysics. May the force be with you. *Nature*, 397(6714):20–1, Jan 1999.

[120] Mary Beth Stearns. Simple explanation of tunneling spin-polarization of fe, co, ni and its alloys. *Journal of Magnetism and Magnetic Materials*, 5:167–171, April 1977.

[121] T. Strunz, K. Oroszlan, I. Schumakovitch, H.-J. Güntherodt, and M. Hegner. Model Energy Landscapes and the Force-Induced Dissociation of Ligand-Receptor Bonds. *Biophys. J.*, 79(3):1206–1212, 2000.

[122] J. K. Stuart and V. Hlady. Reflection Interference Contrast Microscopy Combined with Scanning Force Microscopy Verifies the Nature of Protein-Ligand Interaction Force Measurements. *Biophys. J.*, 76(1):500–508, 1999.

[123] Joan K. Stuart and Vladimir Hlady. Effects of discrete protein-surface interaction in scanning force microscopy adhesion force measurements. *Langmuir*, 11:1368–1374, 1995.

[124] Andy Thomas. *Preparation and characterisation of magnetic single and double barrier junctions*. Dissertation, Universität Bielefeld, 2003.

[125] Todd Thorsen, Sebastian J Maerkl, and Stephen R Quake. Microfluidic large-scale integration. *Science*, 298(5593):580–584, Oct 2002.

[126] K D Vernon-Parry. Scanning electron microscopy: an introduction. *Analysis*, 13(4):40–44, 2000.

[127] D. Voet, J. G. Voet, and C. W. Pratt. *Lehrbuch der Biochemie*. Wiley-VCH, 2002.

[128] Jody Vykoukal, Daynene Mannering Vykoukal, Susan Sharma, Frederick F. Becker, and Peter R. C. Gascoyne. Dielectrically addressable microspheres engineered using self-assembled monolayers. *Langmuir*, 19:2425–2433, 2003.

[129] J. Wang. From DNA biosensors to gene chips. *Nucleic Acids Res*, 28(16):3011–3016, Aug 2000.

[130] J. Wang, P. E. Nielsen, M. Jiang, X. Cai, J. R. Fernandes, D. H. Grant, M. Ozsoz, A. Beglieter, and M. Mowat. Mismatch-sensitive hybridization detection by peptide nucleic acids immobilized on a quartz crystal microbalance. *Anal Chem*, 69(24):5200–5202, Dec 1997.

[131] P. C. Weber, J. J. Wendoloski, M. W. Pantoliano, and F. R. Salemme. Crystallographic and themodynamic comparison of natural and synthetic ligands bound to streptavidin. *J. Am. Chem. Soc.*, 114:3197–3200, 1992.

[132] PC Weber, MJ Cox, FR Salemme, and DH Ohlendorf. Crystallographic data for Streptomyces avidinii streptavidin. *J. Biol. Chem.*, 262(26):12728–12729, 1987.

[133] Dudley H. Williams, Elaine Stephens, and Min Zhou. Ligand binding energy and catalytic efficiency from improved packing within receptors and enzymes. *Journal of Molecular Biology*, 329(2):389–399, May 2003.

[134] Philip M. Williams, Adam Moore, Molly M. Stevens, Stephanie Allen, Martyn C. Davies, Clive J. Roberts, and Saul J. B. Tendler. On the

dynamic behaviour of the forced dissociation of ligand-receptor pairs. *J. Chem. Soc., Perkin Trans.*, 2:5–8, 2000.

[135] Mark Winter. Webelements periodic table. http://www.webelements.com/, 2005.

[136] Roel Wirix-Speetjens and Jo de Boeck. On-chip magnetic particle transport by alternating magnetic field gradients. *IEEE Transactions on Magnetics*, 40(4):1944–1946, 2004.

[137] Joyce Wong, Ashutosh Chilkoti, and Vincent T. Moy. Direct force measurements of the streptavidin-biotin interaction. *Biomolecular Engineering*, 16:45–55, 1999.

Acknowledgements

Without the help of many co-workers this thesis would not have been possible, and I'm deeply grateful for all the help I received during these years. Especially I would like to thank my supervisors Prof. Günter Reiss, P.D. Dr. Hubert Brückl and P.D. Dr. Andreas Hütten for their continuous support and the funding of my work. Moreover I would like to thank Dr. Jörg Schotter for a great introduction to the biosensor project, practical help, fruitful discussions and proofreading of this thesis.

In particular I thank Dr. Paul-Bertram Kamp from the Department of Genetics at the Bielefeld University for the very productive cooperation. Without his knowledge and practical help regarding molecular biology, this work and especially the bond-force measurements would not have been possible.

Furthermore, I thank Marc Sacher and Dr. Jan Schmalhorst for fruitful discussions and AGM and Auger measurements and Dr. Jan Bornemeier for the help with wire bonding and a lot of fun in our office. For discussions about my work and support in the laboratory I thank Dr. Karsten Rott, Dirk Meyners, Dirk Brinkmann and Astrit Shoshi. I also would like to thank the mechanical and electronic workshop for their support and competent work.

Finally, I would like to thank my family and friends for their everlasting support and in particular my fiancée Sonja Schilling for her love and understanding throughout the years.